Dynamics of Phobos

Reconciling the ephemeris and rotation models

AE5810: Master Thesis

Jorge Martinez Castillo

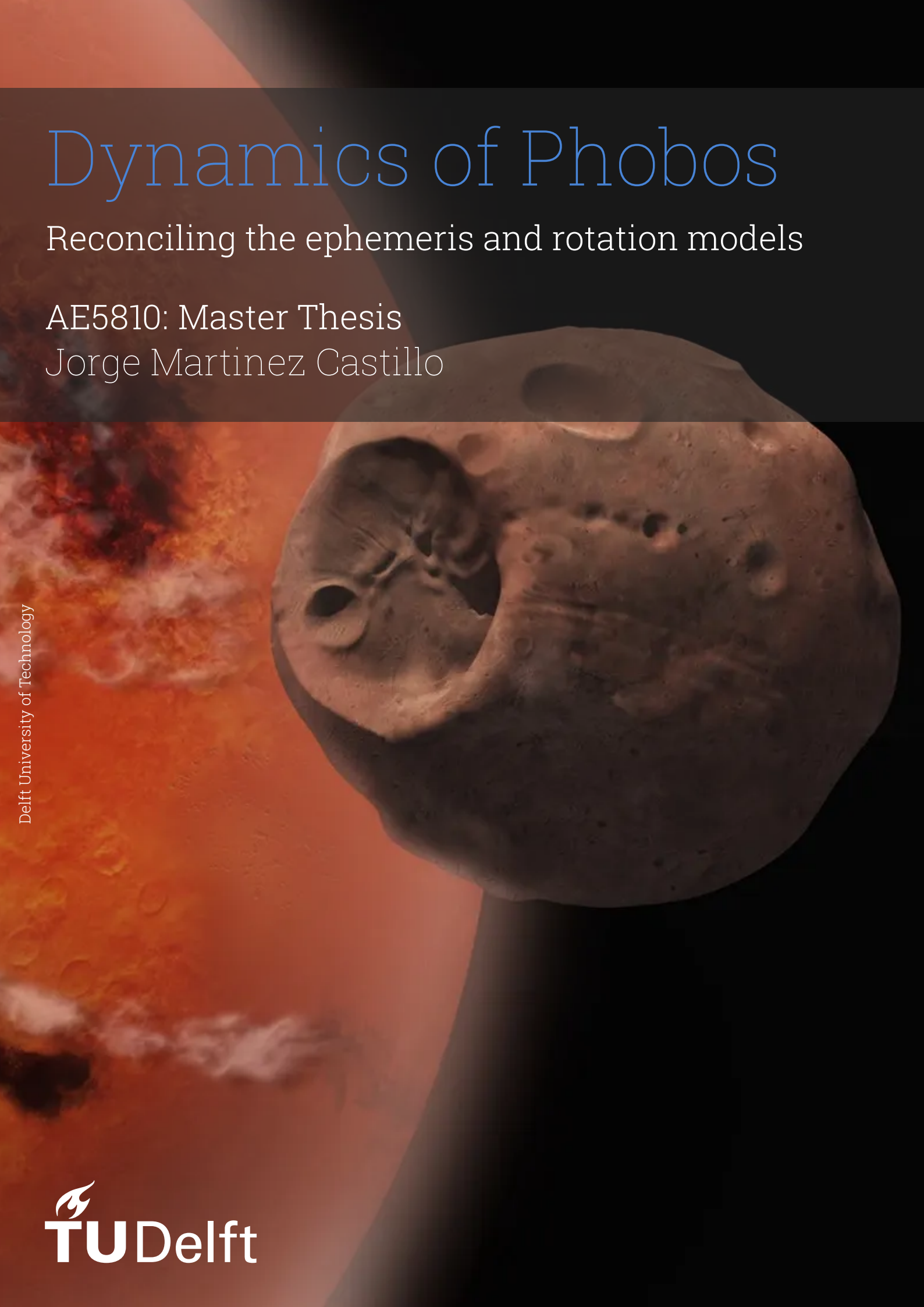

Delft University of Technology

TU Delft

Dynamics of Phobos

Reconciling the ephemeris and rotation models

by

Jorge Martinez Castillo

Student number: 5626919
Project duration: September 2022 – November, 2024
Supervisor: Dominic Dirkx

Cover: "3d illustration of the moon Phobos and the planet Mars" - Esteban De Armas at shutterstock.com
Style: TU Delft Report Style, with modifications by Daan Zwaneveld

TU Delft

Preface

This thesis began in September 2021, when I sent an email to my then-to-be supervisor telling him that a rock was a cool thing to spend nine months on at the end of the masters. And here we are, at the very end of a two-and-half-year degree.

Two and a half years in which (TU) Delft has given me more than I could have ever imagined through a big lot of people that became home when home was on the other side of the continent. It would be impossible to fit the whole cast and crew of this movie in a single page, but there are some characters who deserve special mention. Like Ernesto and Sofía, who began the Dutch journey with me on the very first day we set foot on campus, and who I would like to be part of whatever life throws at me next. Like the whole Spanish group, both OGs and new additions, some of which are already living their new lives someplace else, some of which will do so before they realize, but all of which I will definitely make my moves to see again. Especial thanks to the main characters of my second year, Elemer and Emma, who have been my 24/7 for months and without whom a morning is never really a "good morning". Thank you so much to all these people for picking me up when I was down, for making good times better, and for being there through thick and thin.

Thank you in particular to those with whom I have worked closely on this project: Dominic and Marie. You gave me not only the tools to make this thesis a piece of work that I am proud of, but also the knowledge and mindset that will make it only the first of what I hope will be a long list of works, each better than the previous one. I don't think there are words to even approximate how much I have learnt from you, and how much of a completely different person I am from that kid who started the masters two years ago. I also want to thank you for creating a working environment in which I felt valued, safe and in which I could thrive in the best direction possible. I am writing this with the prospect of spending the next five years of my life in the planetary science scene in Europe, and you have somehow managed to give me the security and confidence to stand up to all the challenges that come my way. This extends to Stéphanie Cazaux, who has made me see that the people that will surround me in the coming scientific adventure will not only be top-notch experts, but also insane fun.

This list would be very incomplete without Maria Scali, my adopted Italian-Dutch grandmother, who gave me all the help I could not ask for in the time I needed it most, and who luckily hasn't left the scene ever since. I hope I can still say the same thing in a month, a year, and a lifetime. Finally, a million thanks to this special category of people who have been with me mostly from the other side of my phone's screen, my family and friends, back in Lodosa and Alfaro but always with me wherever I go.

I would like to dedicate some words to those places, occasions, and people whose absence - or rather *my* absence - have bitterly marked these two years in the Netherlands. To all those festivities in my town that I couldn't attend. To all those local vegetables I have been away from. A la Banda de Música de Lodosa, especially the after-rehearsal beer gang. There is no way of expressing how much the distance between me and each and every of these things pains me daily, deep in my heart and soul.

Jorge Martinez Castillo
Delft, November 2023

Abstract

This thesis studies the dynamics of Phobos, Mars' bigger moon, as part of the preparation for coming Phobos-bound missions. Existing observations have not been able to properly constrain the interior of the two Martian moons in general and Phobos in particular, being therefore inconclusive about their origin and formation. Thus, on-site measurements with the aid of Phobos landers is planned for the near future. In particular, this thesis focuses on the couplings between Phobos' translational and rotational dynamics. Their effect in state propagation is quantitatively described and their impact on parameter estimation is assessed.

For this, the trajectory of Phobos has been computed by propagating a given initial state in two ways. A first manner integrates Phobos' translational and rotational equations of motion simultaneously; a second manner integrates Phobos' translational equations of motion alone, and assumes that Phobos is in a fully-locked configuration with a once-per-orbit longitudinal libration. A first part of the results is an analysis of the differences between these two solutions, in terms of position and orientation.

A second part of the solution is the analysis of least-squares estimations, by which the uncoupled model is fit to observations taken from the coupled trajectory. In doing so, the best way in which the uncoupled model can imitate the coupled model by changing some dynamical parameters is found. The results are analyzed in terms of estimation post-fit residuals - the final differences between the coupled and uncoupled solutions - and differences between the parameter estimates and the true parameters. These parameters comprise mostly the once-per-orbit libration amplitude and the quadrupole gravity field, all of which provide information of Phobos' interior.

The outcome of this thesis is a detailed and quantitative study of the extent to which an uncoupled model can imitate a coupled model and how the differences generated by couplings are absorbed into modifications of estimated parameters to keep the to trajectories as similar as possible. This provides a preliminary approximation of the type of true errors that state-of-the-art estimations contained in their fitted solutions.

Contents

Nomenclature

Latin symbols

Symbol	Meaning
a	Semimajor axis
A	Lowest principal moment of inertia.
B	Middle principal moment of inertia.
C	Largest principal moment of inertia.
$\overline{C}_{l,m}$	Normalized cosine harmonic coefficient of degree l and order m
e	Orbital eccentricity.
$\vec{h}$	Vector of model values.
i	Orbital inclination.
$\boldsymbol{I}$	Tensor of inertia.
M	Mass.
$\boldsymbol{q}$	Rotation quaternion.
$\boldsymbol{R}$	Rotation matrix.
$\vec{r}$	Position vector. In the absence of subscripts, it goes from Mars' to Phobos' centers of mass.
$\hat{r}$	Unit vector in the direction of $\vec{r}$.
R	Coordinate associated to vector $\hat{r}$.
$\hat{s}$	Unit vector in the direction of $(\vec{r} \times \vec{v}) \times \vec{r}$.
S	Coordinate associate to vector $\hat{s}$.
$\vec{v}$	Velocity vector. In the absence of subscripts, the velocity of Phobos relative to Mars.
$\hat{w}$	Unit vector in the direction of $\vec{r} \times \vec{v}$.
W	Coordinate associated to vector $\hat{w}$.
$\vec{x}$	Generic state vector.
$\vec{x}_r$	Rotational state vector.
$\vec{x}_t$	Translational state vector.
$\vec{y}$	Generic vector of estimated parameters.
$\vec{z}$	Vector of observations.

Greek symbols

Symbol	Meaning
α	Generic placeholder. Ratio of moments of inertia $(C - B)/A$.
β	Ratio of moments of inertia $(C - A)/B$.
$\vec{\eta}$	Velocity vector expressed in RSW components.
$\vec{\varepsilon}$	Residual vector.
γ	Physical longitudinal libration angle.
μ	Gravitational parmeter.
$\vec{\omega}$	Angular velocity vector.
Ω	Right ascension of ascending node (RAAN)
ω	Argument of pariapsis.
ψ	Tidal longitudinal libration angle.

Symbol	Meaning
$\vec{\rho}$	Position vector expressed in RSW components.
$\vec{\rho}_{AB}$	Vector that goes from center of mass of body A to center of mass of body B, expressed in the reference frame associated to body A.
σ	Ratio of moments of inertia $(B - A)/C$.
θ	True anomaly. Longitude.
ϕ	Latitude.

1

Introduction

Our knowledge of the history of the Solar System is shaped by the theories of planetary system formation and evolution. The two Martian moons, Phobos and Deimos, seem to fit many and none of these theories. The physical properties of these bodies - albedo, density, ... - suggest they are asteroids that were captured by Mars. However, their (quasi)equatorial and (quasi)circular orbits make this possibility very unlikely, as it would involve strong circularizing mechanisms to bring the moons' orbits from the highly elliptic capture orbits to circles, not to mention the big inclination change (about 25º) of Mars' equator with respect to the ecliptic.

Because the Martian moons push the limits of our knowledge on the formation and evolution of planetary systems, they represent a very good opportunity to improve on what we know. The biggest of the two, Phobos, has received the most attention of the two since their discovery in 1877 (Woolard, 1944; Kerr and Whipple, 1951; Smith, 1970; Veverka, 1978; Dobrovolskis, 1982; Murray et al., 2006; Oberst et al., 2014; Usui et al., 2020). State-of-the-art knowledge of this moon mainly comprises its bulk mass, with its mass distribution usually being extracted from better or worse estimates of its once-per-orbit longitudinal libration amplitude (e.g. Lainey et al. (2021)) and gravity field coefficients (e.g. Lainey et al. (2007) or Jacobson (2010)). This has not been sufficient so far to properly constrain Phobos' interior structure in terms of composition, layering and/or porosity, and many models still fit current observations (Maistre et al., 2019).

In order to acquire new types of observations, space missions to Phobos are being under way, the most prominent being JAXA's sample return mission *MMX* (*Martian Moons eXploration*) (Usui et al., 2020). The Phobian regolith brought to Earth by this mission will provide unprecedented information on Phobos' surface composition (Usui et al., 2020). The mission, which will consist of a Phobos orbiter and a lander, will require orbiter tracking. On the one hand, landing on Phobos imposes unprecedented requirements on the modelling of the position and orientation of Phobos. On the other hand, range and range rate measurements to the orbiter and, potentially, to the lander, will bring an orders-of-magnitude improvement in state-of-the-art observational uncertainty. This in turn reduces the uncertainty of state-of-the-art parameter fits.

With better observations, appropriate dynamical models used to process them should not compromise the quality of the science products. This thesis evaluates state-of-the-art dynamical models used to process existing data in order to assess whether they are appropriate to also process data generated by future missions. In particular, it focuses on the couplings between Phobos' translational and rotational dynamics. In nature, the accelerations and torques acting of Phobos are determined by both Phobos' position and orientation, so that Phobos' translation and rotation interact with each other "in real time" - i.e. the two motions are *coupled*. However, state-of-the-art models assume a simplified rotation and consider only Phobos' translational dynamics - they are *uncoupled* models. It is assumed that this is sufficiently close to reality to properly process data - and until now, this has been the case. However, this assumption should be re-evaluated in the context of an improved observational accuracy. This thesis provides a systematic analysis to determine the extent to which these uncoupled models can really be used in lieu of coupled models, more representative of Phobos' actual dynamics.

1.1. Research questions

Following the line of thought from the introduction, the main research question this thesis will try to answer can be formulated as follows:

- To what extent can an uncoupled dynamical model of Phobos' translation and rotation emulate a coupled dynamical model?

In order to facilitate the research work and guide the answer to the broader research question above, the following subquestions have been formulated:

- How does the trajectory of Phobos change when an initial state is integrated with an uncoupled model as opposed to a coupled model?
- How well do analytical approaches to describe Phobos' orientation in an uncoupled model represent the features of the rotational motion obtained by numerically integrating a coupled model?
- What are the differences between the parameters estimated by an uncoupled estimation model and the parameters used to generate the observations with a coupled model?

1.2. Thesis outline

The bulk of the content of this thesis is provided in the form of a research paper included in chapter 2. Using the findings in this paper, chapter 3 provides specific answers to the research (sub)questions presented above in section 1.1. It also gathers recommendations of future work that naturally follows the line of research of this paper. Complementary sections are provided as appendices. In particular, Appendix A presents the process that was followed in order to select the integrator that was used in numerical simulations. On the other hand Appendix B gathers the different ways in which the software that was developed has been verified. This includes validation of the propagation suites, both in terms of translational and rotational dynamics. Of particular interest is the verification of the damping algorithm in section B.2. The estimation suite was also verified in section B.3 and, in fact, a bug was found in *Tudat*'s computation of the state partials when the dynamical model features the once-per-orbit longitudinal libration. Thus, an alternative partial computation scheme had to be developed, which is therefore verified in section B.4.

2

Research paper

The main body of this thesis has been written in the form a research paper. It is included in this chapter in the corresponding paper format.

Translational-rotational couplings in the dynamics of Phobos

Jorge Martinez[a]

[a]Delft university of Technology, Kluyverweg 1, Delft, 2629HS, The Netherlands

Abstract

Upcoming science missions to Phobos will potentially provide unprecedented observations of Phobos' orbit in the form of lander tracking data. This will likely require updating dynamical models currently used to invert this data. State-of-the-art estimations are performed using translational models together with an evolution of Phobos' orientation determined by the translational state itself. This paper investigates the role that couplings between Phobos' translational and rotational dynamics play in the moon's motion in order to assess the extent to which uncoupled models can emulate coupled models, and what consequences the mis-modelling has on the products of data inversion. We considered two models: a coupled model that propagates Phobos' translational and rotational dynamics simultaneously, and an uncoupled model that assumes Phobos to be in a fully-locked configuration with a once-per-orbit longitudinal libration. By simulating the dynamics for about 10 years, first in a coupled and then in an uncoupled manner, the results were compared and, furthermore, the coupled trajectory was used as simulated observations for an estimation of different parameters using uncoupled translational dynamics. For identical initial states, differences between the coupled and uncoupled trajectories were found to accumulate to 40 m, most predominantly in Phobos' direction of motion. Longitudinal librations were mis-represented by the uncoupled model particularly around the frequencies of the normal mode, where forcings are amplified up to 3.6×10^{-3} degrees. Long-term latitudinal librations also arise from forcings due to coupling-induced changes in orbital inclination. The use of uncoupled models in data inversion results in true errors in the estimated parameters. In this case, estimations of different lengths up to 250 days were performed estimating Phobos' initial state, once-per-orbit libration amplitude and harmonic coefficients $\overline{C}_{2,0}$ and $\overline{C}_{2,2}$. Errors in dynamical parameters were found to be in the order of 10^{-3} degrees for the physical libration amplitude and of 10^{-5} for the harmonic coefficients. These true errors are 1 to 3 orders of magnitude above the formal errors expected from laser ranging measurements to a Phobos lander, indicating that uncoupled models are not suitable for the proper inversion of such data.

Keywords: Phobos, Libration, Spin-orbit coupling

1. Introduction

The two Martian moons, Phobos and Deimos, are the only natural satellites - together with our own - that orbit a terrestrial planet. However, the moons of the red planet are completely different from that of the Earth. Discovered by Hall (1878), they were repeatedly observed from Earth during the next years - e.g. Pickering et al. (1879); Keeler (1888); Newall (1895) - and they were found to be in (quasi-)equatorial (Marth, 1879) and (quasi-)circular (Woolard, 1944) orbits. This suggested that the two moons had been formed in Mars' proto-planetary disc. However, with the advent of Martian orbiters, space-borne photography revealed Phobos to have very low albedo (Smith, 1970), while colored pictures showed Phobos' surface composition to be very similar to that of a carbonaceous chondrite (Veverka, 1978). This indicated that the Martian moons had likely been captured asteroids.

As recently as 2023, the origin and evolution of the Martian moons - and in particular of Phobos - is still unclear (Miranda et al., 2023). Information on the present day interior of Phobos can help constrain its evolution. This information can obtained by processing observations of Phobos' position - as done by Tolson et al. (1977) or Akim et al. (2007) - the amplitude of Phobos' so-called once-per-orbit longitudinal libration (see Duxbury and Callahan (1989), Willner et al. (2010) or Oberst et al. (2014)) and Phobos' gravity field. The dynamical models used to process observations should be at least as accurate as the observations themselves, meaning that errors arising from dynamical

(mis)modelling should stay below observation-derived uncertainties.

Current efforts in inverting orbit data integrate Phobos' dynamics under the assumption that Phobos is in a fully-locked configuration (Lainey et al., 2007), often times featuring a once-per-orbit longitudinal libration (Shishov, 2008; Jacobson, 2010; Jacobson and Lainey, 2014; Lainey et al., 2021). Phobos' gravity field is often represented by the so-called quadrupole field, i.e. only the $C_{2,0}$ and $C_{2,2}$ harmonic coefficients (Lainey et al., 2007; Jacobson, 2010; Jacobson and Lainey, 2014; Lainey et al., 2021). Because of the simple dynamical model assumed for Phobos, estimated dynamical parameters are limited to the amplitude of Phobos' once-per-orbit longitudinal libration (Jacobson, 2010; Lainey et al., 2021) or the values of the $C_{2,0}/C_{2,2}$ coefficients (Lainey et al., 2007; Jacobson and Lainey, 2014). Latest estimates are accurate to the 0.01 degrees (0.9%) for the libration amplitude (Lainey et al., 2021) and to the $10^{-3} - 10^{-4}$ (2.7%-6.3%) for $C_{2,0}$ and $C_{2,2}$ (Jacobson and Lainey, 2014). Jacobson (2010) notes that simultaneous estimation of all three of these parameters is not possible because the resulting estimation problem is ill-posed. Dirkx et al. (2014) also attempted to fit a broad range of libration amplitudes and phases to simulated observations, both in longitude and latitude, and reported very high correlations among them.

On the other hand, the *shape* of Phobos can be measured through bundle block adjustments (Duxbury, 1974; Burmeister et al., 2018). This product, however, is insensitive to Phobos' *interior*. A by-product of these bundle-block adjustments is the amplitude of the once-per-orbit longitudinal libration, provided as well by Willner et al. (2010), Nadezhdina and Zubarev (2014) and Oberst et al. (2014). A broader range of librations has been investigated by the semi-analytical ESAPHO theory (Chapront-Touze, 1988), which was used by Borderies and Yoder (1990) to study Phobos' librations, most notably longitudinal librations at the frequencies of once, twice and three times the mean motion.

However, current estimates of so-far considered parameters - i.e. once-per-orbit longitudinal libration, $C_{2,0}$ and $C_{2,2}$ - have not been able to sufficiently constrain the interior of present-day Phobos, and several different internal structures are still possible (Maistre et al., 2019). Phobos-bound space missions - e.g. MMX (Nakamura et al., 2021) - are currently under way, which will provide orbiter and (potentially) lander tracking data. These new observation types are expected to represent order-of-magnitude improvement in observational-derived uncertainty of data inversion products (Dirkx et al., 2014), and therefore current dynamical models used in these data inversions should be reevaluated in order to keep up with this new observation-imposed requirements. It was noted by Yang et al. (2020) that a simultaneous integration of Phobos' orbit and rotation would allow their work to provide more meaningful results. A coupled translational-rotational model has in fact not yet been used in data inversion - or state propagation for that matter - when studying Phobos' dynamics, with the state-of-the-art being uncoupled translational models. It is this area of dynamical couplings between Phobos' translational and rotational dynamics that this work will investigate. More precisely, it will attempt to assess the extent to which state-of-the-art uncoupled dynamical models can emulate the translational and rotational features of coupled models, and what dynamical parameters minimize position differences between the two solutions.

An overview of the mathematical description of Phobos' dynamics is given in section 2. This section will also provide an in-depth analysis of different considerations of Phobos' rotational motion, like normal modes and librations. Section 3 will introduce all definitions and equations used in this work concerning the estimation problem and data inversion. Then, results will be presented in section 4 and, finally, section 5 and section 6 will focus on what these results mean in the context of future work and will gather the main points of this paper.

2. Dynamical model

In this work, Phobos' translational dynamics are described through the translational equations of motion (EOM), while two different descriptions of Phobos' rotational motion are used: a dynamical description (through EOMs) and a kinematical description. While the former uses torques to integrate a set of variables that represent Phobos' orientation (e.g. Euler angles), the latter uses simplified closed expressions to describe the time evolution of those variables.

This section will first present the mathematical formulation of all the elements that make up the equations of motion. Then, it will collect the kinematic descriptions of Phobos' motion that are most relevant for this work, and how using a dynamical description of this motion plays a role in the equations of motion. Finally, the different dynamical models used in this work will be presented.

2.1. Equations of motion

For the sake of context, a brief description of some reference frames of interest is provided first. Then, the state vector of Phobos is defined, and then the equations of motion describing the time evolution of said state vector are presented.

The motion of Phobos will be described within the Martian system, and a reference frame - from now on *J2000* - is defined with origin at Mars' center of mass. The orientation of this frame, however, is referred to Earth's equator of date at the J2000 epoch, with the frame's x-axis pointing towards vernal equinox and its z-axis aligned with the Earth's rotation vector as it was in the epoch of J2000. The y axis completes the right-handed triad. Each body can be assigned a so-called *body-fixed frame* or simply *body-frame*, with origin at the body's center of mass and the three axes aligned with the body's principal axes of inertia, with the x-axis along the longest axis and the z axis along the shortest one. In the following, any of these reference frames may be used to express vectors.

The state vector $\vec{x}$ of Phobos contains a description of its state of motion at an innd orientation rate (*rotational state*, $\vec{x}_r$), or both. In this work, the translational state vector will be formed by Phobos' position and velocitystant of time, which can be in terms of translation (the *translational state*, $\vec{x}_t$), the orientation a vectors with respect to Mars, $\vec{r}$ and $\vec{v}$ respectively. On the other hand, the rotational state vector will be formed by Phobos' *rotation quaternion*, $\boldsymbol{q}$, and Phobos' angular velocity vector, $\vec{\omega}$. The components of $\vec{\omega}$ are always referred to the body-frame.

As any other body, Phobos' translational dynamics are driven by accelerations, while its rotational dynamics are driven by torques. In this work, all accelerations and torques are gravitational in nature and they are formulated as in Equation 1 (drag, solar radiation pressure and the Yarkovsky effect are ignored due to low expected impact on results and difficulty in modelling them). In these equations, U_A and U_B are the gravitational potentials of bodies A and B respectively, $\vec{\rho}_{AB}$ is a vector going from A to B expressed in the body-frame of A and similarly $\vec{\rho}_{BA}$ is a vector going from B to A expressed in the body-frame of B. Subscripts $\mathcal{A}$ and $\mathcal{B}$ in $\nabla_{\mathcal{A}}$ and $\nabla_{\mathcal{B}}$ indicate that the gradients are taken with respect to coordinates associated to the body-frames of A and B respectively, and the result is to be understood as vectors expressed in said reference frames. That is why the rotation matrices $\boldsymbol{R}^{\mathcal{I}/\mathcal{A}}$ and $\boldsymbol{R}^{\mathcal{I}/\mathcal{B}}$ are required to rotate them to a common, inertial frame.

$$\vec{a}_{AB} = \boldsymbol{R}^{\mathcal{I}/\mathcal{A}} \nabla_{\mathcal{A}} U_A(\vec{\rho}_{AB}) \tag{1a}$$

$$\vec{T}_{AB} = -M_A \boldsymbol{R}^{\mathcal{I}/\mathcal{B}} \left(\vec{\rho}_{BA} \times \nabla_{\mathcal{B}} U_B(\vec{\rho}_{BA})\right) \tag{1b}$$

In this work, the gravitational potential U that a body exerts at any point in space will be represented through the so-called *spherical harmonic expansion*, as in Equation 2 (Battin, 1999). Here, the distance to the origin r, longitude λ and latitude ϕ are the spherical coordinates of the point at which the potential is computed referred to a reference frame attached to body A. On the other hand, μ and R are the gravitational parameter and reference radius of body A, $P_{l,m}$ are the so-called *Legendre polynomials* of degree l and order m and $C_{l,m}$ and $S_{l,m}$ are the associated cosine and sine coefficients. This works considers all bodies as rigid bodies, so that these harmonic coefficients and time-invariant.

$$U_A(r, \lambda, \phi) = \sum_{l=0}^{\infty} \sum_{m=0}^{l} U_{A,l,m}(r, \lambda, \phi) \tag{2a}$$

$$\begin{aligned} U_{A,l,m}(r, \lambda, \phi) = \frac{\mu}{r} \left(\frac{R}{r}\right)^l P_{l,m}(\sin\phi) \times \\ \times \left(C_{l,m} \cos(m\lambda) + S_{l,m} \sin(m\lambda)\right) \end{aligned} \tag{2b}$$

With this notation, the mutual acceleration between Phobos and Mars is given as in Equation 3 (Dirkx et al., 2014), where the M stands for Mars and P stands for Phobos. The bar and hat notations indicate the center of mass and extended body terms of the accelerations respectively - i.e. $\vec{a}_{\hat{A}\bar{B}}$ is the evaluation of Equation 1a where U_A is evaluated as in Equation 2 starting at $l = 1$.

$$\vec{a} = (\mu_M + \mu_P)\left(-\frac{\vec{r}}{r^3} + \frac{1}{\mu_M}\vec{a}_{\hat{M}\bar{P}} - \frac{1}{\mu_P}\vec{a}_{\hat{P}\bar{M}}\right) \tag{3}$$

This work includes the accelerations and torques exerted on Phobos by Mars, Deimos, the Sun, the Earth and Jupiter, as well as Phobos' own gravitational field. Note that, in the case of Phobos's own acceleration and torque, Equation 1 requires, on the one hand, the evaluation of $\boldsymbol{R}^{\mathcal{I}/\mathcal{P}}$, the rotation matrix from Phobos' fixed-frame to J2000 and, on the other hand, the evaluation of $\vec{\rho}_{Pi}$, the vector going from Phobos' center of mas to any body i. This means that computing both accelerations and torques involves both the translational and rotational states of Phobos. The full dynamics of Phobos are given by Equation 4 (e.g. Dirkx et al. (2019)), under the assumption of a time-invariant inertia tensor $\boldsymbol{I}$ in the Phobos-fixed frame (i.e. Phobos is treated as a rigid body). In this equation, $\vec{x}_t$ and $\vec{x}_r$ represent Phobos' translational and rotational state vectors, $\vec{T}$ is the resultant torque and $\boldsymbol{q}$ is Phobos' rotation quaternion, with its i-th component denoted q_i. It is emphasized

that this quaternion is not treated in this work in a rigorously mathematical manner as the classical quaternion object (e.g. Goldman (2011)), but rather as a vector in the sense of a collection of values. More specific details on the terms of these equations of motion can be found on Appendix A. For this work, these equations have been numerically integrated using an RKF8(10) integrator working in a fixed-step regime of 5 minutes, resulting in a sub-millimeter accuracy.

$$\dot{\vec{x}}_t = \begin{bmatrix} \dot{\vec{r}} \\ \dot{\vec{v}} \end{bmatrix} = \begin{bmatrix} \vec{v} \\ \vec{a} \end{bmatrix} \tag{4a}$$

$$\dot{\vec{x}}_r = \begin{bmatrix} \dot{\boldsymbol{q}} \\ \dot{\vec{\omega}} \end{bmatrix} = \begin{bmatrix} \boldsymbol{Q}\vec{\omega} \\ \boldsymbol{I^{-1}}\left(\vec{T} - \vec{\omega} \times (\boldsymbol{I}\vec{\omega})\right) \end{bmatrix} \tag{4b}$$

$$\boldsymbol{Q} = \frac{1}{2}\begin{bmatrix} -q_1 & -q_2 & -q_3 \\ q_0 & -q_3 & q_2 \\ q_3 & q_0 & -q_1 \\ -q_2 & q_1 & q_0 \end{bmatrix} \tag{4c}$$

Equation 4 represents a coupled system of ODEs that can generally written as in Equation 5, where the dependence of each state derivatives in both the translational and rotational state vectors has been made explicit.

$$\dot{\vec{x}}_t = \vec{f}_t\left(\vec{x}_t, \vec{x}_r\right) \tag{5a}$$

$$\dot{\vec{x}}_r = \vec{f}_r\left(\vec{x}_t, \vec{x}_r\right) \tag{5b}$$

In conclusion, Phobos' dynamics are coupled by nature. However, an uncoupled model can be defined that propagates only the translational equations of motion (Equation 5a) by imposing some fixed $\vec{x}_r(t)$ that is not integrated. However, a coupled model that incorporates the same accelerations and the appropriate torques is regarded as more faithful to reality.

2.2. Kinematic rotation descriptions

There is a number of ways to parameterize the orientation of a body (Fukushima, 2012). For Solar System bodies, the most popular manner is by specifying the orientation of the rotation axis - or *pole* - by its right ascension and declination with respect to a frame of inertial orientation, together with the longitude of the meridian in said frame (see e.g. Archinal et al. (2018); Burmeister et al. (2018)). This amounts to three parameters, and attempts have been often made at providing expressions for their evolution in time (Duxbury and Callahan, 1981; Stark et al., 2017; Archinal et al., 2018).

Phobos' pole follows the long-term orientation of the orbital plane normal (Stark et al., 2017), and Phobos' rotates about it at a frequency that follows the long-term evolution of the mean motion (Jacobson et al., 2018). In terms of Phobos' body-fixed frame (see subsection 2.1), this means that, on average, Mars' Phobos-fixed position is constant in time. Furthermore, there exist oscillatory deviations from this constant rotational rate, known as *longitudinal librations*. This situation allows to visualize Phobos' orientation in two dimensions, which is represented in Figure 1. The deviation of Phobos' x-axis from the moon-planet direction is sometimes termed the *tidal libration* angle (Lainey et al., 2019), and is denoted ψ in Figure 1. The sign of this angle in the figure is just a matter of definition, and in this work this tidal libration angle is defined as in Equation 6, where λ is the longitude of Mars in Phobos' body-frame.

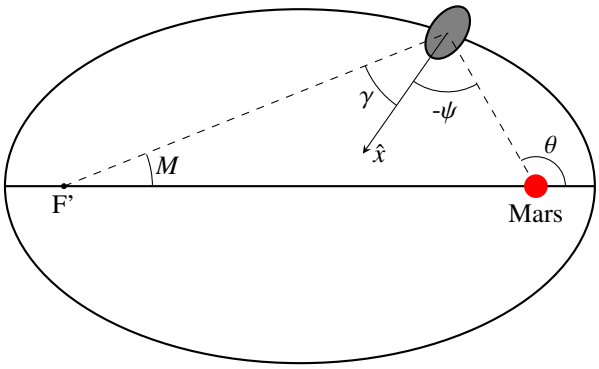

Figure 1: Librational geometry, where θ and M are the true and mean anomalies of Phobos in its orbit, ψ is the tidal libration angle and γ is the physical libration angle. F' represents the empty focus of the ellipse. The fact that M is the angle between the moon-to-empty-focus and the apse line has been taken from Murray and Dermott (1999).

$$\psi = -\lambda \tag{6}$$

When, instead of the moon-planet direction, the moon-to-empty-focus direction is taken as reference from which to measure the direction of Phobos' x-axis, the deviation of this axis from the reference is known as the *physical libration* angle, denoted γ in Figure 1. However, the use of this reference direction presents a complication. Because Phobos' orbit is not perfectly Keplerian, the shape and size of the ellipse change over time and the empty focus moves, so this reference is by definition unstable. Furthermore, with the orientation of Phobos following the orbital geometry for long timescales, taking a geometrical construct as reference introduces long-periodic terms in Phobos' physical librations, which are really the orbital trends of node and apse precession.

The angle between the empty-focus-to-moon line and the line of apsides is given by the mean anomaly M (Murray and Dermott, 1999). Note that, because the

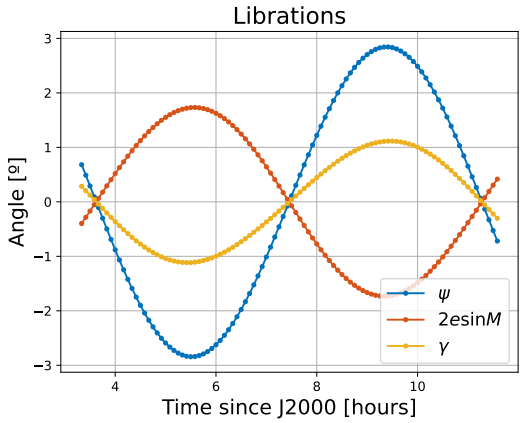

Figure 2: Evolution over one orbit of the tidal libration $\psi = -\lambda$, optical libration $2e \sin M$ and physical libration $\gamma = 2e \sin M + \psi$.

angles of the triangle formed by Mars, Phobos and the empty focus have to amount to 180º, one can write Equation 7, where the final approximation is taken from Murray and Dermott (1999). This quantity is sometimes termed the *optical libration* (Lainey et al., 2019).

$$\gamma - \psi = \theta - M \approx 2e \sin M \tag{7}$$

The largest component of these longitudinal librations is an oscillation with period the same as the orbital period, and Phobos' orientation in the plane is often represented in research just by this component. In terms of the physical libration angle γ, this oscillation is given by Equation 8 where $\mathcal{A}$ is just the amplitude of the oscillation - the so-called *libration amplitude*. The *scaled libration amplitude* $\mathcal{B}$ for the tidal libration angle was introduced by Lainey et al. (2019) as a fitted parameter in their work, and is also the parameter that *Tudat*[1] uses to describe this once-per-orbit libration.

$$\gamma = \mathcal{A} \sin M \quad \text{with} \quad \mathcal{A} < 0 \tag{8a}$$

$$\psi = \mathcal{A} \sin M - 2e \sin M = -\mathcal{B}e \sin M \quad \text{with } \mathcal{B} > 0 \tag{8b}$$

The signs of $\mathcal{A}$ and $\mathcal{B}$ are required for Equation 8a and Equation 8b to be consistent with Figure 2, where the sign of both γ and ψ is seen to be the opposite of $\sin M$.

Because $\mathcal{A}$ and $\mathcal{B}$ are related through Equation 8b, Phobos's orientation in the orbital plane can be described through either. This work will use the latter for two reasons. On the one hand, consistency with *Tudat*, the numerical tool used for simulations. On the other hand, it lends itself to a clearer interpretation because it is defined with respect to a stable, well defined reference. Other works, however, prefer to use $\mathcal{A}$. Depending on how different authors define their libration angles, different relationships between $\mathcal{A}$ and $\mathcal{B}$ will hold for different sources. In this particular work, this relationship is given as in Equation 9.

$$\mathcal{A} = (2 - \mathcal{B})\, e \tag{9}$$

The value of the libration amplitude provides information on Phobos' moment of inertia through Equation 10 (Murray and Dermott, 1999), where $\sigma = (B - A)/C$ and $A \leq B \leq C$ are Phobos' main moments of inertia. Thus, estimation of the once-per-orbit libration amplitude can help constrain the interior structure of Phobos.

$$\mathcal{A} = \frac{2e}{1 - \frac{1}{3\sigma}} \tag{10a}$$

$$\mathcal{B} = \frac{2}{1 - 3\sigma} \tag{10b}$$

Although the discussion so far has focused on longitudinal librations - oscillations about Phobos' z-axis - and the orientation of Phobos' x-axis in the orbital plane, because those are indeed the most prominent aspects of Phobos rotational motion, other oscillations exist about Phobos' x and y axes, the latter being called *wobble* and *latitudinal* librations respectively. Kinematic descriptions of the rotation of Phobos usually don't include them, and they have rarely been considered in Phobos' dynamics, with Borderies (1977) and Rambaux et al. (2012) being works that have been partly dedicated to the study of latitudinal librations.

In the most popular of these simplified, kinematical descriptions of Phobos' orientation, which feature the once-per-orbit longitudinal libration, the rotational state $\vec{x}_r$ of Phobos is not driven anymore by torques, but rather is completely determined by the translational state $\vec{x}_t$ and some extra parameters, namely $\mathcal{A}$ or $\mathcal{B}$. This effectively decouples Equation 5a from Equation 5b by making, for example, $\dot{\vec{x}}_t = \vec{f}_t(\vec{x}_t, \mathcal{B})$. Although this reduces the computational cost of simulations, it introduces inaccuracies in the dynamics by eliminating longitudinal librations of other frequencies and all latitudinal librations.

2.3. Normal modes and damping

The rotational equations of motion Equation 4b can be linearized for small angles ε around each axis of the

[1] *TU Delft Astrodynamics Toolbox*, the software used in this work. See https://docs.tudat.space/en/latest/.

Phobos-fixed frame, yielding Equation 11a for the evolution of each small angle (Rambaux et al., 2010), where f is the appropriate component of the torque - the *forcing*. In the homogeneous case (for $f = 0$), this equations still yields an oscillatory solution, with a frequency of oscillation ω_o. This oscillation is called the *rotational normal mode*, and there exists one for each axis of the Phobos-fixed frame. Because there are no elements in Equation 11a that are external to the body if $f = 0$, these normal modes are not characteristics of the dynamical environment but rather physical properties of the body itself.

$$\ddot{\varepsilon} + \omega_o^2 \varepsilon = f \tag{11a}$$

$$\varepsilon = \sum \frac{f_i}{\omega_o^2 - \omega_i^2} \sin(\omega_i t) \tag{11b}$$

In the general case where $f \neq 0$, oscillations appear at an infinite range of frequencies. In the context of rotating moons - and more specifically Phobos - where oscillations about the moon's three axes are called librations (see subsection 2.2), these oscillations excited by forcings are called *forced librations*. These forced librations about each axis are given, in the linearized case, by the solution to Equation 11a, namely Equation 11b (Rambaux et al., 2010), where f_i and ω_i are the amplitudes and frequencies of all the components that make up the forcing f.

There are two things to point out in this equation. On one hand, the components of the forcing that oscillate close to the normal mode will produce a big librational response as opposed to those components for which ω_i is further from ω_o. This is particularly important for Phobos because its longitudinal normal mode is close to the orbital mean motion, a frequency at which is only natural that forcings oscillate. On the other hand, the normal mode itself is not present as one of the frequencies at which the libration oscillates. This is because damping is assumed to have already existed over long time scales, making the normal modes disappear.

There exist analytical expressions for the frequencies of the normal modes collected by Rambaux et al. (2012) and gathered in this work in Equation 12, where ω_{lon}, ω_{lat} and ω_{wob} are the longitudinal, latitudinal and wobble normal mode frequencies and $A \leq B \leq C$ are Phobos' main moments of inertia. The last of these is an oscillation about Phobos' x-axis.

$$\omega_{\text{lon}} \approx n\sqrt{3\sigma} \tag{12a}$$

$$\omega_{\text{lat}} \approx n\sqrt{\frac{(1 + 3\beta + \alpha\beta) + \sqrt{\Delta}}{2}} \tag{12b}$$

Table 1: Frequencies in rad/day of all three normal modes, as computed with Equation 12, compared to those obtained by Rambaux et al. (2012). Differences stem from the different inertia properties used in each work.

	ω_{lon}	ω_{lat}	ω_{wob}
This work	12.354	27.165	7.336
Rambaux et al. (2012)	12.275	27.270	7.498

$$\omega_{\text{wob}} \approx n\sqrt{\frac{(1 + 3\beta + \alpha\beta) - \sqrt{\Delta}}{2}} \tag{12c}$$

$$\Delta = (1 + 3\beta + \alpha\beta)^2 + 16\alpha\beta \tag{12d}$$

$$\alpha = \frac{C - B}{A} \qquad \beta = \frac{C - A}{B} \qquad \sigma = \frac{B - A}{C} \tag{12e}$$

Table 1 collects the values of all three normal modes as computed by Equation 12, and compared to those obtained by Rambaux et al. (2012). The largest difference between the two computations is in ω_{wob}, where they differ by 2%. The differences in the other two frequencies are below 1%. Such a good agreement serves to show consistency between the gravity field developed by Maistre et al. (2019) used in this work to compute the moments of inertia (a detailed explanation of how this is done can be found in Appendix A), and the moments of inertia derived by Willner et al. (2010) and used by Rambaux et al. (2012).

Equation 11b is also representative of Phobos' longitudinal rotational kinematics in the present day. The normal modes are not observed anymore because damping has made them disappear over the history of the Solar System. However, when Equation 11a is integrated - and more generally Equation 4b - both the normal modes and the forced response will arise. Unless a physically realistic initial state is used, one needs to forcefully remove the normal modes from the solution. In this work, this is done in the same way as presented by Rambaux et al. (2012), which is to introduce a damping algorithm and add a virtual torque in the equations of motion. This virtual torque is computed as to preserve the average rotation of Phobos around its z-axis while opposing any other rotation. The dynamics are propagated forward in time with the torque, and the final state is used to propagate the dynamics backwards without the torque. This procedure is performed several times in an iterative process to generate the initial state used to propagate Phobos' dynamics. Specific details on this algorithm and the computation of such torque can be found in Appendix C.

2.4. Self-inconsistency of the concept of librations

As seen in subsection 2.1, the concept of "libration" simply does not exist in the real-life dynamics of Phobos, mathematically represented by the equations of motion. Thus, when librations are introduced in the propagation of an uncoupled translational model to represent the orientation of Phobos, they should always be understood, in a way, as useful yet artificial constructs that are computed with actual quantities of the motion - like position, velocity or the Keplerian elements. For instance, Equation 8b gathers the most popular representation of the most popular librational component, the once-per-orbit longitudinal libration. It is given in terms of the eccentricity of Phobos' orbit and the mean anomaly of Phobos. This artificial nature of librations is exacerbated in a non-Keplerian dynamical environment where the strict definition of orbit becomes dubious, in the sense that an abstract "instantaneous" ellipse needs to be defined at each instant of time. This renders the Keplerian elements time-changing, i.e. the so-called *osculating elements*. In this scenario, the term *once-per-orbit* becomes ill-defined.

In particular, with the mean motion changing with time, forcing the longitudinal libration angle to oscillate at a frequency equal to the mean motion requires to either compute an average mean motion or use the osculating mean motion and accept that the libration angle is going to oscillate at different frequencies. However, if average Keplerian elements are used for its computation, one runs the risk of making the definition of the libration angle incompatible with the translational state in short time scales, and therefore misrepresent Phobos' orientation relative to Mars - which renders the computation of state derivatives wrong.

The software used in this work - *Tudat* - uses the longitudinal libration angle implementation presented by Lainey et al. (2019), who uses the approximation in Equation 13a, valid for small eccentricities, to write Equation 13b. Here, E is the eccentric anomaly of Phobos. This leads to the implicit use of osculating Keplerian elements, namely the quantity in Equation 13b will oscillate at different frequencies, mostly those contained in the mean motion itself. This is very well illustrated in Figure 3, where the frequency content of the *once-per-orbit* longitudinal tidal libration ψ has been plotted together with the frequency content of the mean motion. As can be seen, the frequency content of ψ has a main peak at the average mean motion, but has large peaks at other frequencies, corresponding to the frequencies of the osculating mean motion n - the largest of them occurring at integer multiples of the average mean motion.

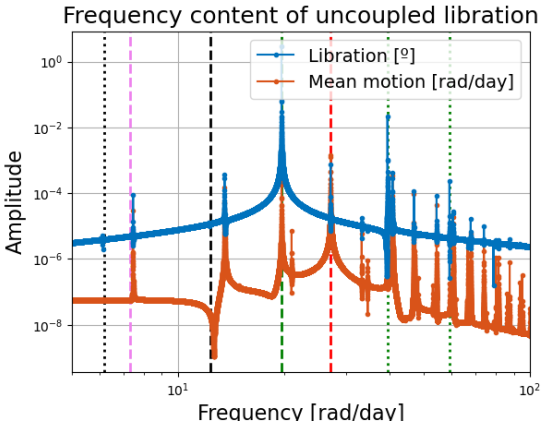

Figure 3: Frequency content of the longitudinal libration of an uncoupled translational state in which a fully locked configuration of Phobos has been assumed, together with a once-per-orbit longitudinal libration.Dashed vertical lines indicate the average mean motion (green), and the three normal modes: longitudinal (black), latitudinal (red) and wobble (violet). Dotted lines are integer multiples/divisors of dashed lines.

$$e \sin M \approx e \sin E \approx \frac{\vec{r} \cdot \vec{v}}{\left|\vec{r} \times \vec{v}\right|} \tag{13a}$$

$$\psi = -\mathcal{B} e \sin M \approx -\mathcal{B} \frac{\vec{r} \cdot \vec{v}}{\left|\vec{r} \times \vec{v}\right|} \tag{13b}$$

The fact that the implementation of the *once-per-orbit* longitudinal libration angle produces contradictory results in which its frequency content presents peaks at frequencies other than the *average* mean motion might be - and will likely be - an inherent limitation to the use of librational models when high fidelity models of Phobos' dynamics are required. The aim of this work is to quantify the impact of this mis-representation of Phobos' orientation made by librational models on its translational dynamics. This will serve as an indication of which applications accept the use of librational models, and which ones do not.

2.5. Model variations

In order to study the couplings between Phobos' translational and rotational dynamics, the equations of motion (Equation 5) have been integrated both in a coupled manner and an uncoupled manner - from now on the *coupled model* and the *uncoupled model* respectively.

The uncoupled model integrates Phobos' translational equations of motion (Equation 5a) independently from the rotational equations of motion (Equation 5b).

In this uncoupled model, an a-priori rotational state vector history $\vec{x}_r$ has been imposed, such that Phobos is in a fully locked configuration - its long axis always pointing directly towards Mars - with the addition of the once-per-orbit tidal longitudinal libration of amplitude $\mathcal{B}e$. This angle is computed as in Equation 8b, the factor $e \sin M$ computed as in Equation 13a.

The coupled model, however, integrates both the translational and rotational equations of motion simultaneously. This requires the execution of the damping algorithm discussed in subsection 2.3 prior to the actual propagation so that a realistic initial state is obtained.

In order to fully isolate the effects of couplings, the coupled and uncoupled models have been made as similar as possible to each other by using the same initial state and gravity coefficients for both. Furthermore, the Fourier transform of Phobos' tidal longitudinal librations as computed by the coupled model is used to compute the amplitude of the oscillation with frequency that of the orbital mean motion, which is used as amplitude $\mathcal{B}e$ for the uncoupled model. Because the initial state is an output of the damping algorithm, the algorithm is executed on the coupled model and the translational part of the resulting initial state vector is used as initial state for the uncoupled model.

As explained in section 3, all these equivalences do not apply during estimation, where one or more of those parameters are estimated.

2.6. Role of couplings in propagation

The fundamental difference between the coupled and uncoupled models are Phobos' librations that the rotational equations of motion (Equation 4b) will generate but that are not modelled by an uncoupled model implementing Equation 8. This comprises all "minor" librations in longitude - those at frequencies other than the mean motion - and the librations in latitude. In evaluating Phobos' acceleration on itself through Equation 2, variables λ and ϕ are Phobos' longitudinal and latitudinal libration angles, bundling together all librations of each kind. If only the quadrupole field ($C_{2,0}$ and $C_{2,2}$) is considered - as done in this work - the out-of-plane component of Phobos' acceleration on itself is proportional to $\sin\phi$. This means that (a) latitudinal librations are required for this out-of-plane component to exist and (b) the contribution of longitudinal librations to this out-of-plane component will be small if the latitudinal libration angle is small. Borderies and Yoder (1990) also hint at all longitudinal librations contributing to the secular part of Phobos' potential. Differences between the coupled and uncoupled trajectories are therefore expected to contain a comparatively small out-of-plane component driven by the (small) latitudinal librations and a secular in-plane component driven by minor longitudinal librations.

3. Estimation

Using the same model parameters - initial state, libration amplitude and gravity field - for both the coupled and uncoupled model will inevitably create differences in the propagated states, because $\vec{x}_r$ in Equation 5 is different in both. However, in quantifying how valid it is to use an uncoupled model in place of a coupled model, it's required to find those conditions in which the two models behave most alike, and look at what differences still remain. This has been done by means of estimations, and this section will explain what types of estimations have been performed and why.

The section will begin by defining what is meant by *estimation* and *estimator* in the present work, as well as the notation used for the different relevant elements of the estimation problem. This will be followed by an explanation of the role that couplings play in this estimation process. Finally, the two main elements of the estimation will be presented, i.e. the observations (and observation model) and the estimated parameters (and estimtion model).

3.1. The estimation problem

Provided a set of observations $\vec{z}$ either obtained from reality or generated with a simulation model, a set of differential equations - from now on the *estimation model* - can be used to replicate them, providing the so-called model values $\vec{h}$. The equations in this estimation model contain some dynamic parameters, collected in a vector $\vec{y}$ that will determine the value of $\vec{h}$, so that $\vec{h} = \vec{h}(\vec{y})$. The *estimation* will be understood as the process of finding a vector $\vec{y}^*$ such that the differences between $\vec{z}$ and $\vec{h}$, called residuals and defined as in Equation 14a, are minimized. The estimator is the method by which the estimation is performed. In this work, a non-linear least squares estimator is used.

Least-squares means that the quantity to be minimized is the sum of the squares of the residuals, mathematically written as $J = \vec{\varepsilon}^T\vec{\varepsilon}$ under the assumption that all observations in $\vec{z}$ have the same associated uncertainty. On the other hand, because the problem at hand is inherently non-linear, the model values are linearized around a reference $\vec{h}_o = \vec{h}(\vec{y}_o)$ and one can define the residuals as in Equation 14b, where $\boldsymbol{H} = \nabla\vec{h}(\vec{y}_o)$ is usually called the *design matrix* and $\Delta\vec{y} = \vec{y} - \vec{y}_o$.

$$\vec{\varepsilon} = \vec{h} - \vec{z} \tag{14a}$$

$$\vec{\varepsilon} \approx \vec{h}_o + \boldsymbol{H}\Delta\vec{y} - \vec{z} = \boldsymbol{H}\Delta\vec{y} - \Delta\vec{z} \tag{14b}$$

Then, an iterative process begins, each iteration consisting of computing $\Delta\vec{y}^*$ that minimizes J with this linear model for $\vec{h}$ around a reference $\vec{y}_o$ and updating the reference to $\vec{y}_1 = \vec{y}_o + \Delta\vec{y}^*_o$. This new reference is used to linearize $\vec{h}$ in the next iteration. The parameter update $\Delta\vec{y}^*$ is computed by solving the so-called normal equations in Equation 15. Note that, at each iteration, all the elements in this equation will be different: the normal matrix is computed at each reference $\vec{y}_k$ and $\Delta\vec{z}$ is also computed using the different references for the model values, $\Delta\vec{z}_k = \vec{z} - \vec{h}_k$.

$$\left(\boldsymbol{H^T H}\right)\Delta\vec{y}^* = \boldsymbol{H^T}\Delta\vec{z} \tag{15}$$

The end of the iterative process is defined by some convergence conditions. In this work, the only stopping criterion has been a maximum number of iterations.

3.2. Observation simulation

This work has made used of simulated observations in all the performed estimations, which means that $\vec{z}$ as defined in the previous subsection has been generated using simulations. Observations have been generated using the coupled model.

Observations consist of position observables. This means that the word *observation* in this work is to be understood as a position vector, more specifically the position vector of Phobos with respect to Mars, with the components expressed in the J2000 reference frame (see subsection 2.1). These observations have been generated every 20 minutes, which means a ∼15.5° spacing in Phobos' orbit between two consecutive observations. A preliminary analysis of this frequency was performed by running estimations with observations generated every 10 minutes, and the results were the same. Observations start 1h after the beginning of the estimated arc and finish 1h before the end of the estimated arc.

Observations are noiseless and ideal, meaning that there will be no uncertainty associated to them.

With respect to the elements defined in the previous subsection, $\vec{z}, \vec{h}, \vec{\varepsilon} \in \mathbb{R}^{3n_o \times 1}$, where n_o is the number of observations, each of which has three components. If a number n_p of parameters are estimated, then $\vec{y} \in \mathbb{R}^{n_p \times 1}$ and $\boldsymbol{H} \in \mathbb{R}^{3n_o \times n_p}$.

3.3. Role of couplings in estimation

Consider a set of parameters $\vec{y}_o$ (e.g. the initial state $\vec{x}_o$) with which the coupled model has been propagated. Using these parameters, the coupled model produces a state history $\vec{x}_c(t, \vec{y}_o)$. If an estimation is performed in which the observations are taken from $\vec{x}_c(t, \vec{y}_o)$ and then an uncoupled model is used as estimation model, the vector of residuals can be written as in Equation 16, where $\vec{x}_u(t, \vec{y})$ is the model values produced by the uncoupled model when the set $\vec{y}$ of parameters is used. Note that, because $\vec{x}_c$ and $\vec{x}_u$ are different by definition, $\vec{\varepsilon}(t, \vec{y}_o)$ will not be nil and the solution to the corresponding least squares problem will be some vector $\vec{y}^* = \vec{y}_o + \Delta\vec{y}^* \neq \vec{y}_o$.

$$\vec{\varepsilon}(t, \vec{y}) = \vec{x}_u(t, \vec{y}) - \vec{x}_c(t, \vec{y}_o) \tag{16}$$

The parameter increment $\Delta\vec{y}^*$ will appear in order to account for the differences in $\vec{x}(t)$ generated by couplings. In other words, the effect that couplings have on the trajectory will be *absorbed* by this $\Delta\vec{y}^*$. If this *absorption* is perfect and the resulting $\vec{y}^*$ is such that $\vec{\varepsilon}(t, \vec{y}^*) = \vec{0}$, one could effectively propagate the dynamics of Phobos with an uncoupled model combined with $\vec{y}^*$ to obtain the exact same result as they would using a coupled model combined with $\vec{y}_o$. This is convenient for state propagation, as it allows to simplify the dynamics if the parameters are chosen appropriately. This is never the case, and although $\vec{\varepsilon}(t, \vec{y}^*)^T \vec{\varepsilon}(t, \vec{y}^*)$ is indeed smaller than $\vec{\varepsilon}(t, \vec{y}_o)^T \vec{\varepsilon}(t, \vec{y}_o)$, it is never 0. Absorption is then said to be *imperfect* and some residuals are left, representing a part of the effects that could not be absorbed by any of the parameters.

When it comes to estimation, however, absorption is usually an inconvenient. Absorbing the effect of couplings into the parameters contaminates the solution and makes it differ from the *true* $\vec{y}_o$. This is the scenario in current state-of-the-art estimations. Phobos' real life dynamics incorporate, by definition, all possible couplings, while state-of-the-art estimation models are uncoupled. In trying to estimate the values of $\vec{y}_o$ through estimation, a solution $\vec{y}^*$ is instead obtained, which contains the bias $\Delta\vec{y}^*$, while $\vec{y}_o$ remains unknown. The aim of this work is to quantify this bias $\Delta\vec{y}^*$. This $\vec{y}$ often includes the once-per-orbit longitudinal libration angle or Phobos' gravity coefficients $C_{2,0}$ and $C_{2,2}$, all of these containing information about Phobos' interior. Mis-estimation of these parameters effectively results in mis-information about the interior structure of Phobos.

3.4. Estimated parameters

We have performed estimations using the uncoupled model as estimation model and the coupled model as

truth model. When different parameters are estimated, a combination of uncoupled model and dynamical parameters is obtained that emulates the coupled model as best as possible. Residuals are the differences that the uncoupled model is not able to represent no matter what. As explained in subsection 3.3, the estimated parameters will be mis-estimated due to couplings.

Three different estimation sets have been performed, estimating different parameters each. They respond to typical estimations, as mentioned in section 1. These sets estimate:

- Set 1: Initial translational state, $\vec{x}_{t,o}$
- Set 2: Initial translational state and once-per-orbit longitudinal libration amplitude, $\vec{x}_{t,o}$ and $\mathcal{B}$ (like Jacobson (2010) or Lainey et al. (2021))
- Set 3: Initial translational state and Phobos' normalized quadrupole gravity coefficients, $\vec{x}_{t,o}$, $\overline{C}_{2,0}$ and $\overline{C}_{2,2}$ (like Lainey et al. (2007))

The first set will provide a baseline as to how well the uncoupled model can emulate the coupled model when the rest of the parameters is the same. Comparisons of other estimations with this one will quantify how well other dynamical parameters can absorb the effects of couplings. The second and third set represent typical es-

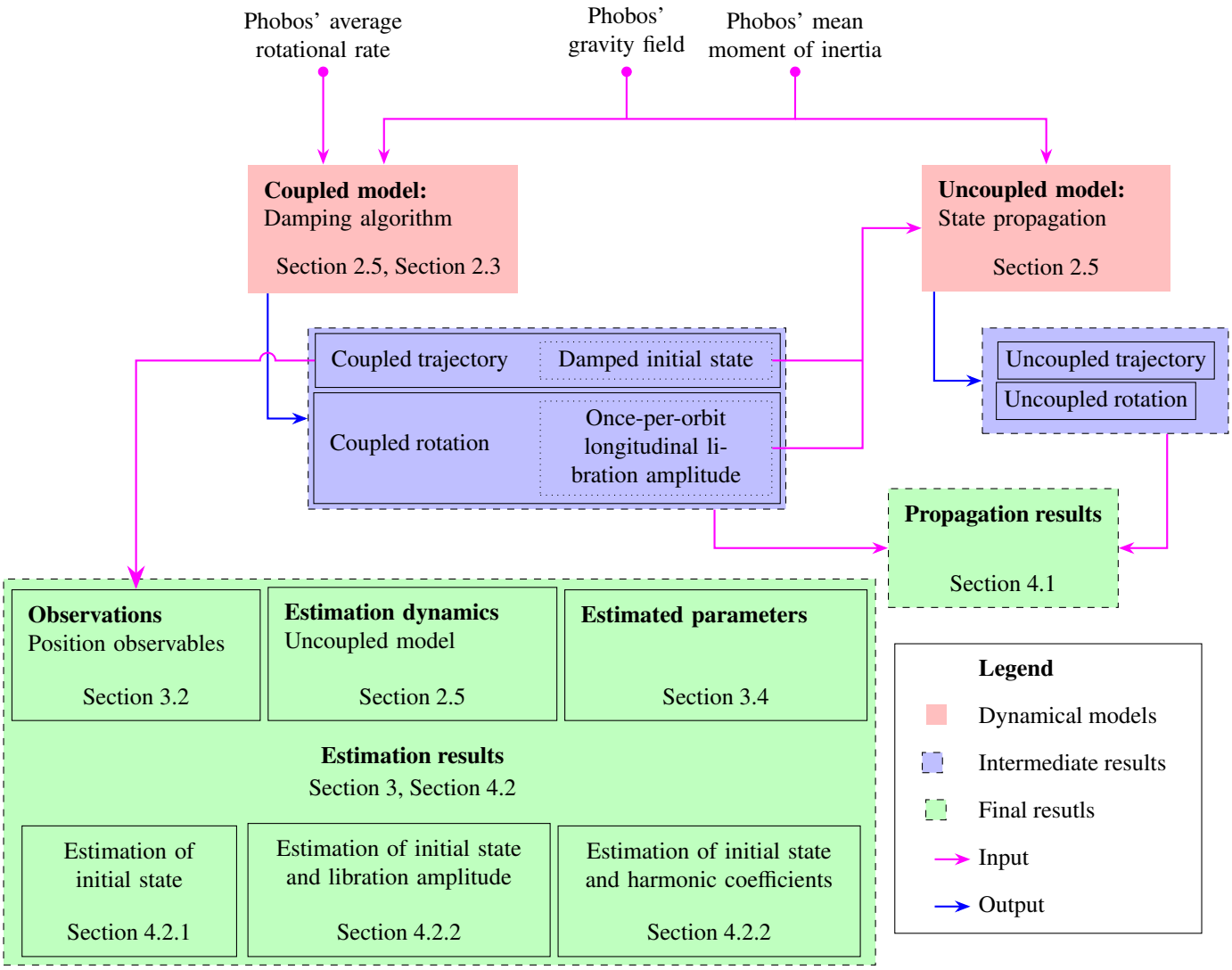

Figure 4: Schematic of the work done in this paper.

timation schemes in state-of-art studies of Phobos. Set 2 is the one used by Jacobson (2010) or Lainey et al. (2021), while Set 3 is the one estimated by e.g. Lainey et al. (2007). Results of these estimations, in particular of sets 2 and 3, will quantify how well an uncoupled model can emulate a coupled model - for which residuals will have to be studied - and how much the estimated parameters are *contaminated* by the dynamical mismatch of couplings.

4. Results

This section will gather the results obtained through simulations. There are two big groups in which results can be categorized: state propagation and parameter estimation. The effect of couplings was analyzed by making the coupled and uncoupled models as physically similar as possible, as was explained in subsection 2.5, and comparing how they propagated the same translational initial state. How couplings impact the results of estimations was studied through the analysis explained in subsection 3.3. A flowchart summarizing the procedure followd in this work is provided in Figure 4.

In the remainder of the text, extensive use will be made of the so-called *RSW* frame. At any point of a trajectory, one can define a reference frame formed by the right-handed triad $\{\hat{r}, \hat{s}, \hat{w}\}$. Unitary vectors $\hat{r}$ and $\hat{w}$ are parallel to the instantaneous position and angular momentum vectors, while $\hat{s}$ completes the triad. The *RS* plane corresponds to the plane of the instantaneous elliptical orbit (in-plane), while the *W* direction is the direction perpendicular to it (out-of-plane).

4.1. State propagation

As a first approach to the study of couplings, the same initial state was propagated using two different models, the uncoupled model and the coupled model, which have been made as similar to each other as possible as explained in subsection 2.5, for a total of 81920 hours (around 9 years and 4 months). There are two main areas in which the differences between these two simulation results are interesting: translation and rotation.

4.1.1. Translation

For an order-of-magnitude context, Figure 5a shows that the norm of position differences between the coupled and uncoupled trajectories accumulate to ~40 m.

The time dependence of all three components can be seen in Figure 5b. As expected, the along-track component shows a secular trend (the uncoupled trajectory gets ahead of the coupled one) superimposed by oscillations of ever-increasing amplitude. The radial and out-of-plane components lack that secularity, and just oscillate around 0 with a growing amplitude of up to 4 m at the end of the integration time. The largest of these oscillations occurs at the orbital frequency of the mean motion n, as seen in Figure 5c. Oscillations in the order of millimeters are present at frequencies very close to the latitudinal normal mode ($\omega_{\text{lat}} = 27.27$ rad/day), a frequency close to which Rambaux et al. (2012) identified a resonant forcing. Rambaux et al. (2012) notes that these frequencies are due to oscillations in Phobos' inclination and changes in the secular part of the mean anomaly, and the fact that there exist differences at this frequency between the coupled and uncoupled model indicates that this libration still has some influence on the orbit that, although small, cannot be accounted for by uncoupled rotational models.

Insight is gained when looking at the Keplerian elements. With fundamental differences between the coupled and uncoupled models being in the orientation of Phobos, the orbital energy as measured by the semi-major axis of the orbit should not change. Figure 5d shows that, although it presents small oscillations in the order of centimeters, the mean semimajor axis remains constant when couplings are introduced. The main differences in position were seen to be a secular trend in along-track position and the onset of out-of-plane oscillations (Figure 5b). In terms of keplerian elements, the latter is mostly contained in the inclination of the orbit. The dominant frequency of the inclination is 0.01 rad/day, driving the low-frequency oscillations in the RSW components of the effects of couplings, as mentioned above.

$$\dot{\Omega} + \dot{\omega} = -\frac{3}{4} n \left(\frac{R}{a}\right)^2 \left[2C_{2,0} + \sigma \frac{I_{zz}}{MR^2} \frac{5 + 9\sigma}{1 - 3\sigma}\right] \quad (17)$$

On the other hand, secular effects of couplings in along track direction can be identified to be qualitative similar to those of the once-per-orbit longitudinal libration. In this regard, Equation 17 (Borderies and Yoder, 1990) indicates that the once-per-orbit libration amplitude induces a decreasing linear trend in $\Delta\Omega + \Delta\omega$. Here, n, I_{zz}, M, R and a are Phobos' mean motion, polar moment of inertia, mass, reference radius and semi-major axis, while σ is the inertia ratio from Equation 12e. The fact that such a trend is observed in Figure 5d (yellow line) with a slope of 18 mas/day owes to the fact that couplings induce the same in-plane motion as the once per-orbit libration, which was expected from the fact that all longitudinal librations - once-per-orbit or otherwise - are bundled together in Mars' Phobos-fixed

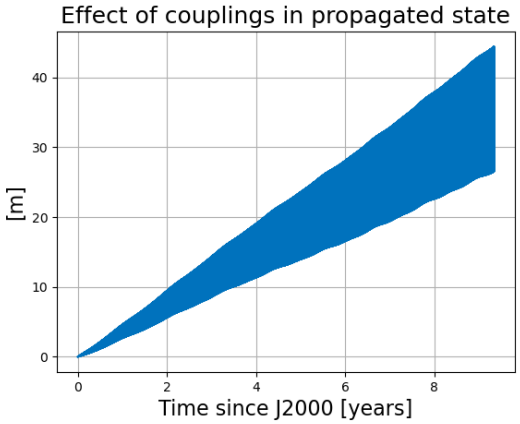

(a) Norm of position difference between the states propagated by the uncoupled model and those propagated by the coupled model.

(b) Time evolution of the RSW components of the position differences between the coupled and uncoupled trajectories.

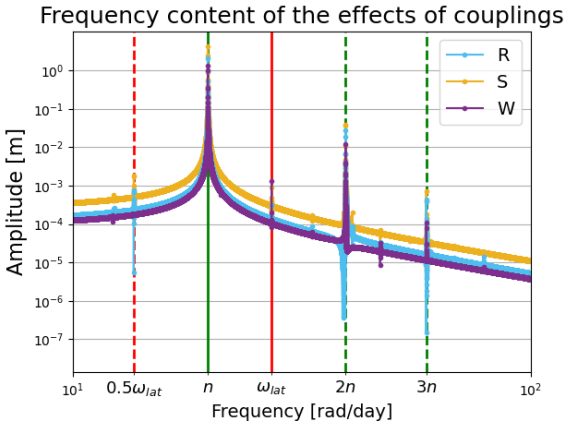

(c) Frequency content of the RSW components of the position differences between the coupled and uncoupled trajectories.

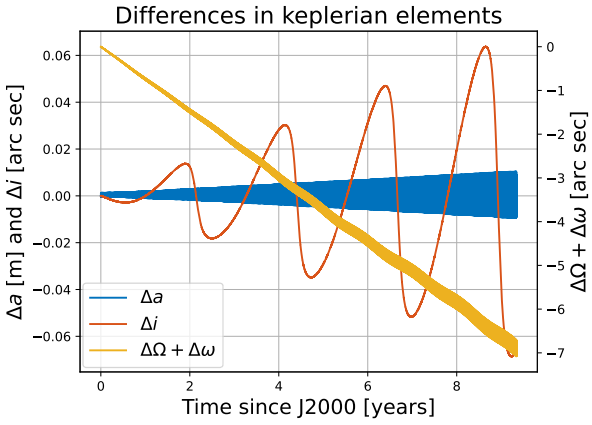

(d) Differences in selected Keplerian elements between the coupled and uncoupled trajectories.

Figure 5: Propagation results. The differences in position is studied in different ways: norm (top left), components (top right), frequency content (bottom left) and Keplerian elements (bottom right). Vertical lines in the bottom right picture represent (multiples of) the mean motion (n) and latitudinal normal mode (ω_{lat}).

longitude in the evaluation of Phobos' gravitational potential (Equation 2). This is reinforced by the similarities between the in-plane effects of couplings and the once-per-orbit libration after the 9 years and 4 months of simulation, seen in Figure 6a. The out of plane effects (Figure 6b), however, are completely different. In the context of parameter estimation, this points at the once-per-orbit libration amplitude having a lot of potential in absorbing the effects of couplings, which means that it will likely be mis-estimated in minimizing the in-plane components of the residuals generated by couplings.

Differences in rotational motion can be divided in two axes: longitudinal and latitudinal differences. The uncoupled model, by definition, produces no latitudinal librations because Phobos' orbital and equatorial planes are always coincident, so it would be trivial to assess the effects of couplings in this sense. It is still of interest to study the latitudinal librations produced by the coupled model. Table 2 collects the five largest peaks of the frequency spectrum of the tidal latitudinal librations, i.e. equivalent to Mars' Phobos-fixed latitude. In studying these types of librations instead of the *physical* librations, the low-frequency orbit-induced effects are removed. In these lines, tidal latitudinal librations are purely associated with high-frequency forcings, which are amplified if they are close to Phobos' normal modes. It is to be noted that the first two components in Table 2 correspond to the 2nd and 5th terms tabulated by Rambaux et al. (2012), attributed to resonances with the latitudinal and wobble normal modes, $\omega_{\text{lat}} = 27.165$

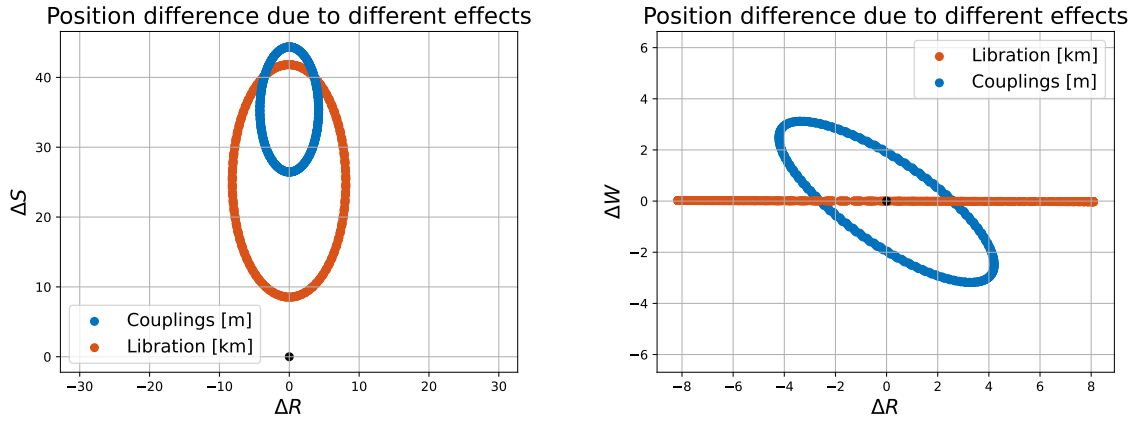

(a) In-plane projection of position differences.

(b) Out-of-plane projection of position differences

Figure 6: Comparison between the position differences between the coupled and uncoupled trajectories (blue) and the position differences between the uncoupled and fully-locked trajectories (orange). Only the final 10 orbits of the 9 years and 4 months have been plotted. Note the different units.

Table 2: Strongest components of latitudinal tidal librations from the coupled model.

Freq. [rad/day]	Amp. [mdeg]
27.1547	8.48481
7.46106	5.09929
19.7102	0.809964
12.2326	0.448258
46.8503	0.197696

Table 3: Main peaks of the tidal longitudinal libration as computed by the coupled and uncoupled models

Frequency [rad/day]	Amplitude [mdeg]	
	Coupled	Uncoupled
39.3887	25.1998	21.5162
13.5769	3.5805	0.3672
27.1557	1.5757	0.7545
59.0831	0.36885	0.23865
12.2643	0.25452	—
7.4613	0.12578	0.08761

rad/day and $\omega_{\text{wob}} = 7.336$ rad/day. The third term in Table 2 occurs at the orbital frequency of the mean motion, while the fourth corresponds to a resonance with the longitudinal normal mode $\omega_{\text{lon}} = 12.354$ rad/day.

On the other hand, longitudinal librations are present in both the coupled and uncoupled models. As a reminder, the uncoupled model should ideally only contain one single librational component at the orbital frequency. It was shown in subsection 2.4 that this is however not the case. Nevertheless, with the coupled model introducing the phenomenon of resonance for weak forcings at frequencies close to the normal modes (see subsection 2.3), it is expected to have a richer frequency spectrum particularly around normal modes, while the once-per-orbit libration amplitude should be exactly the same in both models - as explained in subsection 2.5. Table 3 collects the most important peaks obtained from a frequency decomposition of the Phobos-fixed longitude of Mars - Phobos' tidal longitudinal librations. The amplitudes produced by both the coupled and uncoupled models have been tabulated for comparison. The once-per-orbit libration has been left out because the amplitude obtained from the coupled model was imposed on the uncoupled model. As a point of reference, the first and second peaks in this table can be correlated to the second and fifth terms in Table 4 by Rambaux et al. (2012). Of particular interest is the fact that the peak at 12.2643 rad/day, close to the longitudinal normal mode ω_{lon} (see Table 1) is not produced by the uncoupled model because this model does not incorporate resonances between dynamical forcings and Phobos' normal modes.

Phobos' once-per-orbit longitudinal libration amplitude can be extracted from the results of the coupled model, producing a scaled tidal libration amplitude of $\mathcal{B} = 3.29918$ rad (the one used for the uncoupled model in this work), which can be compared to the analytical prediction of Equation 10, i.e. $\mathcal{B} = 3.29807$ rad. The error between the two values is of 0.03%, which translates in an error of 10^{-3} degrees in the amplitude of the once-per-orbit physical libration amplitude. Note that

the analytical prediction was developed in the context of uncoupled models, and their predictions matching so well with the result of a coupled propagation indicates that uncoupled models can naturally replicate the once-per-orbit libration amplitude of the complex coupled dynamics of Phobos.

4.2. Parameter estimation

This subsection will quantifying the absorption that an uncoupled model produced on estimated parameters when a coupled model is used as truth to generate observations. Similarly, the remainder effects that cannot be absorbed, observed in estimation post-fit residuals, will be studied as well.

This will be done in a systematic analysis of the estimation sets presented in subsection 3.4, which will be performed for different arc lengths up to 250 days. All estimations start at the same epoch t_o (1 year after the J2000 epoch). In assessing the quality of the estimation, the residuals and estimated parameter difference from truth will be used as figures of merit. The former will be studied both as norms and as RSW components.

4.2.1. Estimation of initial state

First, an estimation of initial state is performed with the uncoupled model, using observations generated by the coupled model. Looking at the results of this estimation will allow to isolate the effects of estimating additional dynamical parameters by providing a baseline as to how estimating *only* the initial state brings the uncoupled model closer to the coupled model. Then, residual reduction observed in further estimations will

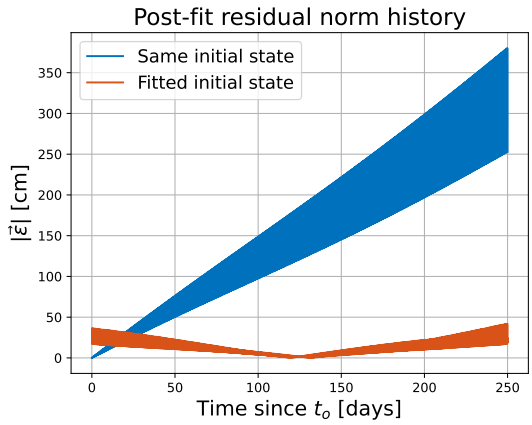

(a) Differences between the coupled and uncoupled trajectories when the same initial state is used and when the best-fit estimated initial state is used for the uncoupled model.

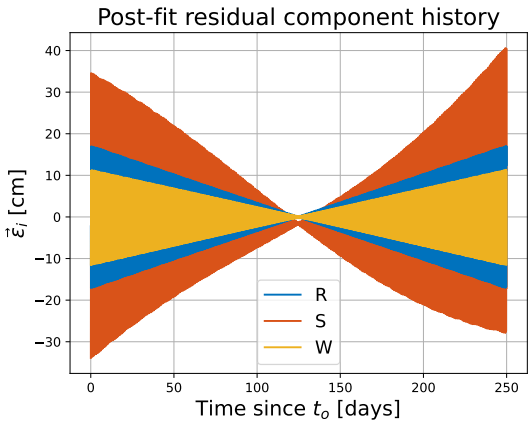

(b) Time history of the RSW components of residuals.

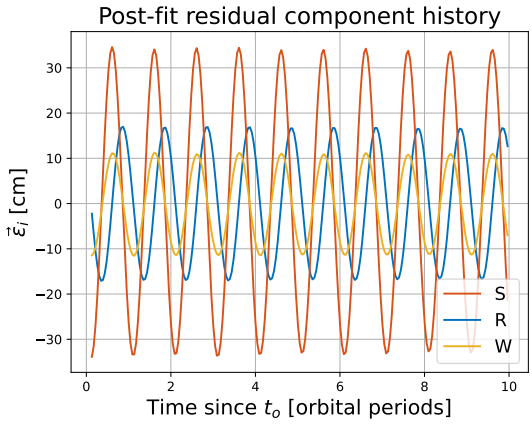

(c) First 10 orbits of the component-wise residual history of a 250-day estimation of initial state.

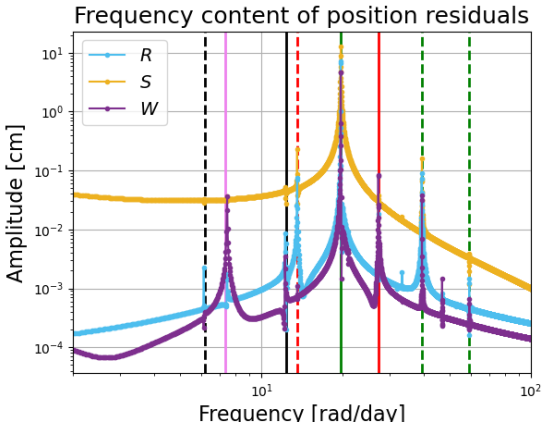

(d) Frequency content of residual components. Vertical lines indicate the mean motion (green) and the three normal modes: longitudinal (black), latitudinal (red) and wobble (violet). Dashed lines are multiples/divisors of solid lines.

Figure 7: Residuals of a 250-day estimation of initial state. A coupled model was used for observations and an uncoupled model for estimation.

be solely due to the estimation of additional dynamical parameters when compared to the present estimation of initial state.

In this estimation, focus will be put on an analysis of residuals. These residuals will will provide insight on what effects the initial state cannot absorb and will represent an upper bound for residuals of latter estimations. Residuals that remain in latter estimations will represent effects that additional parameters cannot absorb, while improvements will represent effects of couplings that additional parameters can absorb.

Couplings were seen to impact the along-track motion in a more significant way than the R or W components (see subsection 4.1), with the uncoupled orbit mostly getting ahead of the coupled orbit. This is expected to translate, in the context of an estimation of initial state, as bigger along-track components of residuals as opposed to the R and W components, so that the estimated orbit starts behind observations and it eventually gets ahead of them - meaning the initial correction will be in the negative $\hat{s}$ direction. As an order of magnitude reference, Figure 7a shows how fitting the initial state reduces the differences between the coupled and uncoupled models, in terms of the norm of the position differences between the two. The blue line shows the differences between the two propagations if the same initial state is used in both, while the red curve shows the differences between the two when the fitted initial state is used to propagate the uncoupled model. Then, Figure 7a shows that differences are reduced by a whole order of magnitude, from a maximum of around 3.5 m to below 50 cm. Recalling Equation 16, the blue line would correspond to $|\vec{\varepsilon}(t, \vec{y}_o)|$ while the red line would correspond to $|\vec{\varepsilon}(t, \vec{y}^{\,*})|$. There is of course a $\Delta\vec{y}^{\,*}$ associated with this reduction, given in this case in Equation 18 in terms of the difference in position ($\Delta\vec{\rho}$) and velocity ($\Delta\vec{\eta}$) in RSW components. As expected, the S component of the position error is negative and the largest of the three in absolute terms. The R and W components, on the other hand, are comparable to each other and much lower than the S component. In any case, the error in the estimated position is in the order of centimeters, while the error in the estimated velocity is in the order of micrometers per second.

$$\Delta\vec{\rho}_o = \begin{bmatrix} 10.62 \\ -26.74 \\ -8.27 \end{bmatrix} \text{ cm} \quad \Delta\vec{\eta}_o = \begin{bmatrix} 29.50 \\ -24.17 \\ -17.63 \end{bmatrix} \times 10^{-6} \text{ m/s} \quad (18)$$

As expected from such a fit, the norm of the residuals - red curve in Figure 7a - seems to reach a minimum at the center of the arc (meaning that all three components are 0), and increases to reach its maximum at the two ends of the arc. A quantitative analysis can be done on the basis of Figure 7b. On the one hand, the S component is, as expected, the largest component of the residuals, reaching 30 cm at the ends of the arc, while the W component is the smallest one and reaches maxima of around 12 cm. All three of them feature fast, large oscillations - better observed in Figure 7c - which seem to have a dominant frequency equal to the mean motion. It is then of interest to take a look into what frequencies make up these oscillations. A Fourier decomposition of all three components can be seen in Figure 7d. Indeed, the dominant frequency is that of the mean motion n, with contributions at millimeter level of twice the mean motion and close to half the frequency of the latitudinal normal mode. Furthermore, there are also a series of peaks at sub-mm level that, although irrelevant in the current estimation - because residuals are at the level of several centimeters - they all can be correlated to frequencies close to the normal modes, at which forcings are amplified by resonance and significant librations were observed. Once again, the slow frequencies of the residuals components have been cropped out of Figure 7d for clarity, but they all show large oscillations below 0.1 rad/day and at around 0.01 rad/day, coincident with the long term orbit-induced effects mentioned in subsection 4.1.

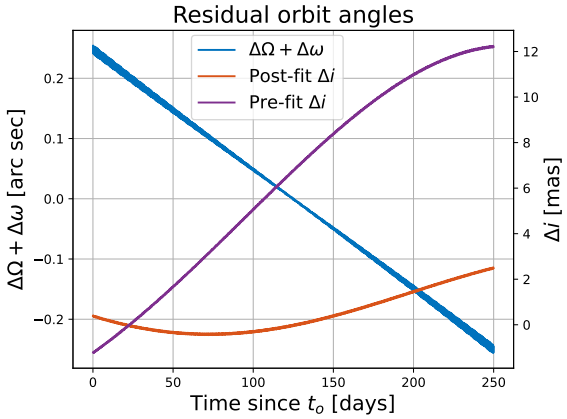

Figure 8: Differences in inclination and $\Omega + \omega$ between observed and estimated trajectories.

Geometrical insight is gained when the analysis of residuals is carried out on the basis of Keplerian elements, in particular of the orbit's Euler angles (Ω, i and ω). Their evolution can be seen in Figure 8. Because none of the terms in Equation 17 are changed in an estimation of initial state alone, the secular drift of $\Delta\Omega + \Delta\omega$ is the same in both Figure 5d (differences between coupled and uncoupled trajectories for same initial state)

and Figure 8 (differences for fitted initial state), namely $\dot{\Omega}+\dot{\omega} = 18$ mas/day. Figure 8 also contains both the pre-fit (purple) and post-fit (red) inclination residuals. As can be seen, the longest periods of the coupling-induced variations in inclination (Figure 5d) are not contained in this 250-day estimation. Rather, the inclination variation is perceived almost in its entirety as a straight line, and the post-fit residuals is just the solution that the least squares estimation finds. However, a frequency decomposition revealed that the components of Δi close to the wobble normal mode in particular is present in both the pre-fit and post-fit residuals at the same level, owing again to the inability of an uncoupled model to emulate the resonance properties of the rotational equations of motion.

Finally, it is practical to see how these results extrapolate to estimations performed over arcs of different lengths. An in-depth analysis of each arc will not be carried out, but rather the extrapolation will be performed only on the basis on the post-fit residual norm history and on the error in estimated initial state. In this regard, Figure 9a shows that, regardless of the arc length, the residual norm increases linearly from the mid-arc point. In this sense, extrapolation becomes straight-forward, and one could easily predict how the residuals of a 300-day arc would behave. On the other hand, Figure 9b shows the evolution of the error in estimated initial state as a function of the length of the estimated arc. There are two things to point out. On the one hand, errors increase monotonically with increasing estimation duration. On the other hand, the hierarchy observed in Equation 18 is maintained for all arc lengths. The error in estimated initial position is dominated by the S component, and the W component shows the smallest error. As for velocity, the importance of the in-plane components is reversed - now the radial component dominates the error - and the out-of-plane component is still the smallest.

This estimation of initial state will be used in following subsections as baseline to assess how different parameters (see subsection 3.4) can absorb the effects of couplings. To this regard, subsection 4.1 showed that the libration amplitude will likely improve the in-plane components of residuals but will not be able to correct the out-of-plane components. Similarly, the zonal and sectorial harmonics of degree 2 represent a gravity field that is symmetric with respect to the equator. In the uncoupled model used as estimation, Phobos' equator is always coincident with its orbital plane, meaning that a gravity field with symmetry about the equator has no ability to induce out-of-plane motion, meaning that out-of-plane components of residuals will also remain when the harmonic coefficients are estimated.

4.2.2. Estimation of additional parameters

As mentioned in subsection 3.4, two more sets of estimations were performed. One of them estimates the initial state together with the once-per-orbit longitudinal libration amplitude; the other estimates the initial state together with the $C_{2,0}$ and $C_{2,2}$ gravity coefficients of Phobos. The results of both estimations were found to be very similar in terms of residuals, so they will be presented together for the sake of brevity. It is however emphasized that the libration amplitude and harmonic coefficients were not estimated simultaneously at any

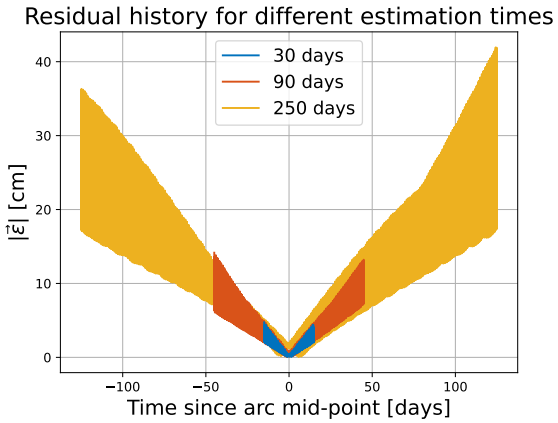

(a) Residual histories for estimations of different lengths.

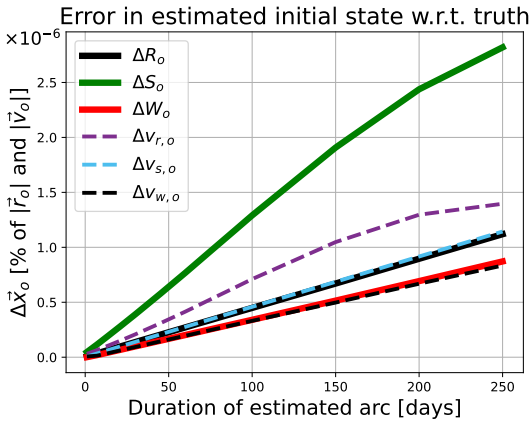

(b) Change in estimated initial state for estimations of different lengths (in days).

Figure 9: Comparison of the results of estimations of different lengths. All of them estimate only initial state. All of them have the same *true* initial state, with $|\vec{r}_o| = 9484$ km and $|\vec{v}_o| = 2113$ m/s.

point, due to ill-posedness of the resulting least squares problem.

Both the once-per-orbit libration amplitude $\mathcal{B}$ and the degree 2 harmonic coefficients $C_{2,x}$ of Phobos are expected to absorb the in-plane effects of couplings, but not the out-of-plane effects (see subsection 4.1). Figure 10a shows the residual history of a 250-day estimation of initial state and libration amplitude. Figure 10b shows the differences between these residuals and the residuals of a 250-day estimation of initial state and gravity coefficients. The R and W components of the two are within 0.5 cm of each other and will be considered equal in the following, while the S component shows a growing difference between the two. This trend is such that along-track residuals are lower in the estimation of gravity field, so that the joint estimation of $C_{2,0}$ and $C_{2,2}$ shows more potential at absorbing couplings than the sole estimation of the libration amplitude. Comparison of Figure 10a with Figure 7b shows that the out-of-plane residuals are indeed not corrected by the estimation of either $\mathcal{B}$ or $C_{2,x}$, while the radial component is completely flattened out (oscillations at millimeter level). The S component, however, shows long-period oscillations at the centimeter level that the estimation of additional parameters cannot account for. This residual reduction has been achieved by adjusting the libration amplitude. Through its relation to Phobos' moments of inertia (Equation 10) and as noted by Ram-

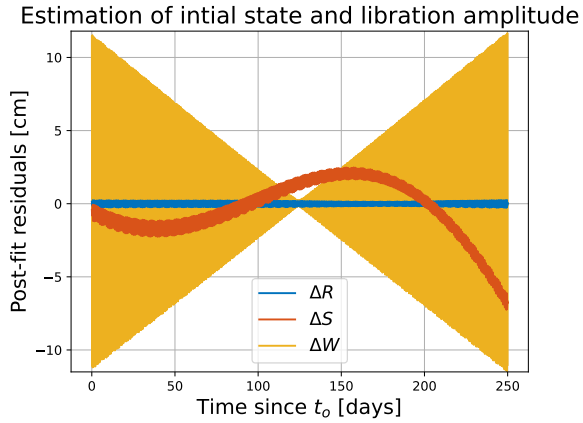

(a) Component-wise post-fit residual history of an estimation of initial state and libration amplitude.

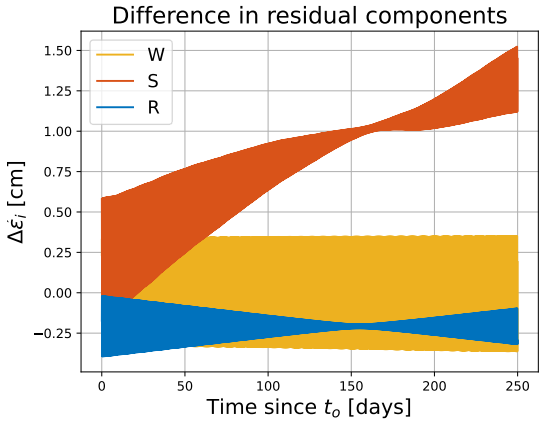

(b) Component-wise differences between the residuals of the two different estimations (gravity coefficients vs libration amplitude).

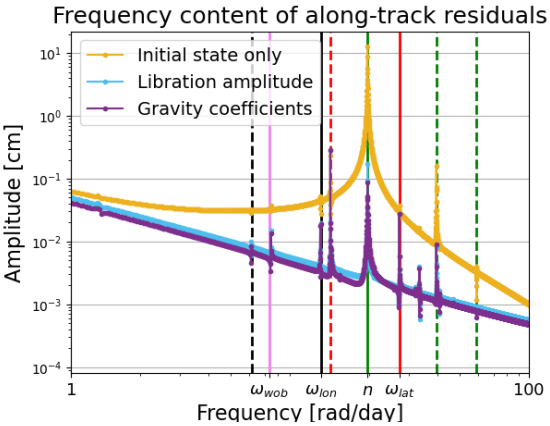

(c) Frequency content of the S components of residuals for all three different estimations: initial state, initial state and libration amplitude, initial state and gravity coefficients. Vertical lines indicate the mean motion (green) and the three normal modes: longitudinal (black), latitudinal (red) and wobble (violet). Dashed lines are multiples/divisors of solid lines.

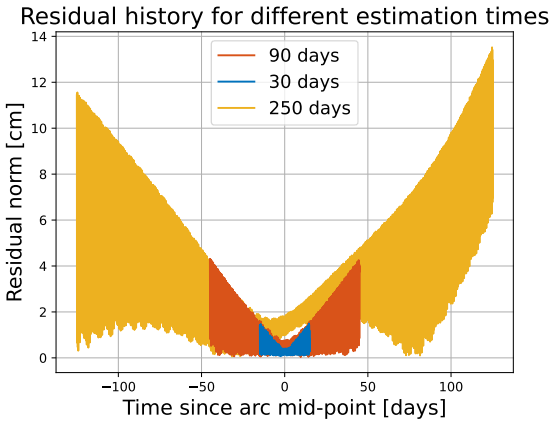

(d) Residual norm history for estimation of different durations (in days) for an estimation of initial state and once-per-orbit longitudinal libration amplitude.

Figure 10: Results in terms of residuals for an estimation of initial state and once-per-orbit libration amplitude and an estimation of initial state and gravity coefficients. The observations are generated with a coupled model and estimation is performed with an uncoupled model.

baux et al. (2012), this quantity is most related to the short-period behaviour of Phobos', with the long periodic dynamics being independent from it. It therefore makes sense that an estimation of libration amplitude cannot correct for this long-periodic behaviour.

Figure 10c shows the residual components at these fast frequencies. There are some that cannot be corrected by adjusting the libration amplitude or harmonic coefficients, namely those that are tightly connected with the resonance phenomenon present in rotational dynamics featured in the coupled model. Particularly the component close to the latitudinal mode ω_{lat} (red solid line) and half of it (red dashed line) in Figure 10c are seen at the same level for the estimation of initial state alone (yellow curve) and for estimations with additional parameters (blue and purple curves). These arise from forcings amplified by the rotational equations of motion contained in the coupled model that the uncoupled model does not have the ability to amplify in the same manner, no matter the changes in libration amplitude or harmonic coefficients.

As was done in subsubsection 4.2.1 with the estimation of initial state, Figure 10d shows how the residuals of the estimation of initial state and libration amplitude behave when arcs of different lengths are considered. Because residuals are now dominated by the out-of-plane component, and this is the same in estimations of initial state alone and estimations of initial state with libration amplitude, the same conclusion is drawn in this case, and one could easily predict the residuals some time beyond the end of the estimated arc by linear extrapolation. However, this assumption of dominance of out-of-plane component could break if longer arcs are estimated and that results in the long-period along-track oscillation seen in Figure 10a growing faster than the out-of-plane oscillations.

Because a good part of the effects of couplings have been absorbed into the new estimated parameters, their estimated values will differ from the *true* ones used to generate the observations. It is of interest to look at how the initial state estimate obtained in subsubsection 4.2.1 changes when additional parameters are estimated with it. Because both the longitudinal libration amplitude and the zonal and sectorial harmonic coefficients of degree 2 can directly produce in-plane motion only, it is expected that the biggest changes occur in the R and S components of the estimated initial state. Equation 19 shows the error in estimated initial position ($\Delta\vec{\rho}_o$) and estimated initial velocity ($\Delta\vec{\eta}_o$) in RSW components for an estimation of initial state and libration amplitude - the result for the estimation of initial state and harmonic coefficients is very much the same. As expected, the

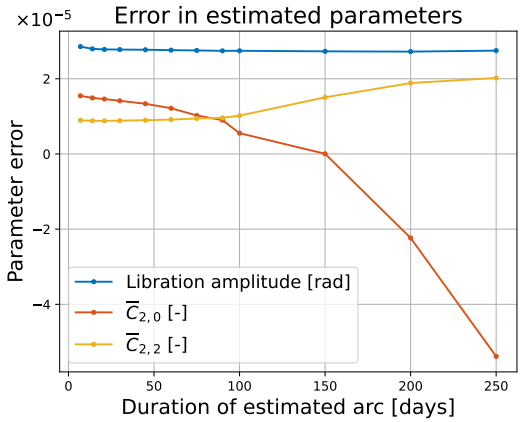

Figure 11: Errors in estimated parameters for estimations performed with arcs of different lengths. Observations are generated with a coupled model and estimation is performed with an uncoupled model. Libration amplitude errors given in terms of the *physical* libration amplitude $\mathcal{A}$ (see subsection 2.2).

W components of both of them remain unchanged from Equation 18. On the other hand, the errors in R and S components have been reduced by 2 orders of magnitude by introducing additional estimated parameters.

$$\Delta\vec{\rho}_o = \begin{bmatrix} -0.11 \\ 0.21 \\ -8.17 \end{bmatrix} \text{ cm} \quad \Delta\vec{\eta}_o = \begin{bmatrix} -0.68 \\ 0.28 \\ -17.73 \end{bmatrix} \times 10^{-6} \text{ m/s} \quad (19)$$

This improvement in estimated initial state is driven by the absorption of couplings into other parameters, namely the libration amplitude and the normalized harmonic coefficients $\overline{C}_{2,0}$ and $\overline{C}_{2,2}$, whose estimates consequently contain errors with respect to their true values. This estimation error has been plotted in Figure 11 for estimations of different durations. For the 250-day estimation, the errors in $\overline{C}_{2,0}$ and $\overline{C}_{2,2}$ is of -5.385×10^{-5} and 2.022×10^{-5} respectively (relative errors of 0.0184% and 0.129%). These errors are one order of magnitude below the uncertainties derived by Jacobson and Lainey (2014) from the moments of inertia provided by Willner et al. (2010). On the other hand, errors in the gravity coefficients grow with estimation duration. For estimations up to 250 days, the error in $\overline{C}_{2,2}$ is more than 3 orders of magnitude above the formal errors reported by Dirkx et al. (2014) for a laser ranging system to a Phobos lander after a year. The error in the once-per-orbit longitudinal libration amplitude seems to quickly stabilize, and acquires a value of 1.575×10^{-3} degrees for the 250-day estimation. This is 4 orders of magnitude below the formal error reported by Lainey et al. (2021), but one order of magnitude above the formal er-

ror predicted by Dirkx et al. (2014) for a laser ranging system to a Phobos lander after 1 year. This shows that couplings are not required for the proper inversion of current data, but will become necessary to process observations from lander missions.

5. Discussion

This section will put the results from this paper in the context of current and future missions and data. It will assess what the impact of these results is on currently available and future information on Phobos' interior.

5.1. Future missions

Phobos' libration amplitude $\mathcal{A}$ and harmonic coefficients $C_{2,0}$ and $C_{2,2}$ have so far been determined from their effect on Phobos' orbit (e.g. Lainey et al. (2007); Jacobson (2010); Jacobson and Lainey (2014)), achieving typical uncertainties of 0.01° for $\mathcal{A}$ (Lainey et al., 2021) and of $10^{-3} - 10^{-4}$ for the gravity coefficients. Alternatively, the libration amplitude has also been determined from bundle block adjustments (Oberst et al., 2014; Burmeister et al., 2018), achieving uncertainties in the same order of magnitudes as those from orbit data. Phobos' trajectory cannot be used to simultaneously estimate all three parameters, and Jacobson and Lainey (2014) reported very high correlations in their estimates of $C_{2,0}$ and $C_{2,2}$. Geophysical knowledge of Phobos is therefore limited by the nature of available observational data.

Coming missions featuring an orbiter and (potentially) a lander will shift this paradigm. Direct-to-Earth tracking of both orbiter and lander will involve models for Phobos' ephemeris, orientation and gravity field, while lander-to-orbiter communications are insensitive to the moon's position. A lander can further decouple Phobos' rotational motion by direct observations of Phobos' orientation using a start-tracker, insensitive to Phobos' ephemeris.

Maistre et al. (2013) studied the inversion of direct-to-Earth Doppler data as well as star tracker measurements to determine the amplitudes of several librations in both longitude and latitude, achieving formal errors in the order of $10^{-3} - 10^{-5}$ degrees for the once-per-orbit longitudinal libration amplitude. On the other hand, the inversion of direct-to-Earth laser ranging data was studied by Dirkx et al. (2014), reporting formal errors in the order of 10^{-5} degrees for the same parameter. Additionally, orbiter tracking can also be used to determine the libration of Phobos, as will be done with the JUICE mission for Ganymede (Cappuccio et al., 2020).

On the one hand, all these formal errors are below the true errors in estimation of libration amplitude reported in the present paper (see subsubsection 4.2.2 and Figure 11) originating from coupling (mis)modelling. This indicates that couplings will necessarily have to be considered in the inversion of data coming from such missions. On the other hand, couplings were shown to produce a drift in the along-track direction (see subsection 4.1 and Figure 5b), which accumulate to several meters over ~50 weeks. The effect of a meter level bias in Phobos' ephemeris on the product of inverting Doppler data from a Phobos lander was investigated by Maistre et al. (2013), and found true errors in estimated libration amplitude in the order of $10^{-2} - 10^{-1}$ degrees, well above all expected formal errors. This is therefore another manner in which couplings will deteriorate the determination of the libration amplitude.

The determination of Phobos' harmonic coefficients $C_{2,0}$ and $C_{2,2}$ will benefit greatly from tracking to a Phobos orbiter. On the one hand, the signature of these two parameters on a spacecraft orbiting Phobos is determined by the position of the spacecraft in the Phobos-fixed frame, most notably by the orbiter's Phobos-fixed longitude λ and latitude ϕ (see Equation 2). Although these two coordinates are sensitive to Phobos' own librations, they are dominated by the orbiter's position in its Phobos-bound orbit. This allows to de-correlate the estimates of libration amplitude from the estimates of harmonic coefficients. Furthermore, the two coefficients $C_{2,0}$ and $C_{2,2}$ have unambiguously different signals in the trajectory of a Phobos orbiter, allowing for further de-correlation of the two. A Phobos lander can also provide estimates of the moon's quadrupole field through its effect on its own ephemeris, although the estimates are expected to be highly correlated. Dirkx et al. (2014) predicts formal errors of $\sim 10^{-4}$ for $C_{2,0}$ and $\sim 10^{-8}$ for $C_{2,2}$ after 1 year of a laser ranging concept to a Phobos lander. Figure 11 shows that, for a 250-day arc, the true errors of both coefficients arising from coupling (mis-)modelling are in the order of 10^{-5}, and the true error for $C_{2,0}$ grows with increasing arc-length. In this light, couplings will need to be considered when modelling Phobos' dynamics in the inversion process of lander laser ranging data.

In their study, Dirkx et al. (2014) use a refined model of Phobos' rotation in combination with an uncoupled translational model, featuring a total of 15 different longitudinal librations, as well as 9 librations of Phobos' right ascension and declination angles. They estimated all amplitudes of the sine and cosine term of each libration, which amounted to a total of 66 estimated parameters to determine the orientation of Phobos. They

reported extremely high correlations among them. The 3D orientation of Phobos can be minimally described using 4 singularity-free parameters: the 3 components of the unitary axis of rotation and the angle of said rotation, namely Phobos' rotation quaternion $\boldsymbol{q}$. Using more parameters simply overdetermines the estimation of Phobos' orientation. Although it has not been done in this paper, the next natural step in this direction is using a coupled dynamical model in estimation, which uses 7 scalar parameters (Phobos' rotation quaternion $\boldsymbol{q}$ and angular velocity vector $\vec{\omega}$) to represent an infinite number of librations about all three axes of Phobos. Note that this would involve a constrained estimation to ensure that $|\boldsymbol{q}| = 1$ at all times.

5.2. Libration mis-modelling

A-priori rotational models are required inputs in bundle block adjustments, the process by which the shape of Phobos - or any other Solar System body - is inferred by concurrent estimation of a series of surface points that are identified in different pictures (Burmeister et al., 2018). Uncoupled models have been shown (subsection 4.1) to most notably mis-represent latitudinal librations and longitudinal librations resonant with Phobos' proper modes (subsection 2.3), the biggest of which the leading latitudinal libration of amplitude 8.5×10^{-3} degrees at 27.14 rad/day (see Table 2). An uncoupled model can introduce displacements in surface points of up to 2 m. These errors arising from dynamical models are below observational quality indicated by e.g. the resolution of 2.6 m/pixel of the Super Resolution Camera of Mars Express (MEX) (Oberst et al., 2014). These librations are therefore not critical in the process of currently available photography.

On the other hand, MMX will carry TENGOO, an optical camera with a 0.9 m m/pixel resolution (Kameda et al., 2021). In this new scenario, latitudinal librations produced by coupled models will be significant in photogrammetry studies using these new images. A possible solution is to include relevant librations at the appropriate frequencies and estimate their amplitudes in the same way the once-per-orbit longitudinal libration amplitude is estimated in current bundle block adjustments. This, however, presents the complication of identifying what frequencies are relevant in the frequency spectrum, in particular when they are associated to resonances with normal modes.

Expressions for the normal modes exist (Equation 12) that use information on the principal moments of inertia. They could in principle be used to locate librational frequencies of interest and include them in kinematical rotational models to estimate their amplitudes. This was attempted by i.e. Dirkx et al. (2014), who estimated the amplitudes and phases of 15 different longitudinal librations and 9 librations of Phobos' right ascension and declination angles, amounting to a total of 66 estimated parameters. They reported very high correlations among them - in the order of 0.99. In their work, Dirkx et al. (2014) considered librations at the frequencies reported by Rambaux et al. (2012)[2]. These frequencies are a result of the moments of inertia that Rambaux et al. (2012) use in their simulations (namely the one developed by Willner et al. (2010)). The validity of such an approach is however limited by the fact that not much is known about Phobos' interior in the first place, and librational estimates are a means to obtain this information - rather than the other way around.

The advantage that coupled models bring in this respect lies in the fact that 7 scalar parameters - the size of the rotational state vector (see subsection 2.1) - can represent an infinite amount of librations in all three axes. Least squares estimations will however need to implement constraints, namely that the obtained rotation quaternion is unitary ($|\boldsymbol{q}| = 1$).

5.3. Phobos' interior composition

Equation 20 (Dirkx et al., 2019) provides Phobos' moments of inertia as functions of the (unnormalized) gravity coefficients $C_{2,0}$ and $C_{2,2}$ as well as the scaled mean moment of inertia $\tilde{I} = I/MR^2$, where M and R are Phobos' mass and reference radius. Note that Equation 20d relates $\tilde{I}$ with the once-per-orbit longitudinal libration amplitude $\mathcal{A}$. With the errors in estimated harmonic coefficients and libration amplitude from Figure 11, the inertia moments can be mis-calculated by $3 - 5 \times 10^{-4}$ (0.2 – 0.3%).

$$\frac{I_{xx}}{MR^2} = \frac{1}{3}C_{2,0} - 2C_{2,2} + \tilde{I} \tag{20a}$$

$$\frac{I_{yy}}{MR^2} = \frac{1}{3}C_{2,0} + 2C_{2,2} + \tilde{I} \tag{20b}$$

$$\frac{I_{zz}}{MR^2} = -\frac{2}{3}C_{2,0} + \tilde{I} \tag{20c}$$

$$\tilde{I} = \frac{2}{3}C_{2,0} + 12C_{2,2}\left(1 - \frac{2e}{\mathcal{A}}\right) \tag{20d}$$

Maistre et al. (2019) provides the values of the libration amplitude, harmonic coefficients and moments of

[2] Dirkx et al. (2014) mention that their method is able to determine the amplitudes to a precision smaller than the cut-off applied by Rambaux et al. (2012) to their reported spectrum. In the context of the potential of their work, the rotational model used by Dirkx et al. (2014) is therefore effectively incomplete.

inertia for different interior structures of Phobos - rubble pile, layered, ... The moments of inertia of different structures differ by ∼15%, while models are largely indistinguishable among them in terms of libration amplitude and degree 2 gravity coefficients, with the exception of the highly fractured and the disrupted-and-reaccreted bodies (both necessitating a monolithic Phobos at least at some point in time). In the light of the results of this paper, couplings will not induce a sufficient shift in estimated observables to discriminate between categories, or to draw erroneous conclusions to this respect. It is likely to allow, however, for the fine determination of e.g. the percentage of porosity of a rubble pile Phobos.

Coupled models offer a different estimation approach. The libration amplitude itself cannot be estimated with a coupled model, but the mean moment of inertia $\tilde{I}$ can, providing a direct determination of Phobos' radial mass distribution.

6. Conclusions

This paper has investigated how couplings between Phobos' translational and rotational dynamics affect the propagation of a given initial state, as well as how using an uncoupled model in data inversion impacts the results thereof. The solution of propagating an initial state with coupled and uncoupled dynamics were directly compared between them, and the latter model was used to estimate different parameters from observations generated by the former.

On the one hand, it was confirmed that couplings have a qualitatively similar effect to the once-per-orbit longitudinal libration when it comes to motion inside the orbital plane. Differences between the coupled and uncoupled trajectories were largest in the along track direction, with the uncoupled solution getting ahead of the coupled one as much as 40 m after 9 years and 4 months. A secular component was however not present in the differences in the radial and out-of-plane directions, which just oscillated with a growing amplitude that reached 4 m.

State-of-the-art uncoupled models are by definition not designed to emulate the latitudinal librations present in Phobos' motion. Misrepresentations in longitudinal librations stem from the inability of uncoupled models to introduce resonance-amplified librations, particularly of forcings close to the longitudinal normal mode. The largest longitudinal and latitudinal librations that uncoupled models cannot account for stand at amplitudes of 3.6×10^{-3} and 8.5×10^{-3} degrees respectively - displacements at Phobos' surface of 0.8 and 1.9 meters respectively. Furthermore, latitudinal librations couple with Phobos' orbit to produce an ever-growing oscillation of Phobos' inclination with a period of about 2 years, which in turn induces long-term librations that are not accounted for by uncoupled models.

Mismodelling of couplings in estimation results in true errors of estimated parameters, which should ideally stay below formal errors. True errors in the amplitude of the once-per-orbit physical longitudinal libration $\mathcal{A}$ and Phobos' normalized coefficients $\overline{C}_{2,0}$ and $\overline{C}_{2,2}$ were found to be of about 1.6×10^{-3} degrees, 5.4×10^{-5} and 2.0×10^{-5} respectively after 250 days. The error in libration amplitude was seen to quickly stabilize at that value when different estimation times were tested, while error in harmonic coefficients are expected to grow for longer estimations. All these true errors are well within error bars of current inversion products, but are 1 to 3 orders of magnitude above the expected formal errors computed by Dirkx et al. (2014) for a lander ranging concept. Thus, a proper inversion of this data will not be possible with the use of uncoupled models. This type of observations represent the limiting factor in a likely Phobos-bound mission that provides lander and orbiter range measurements. This data will be most fruitfully processed together as a single observation set. For this, the use of coupled models in estimation will be required.

On the other hand, estimation post-fit residuals were seen to occur mostly in the out-of-plane direction, in which the once-per-orbit longitudinal libration and Phobos' zonal and sectorial gravity coefficients of degree 2 have little to no effect. They showed the largest values at 10 cm at the two ends of the 250-day arc. However, the along-track residuals showed a long-periodic oscillation that could potentially outgrow the out-of-plane components for longer estimations. Further study is required in this direction.

Appendix A. Complete simulation definition

Appendix A.1. Third body forces

The time-evolution of Phobos' translational and rotational states $\vec{x}_t = [\vec{r},\ \vec{v}]$ and $\vec{x}_r = [\boldsymbol{q},\ \vec{\omega}]$ is given, in its general form, as in Equation 4, where $\vec{a}$ and $\vec{T}$ are the total acceleration and torque on Phobos respectively, while $\boldsymbol{I}$ is Phobos' inertia tensor and q_i is the i-th component of the rotation quaternion $\boldsymbol{q}$. The mutual acceleration between Mars and Phobos is given as in Equation 3, where both Mars and Phobos are treated as extended, aspherical bodies. Due to the large distances of the Solar System, the interactions between Phobos and other bodies - namely Deimos, the Sun, the Earth and

Jupiter - have been modelled as interactions between two point masses. The acceleration that a body i creates on Phobos, expressed in the Mars-centered frame (see subsection 2.1) is provided in Equation A.1, where i and P stand for body i and Phobos, $\vec{r}_{iP}$ and $\vec{r}_{iM}$ are vectors going from body i to Phobos and Mars respectively, and r_{iP} and r_{iM} are their respective norms.

$$\vec{a} = -\mu_i \left(\frac{\vec{r}_{iP}}{r_{iP}^3} - \frac{\vec{r}_{iM}}{r_{iM}^3} \right) \tag{A.1}$$

In the evaluation of all the terms in the equations of motion, the positions of all bodies is required, as well as their gravitational parameters and, in some cases, their harmonic coefficients as well. The rest of this section will specify the sources of all this data used in this work.

Appendix A.2. Mars

- Gravity field: MRO120D developed by Konopliv et al. (2016). Mars' reference radius (R in Equation 2b) is 3396.0km and the Martian gravitational parameter is $\mu_M = 42828.3750104$ km^3/s^2. All sine and cosine coefficients up to degree and order 12 have been included.

- Rotation model: The rotation model developed by Konopliv et al. (2016), used also by Lainey et al. (2021).

Appendix A.3. Phobos

- Gravity field: Spherical harmonics collected in Table A.4, taken from the homogeneous model of Phobos by Maistre et al. (2019). The reference radius is 14km and the mass is 1.06×10^{16}kg. A value of $G = 6.67259 \times 10^{-11}$ was used, resulting in $\mu_P = 707294.54$m^3/s^2. Coefficients presented in Table A.4 are normalized as shown in Equation A.3.

- Rotation model: See subsection 2.5.

- Inertia tensor: Computed with the gravity coefficients as per Equation A.2 (Maistre et al., 2019), where $\tilde{I}$ is the mean moment of inertia. These moments are normalized with MR^2. In this work, the value of $\tilde{I}$ was selected to be consistent with the homogeneous model of Phobos. The full tensor for a gravity field containing all coefficients up to degree and order 2 is provided in Eq.(23) by Maistre et al. (2019), from which a normalized mean moment of inertia of $\tilde{I} = 0.2645233$ can be inferred.

Table A.4: Normalized harmonic cosine $\left(\overline{C}_{l,m}\right)$ and sine $\left(\overline{S}_{l,m}\right)$ coefficients of degree l and order m. Normalization performed as shown in Equation A.3.

l	m	$\overline{C}_{l,m}$	$\overline{S}_{l,m}$
0	0	1.0	—
1	0	0.0	—
	1	0.0	0.0
2	0	-0.029243	—
	1	0.000084	0.000072
	2	0.015664	-0.000020
3	0	-0.002222	—
	1	-0.002450	0.001399
	2	0.004268	-0.000537
	3	0.000917	-0.006642
4	0	0.002693	—
	1	-0.001469	0.000402
	2	-0.000920	-0.000555
	3	0.001263	-0.001218
	4	-0.000032	0.000088

$$\begin{aligned} I_{xx} &= \frac{1}{3} C_{2,0} - 2C_{2,2} + \tilde{I} \\ I_{yy} &= \frac{1}{3} C_{2,0} + 2C_{2,2} + \tilde{I} \\ I_{zz} &= -\frac{2}{3} C_{2,0} + \tilde{I} \\ I_{xy} &= -2S_{2,2} \\ I_{xz} &= -C_{2,1} \\ I_{yz} &= -S_{2,1} \end{aligned} \tag{A.2}$$

Appendix A.4. Third bodies

- Sun and Earth: The masses of these bodies are taken from the INPOP19a (Fienga et al., 2019) ephemerides product. Their locations are computed with a combination of the NOE-4-2020 ephemerides (Lainey et al., 2021) within the Martian system.

- Deimos: The mass and position of Deimos are computed with the NOE-4-2020 ephemerides (Lainey et al., 2021).

- Jupiter: Use is made of the NOE-5-2021 ephemerides (Fayolle et al., 2023) to compute Jupiter's mass and position with respect to the Jovian system's barycenter. The INPOP19a (Fienga et al., 2019) ephemerides and NOE-4-2020 (Lainey et al., 2021) are then use to compute its position with respect to Mars and Phobos.

$$\begin{bmatrix}\overline{C}_{l,m}\\ \overline{S}_{l,m}\end{bmatrix} = \sqrt{\frac{(l+m)!}{(2-\delta_{0,m})(2l+1)(l-m)!}}\begin{bmatrix}C_{l,m}\\ S_{l,m}\end{bmatrix} \tag{A.3}$$

Appendix A.5. Numerical integration

All these equations and terms have been numerically propagated using *Tudat* (*TU Delft Astrodynamics Toolbox*), which offers a wide range of possible integrators, propagators and environments. In this work, all simulations have been performed using the Cowell propagator formulated in Equation 4 in combination with an RKF8(10) integrator working in a fixed-step regime of 5 minutes. For reproducibility purposes, Equation A.4 provides the translational and rotational initial states returned by the damping algorithm discussed in subsection 2.3 and described in Appendix C. The translational state has been used for both the coupled and uncoupled models in propagation.

$$\vec{x}_{t,o} = \begin{bmatrix}-1991723.0176246795\\ -8742964.680527888\\ -3180540.016758049\\ 1843.0987517454296\\ -43.60246872601227\\ -1018.5417927808861\end{bmatrix} \tag{A.4a}$$

$$\vec{x}_{r,o} = \begin{bmatrix}0.7117384685576372\\ 0.3074341368827725\\ 0.0347308749007907\\ 0.6306396516101695\\ 6.2438591968356885\times10^{-9}\\ -1.3079675754811962\times10^{-7}\\ 2.323693355272973\times10^{-4}\end{bmatrix} \tag{A.4b}$$

Appendix B. Libration definitions

This section will collect different possible combinations for the definition of the libration angles to serve as reference when comparing this work with others, as well as other works among them.

The different combinations will be defined with respect to the definition used in this work, which is depicted in Figure 1. As a reminder, the tidal libration is denoted as ψ, the physical libration is denoted as γ, the true and mean anomalies will be denoted θ and M respectively, and $\mathcal{A}$ and e are the amplitude of the once-per-orbit physical longitudinal libration and the eccentricity of the orbit respectively. It is emphasized that the definition used in this work, is mathematically represented by Equation B.1a and Equation B.1c. The alternative definition of $\mathcal{A}$ in Equation B.1b could also be used in combination with Equation B.1a. From Equation B.1b and Equation B.1c, two alternative definitions for $\mathcal{B}$ can be inferred. It is also emphasized that the one used in this work is $\mathcal{A} = (2-\mathcal{B})e$, inferred from Equation B.1c in combination with $\psi = -\mathcal{B}e\sin M$.

$$\gamma - \psi = \theta - M = 2e\sin M \tag{B.1a}$$

$$\gamma = -\mathcal{A}\sin M\ ,\ \mathcal{A}>0\ ;\ \psi = -(\mathcal{A}+2e)\sin M \tag{B.1b}$$

$$\gamma = \mathcal{A}\sin M\ ,\ \mathcal{A}<0\ ;\ \psi = -(2e-\mathcal{A})\sin M \tag{B.1c}$$

About the definition used in this work, it is noted that the tidal libration angle ψ is the *opposite* of Mars' longitude in Phobos' sky (see Equation 6). That is why an alternative definition of the libration angles has ψ defined in the opposite direction as this work. In this case, Equation B.2a applies. The two possible definitions of $\mathcal{A}$ that can be used in combination with this equations are collected in Equation B.2b and Equation B.2c

$$\gamma + \psi = \theta - M = 2e\sin M \tag{B.2a}$$

$$\gamma = -\mathcal{A}\sin M\ ,\ \mathcal{A}>0\ ;\ \psi = (2e+\mathcal{A})\sin M \tag{B.2b}$$

$$\gamma = \mathcal{A}\sin M\ ,\ \mathcal{A}<0\ ;\ \psi = (2e-\mathcal{A})\sin M \tag{B.2c}$$

The definitions in Equation B.1 and Equation B.2 require the introduction of a negative sign in Equation 8a in order to keep $\mathcal{A}>0$. Thus, another sensible and useful definition of γ has the angle defined in the opposite way of this work, in combination with the same definition of ψ. These definition of the angles is represented by Equation B.3.

$$\gamma + \psi = M - \theta = -2e\sin M \tag{B.3a}$$

$$\gamma = \mathcal{A}\sin M\ ,\ \mathcal{A}>0\ ;\ \psi = -(\mathcal{A}+2e)\sin M \tag{B.3b}$$

$$\gamma = -\mathcal{A}\sin M\ ,\ \mathcal{A}<0\ ;\ \psi = (\mathcal{A}-2e)\sin M \tag{B.3c}$$

Finally, one could define not one, but both ψ and γ opposite to those in this work. Then, Equation B.4 should be used.

$$\gamma - \psi = M - \theta = -2e\sin M \tag{B.4a}$$

$$\gamma = \mathcal{A}\sin M\ ,\ \mathcal{A}>0\ ;\ \psi = (2e+\mathcal{A})\sin M \tag{B.4b}$$

$$\gamma = -\mathcal{A}\sin M\ ,\ \mathcal{A}<0\ ;\ \psi = (2e-\mathcal{A})\sin M \tag{B.4c}$$

It is emphasized that, if used appropriately, all these different equations are actually equivalent, even though different authors may choose different definitions and combinations. What is key is the correct use of this angles in the equations of motion. However, any of these definitions could be used in analytical discussions and to present results. Note that the relationship between

the physical and tidal librations is only required when both are actually used in the discussion. This is rarely the case, and works often manage only physical librations.

A few examples that do discuss and differences between tidal and physical librations are Jacobson (2010) and Lainey et al. (2021). For instance, Eq.(2) by Jacobson (2010) is clearly equivalent to Equation B.4a, while Eqs.(3-4) of the same source are identical to Equation B.4b. It is then inferred that they defined both angles in the opposite way as this work while keeping $\mathcal{A} > 0$. On the other hand, Lainey et al. (2019) and Lainey et al. (2021) state that their $\mathcal{A}$ is the opposite as that of Jacobson (2010). At the same time, the combination of Eq.(8) and Eq.(22) by Lainey et al. (2019) is identical to Equation B.1c. Although no such information is stated by Lainey et al. (2021), it can be assumed that the same convention is used. This is to say that their libration angles are defined in the same way as in this paper together with the same sign of $\mathcal{A}$. As a matter of fact, the software employed in this work implements the libration angles as used by Lainey et al. (2021), and the conventions in this work have been chosen to follow suit.

Appendix C. Damping algorithm

The damping algorithm used in this work is that used by Rambaux et al. (2012). This algorithm is heavily particularized for obtaining an initial state of bodies that are locked in spin-orbit resonance and present a constant (averaged) rotation around their z axis. Such a constant rotation rate will follow the evolution of their orbital mean motion, and will be denoted here as ω_o. The algorithm is designed to damp the normal modes around all axes, while preserving this constant rotation.

For this, a *virtual* torque is added to the dynamics of the moon, which is known to oppose its rotation. This virtual torque $\vec{\Gamma}_d$ is computed as in Equation C.1.

$$\vec{\Gamma}_d = -\frac{1}{\tau_d} \boldsymbol{I} \left(\vec{\omega} - \vec{\omega}_o\right) \tag{C.1}$$

In this equation, τ_d is a given dissipation time that is provided by the user, $\vec{\omega} = [\omega_x\ ,\ \omega_y\ ,\ \omega_z]$ is the rotational velocity of the moon (expressed in body axes) and $\vec{\omega}_o = [0\ ,\ 0\ ,\ \omega_o]$ is the constant angular velocity of a moon in pure synchronous rotation.

In order to obtain the *damped* dynamics of the moon, the algorithm propagates the dynamics with the torque forward in time for a time of $10\tau_d$. The final state is used to start a propagation *backwards* in time and *without* the virtual torque. The result of this forward-backward propagation is a *damped initial state* at $t = 0$ that, if propagated forward in time *without* the virtual torque, the dynamics will not contain the normal modes.

Or at least, not in such a strong way as before the two propagations. The damping provided by the virtual torque is not perfect, so the process is repeated several times with ever-increasing dissipation times. Each iteration, the *damped initial state* from the previous iteration is used to propagate the dynamics forward with the damping torque. This way, the initial state is damped even further in each iteration.

The process and result of this damping algorithm is portrayed in Figure C.12. In this work, an initial value of $\tau_d = 4$h has been used, and each iteration of the damping algorithm doubles this damping time, up to a final damping time of $\tau_d = 8192$h. Note that a value of $\tau_d = \infty$ means there is no damping at all. In Figure C.12a, the Phobos-fixed angular coordinates of Mars are plotted in a longitude-latitude map, where the (0,0) coordinate is identified with the moon-to-planet line. Here the overall effect of the full damping algorithm is very well represented. Pre-algorithm dynamics feature Phobos' x-axis deviating from the moon-to-planet line about 4.5º in longitude and 0.03º in latitude, product of a mixture of normal modes together with resonant forcings. The damping algorithm removes all oscillations occurring at the frequencies of the normal modes while leaving all librations due to forcings behind, as well as the once-per-orbit longitudinal libration.

The difference in the frequency spectrum of the damped and undamped librational motion of Phobos is presented in Figure C.12b and Figure C.12c respectively. It is worth noting how the oscillations close to the longitudinal normal mode in Figure C.12b (black, dashed, vertical line) are decrease from $\sim$1 to $\sim 10^{-4}$ degrees. It is also worth noting how this is not the case for the latitudinal libration close to the latitudinal normal mode, which seems to not be damped at all. The progressive damping of these librations, however, can be seen in Figure C.12d. This picture makes it apparent that there were three peaks very close to the latitudinal normal mode, and only one was actually a forced libration (the middle one), whose amplitude remains the same over the whole damping process, while the other two peaks where excitations of the normal mode that had been damped by 1 to 2 orders of magnitude after the final iteration of the algorithm.

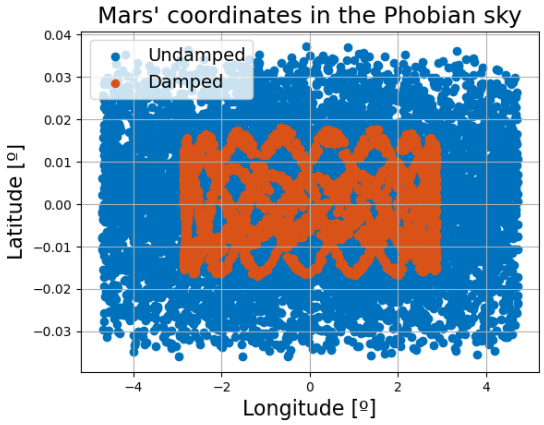

(a) Comparison between damped and undamped tidal librations.

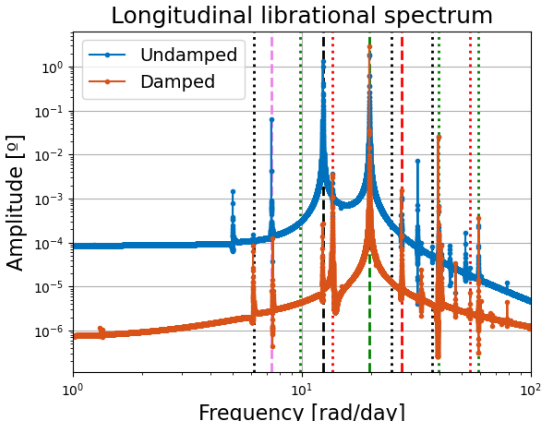

(b) Frequency content of Phobos-fixed longitude of Mars for both the damped and undamped dynamics.

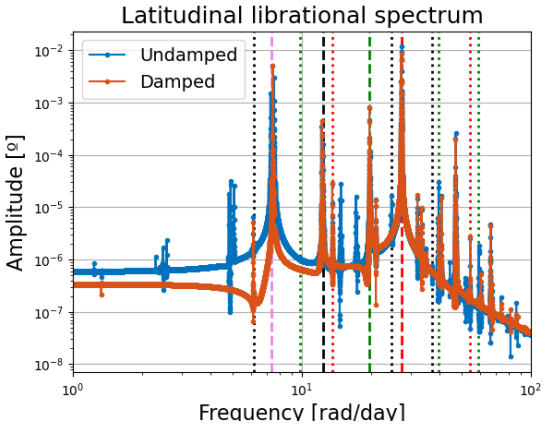

(c) Frequency content of Phobos-fixed latitude of Mars for both the damped and undamped dynamics.

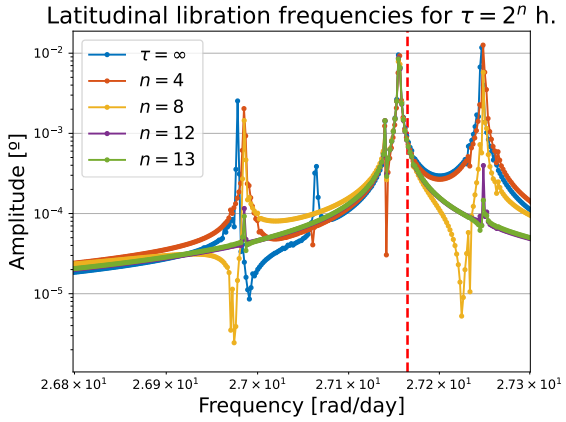

(d) Damping process of the latitudinal librations close to the latitudinal normal mode.

Figure C.12: The damping algorithm, explained in figures. Dashed vertical lines indicate the mean motion (green) and all three normal modes: longitudinal (black), latitudinal (red) and wobble (violet).

References

Akim, E., Stepanyants, V., Tuchin, A., Shishov, V., 2007. Motion parameters determination of the sc and phobos in the project phobos-grunt, in: Proceedings of the 20th International Symposium on Space Flight Dynamics, pp. 1–15.

Archinal, B.A., Acton, C.H., A'Hearn, M.F., Conrad, A., Consolmagno, G.J., Duxbury, T., Hestroffer, D., Hilton, J.L., Kirk, R.L., Klioner, S.A., McCarthy, D., Meech, K., Oberst, J., Ping, J., Seidelmann, P.K., Tholen, D.J., Thomas, P.C., Williams, I.P., 2018. Report of the IAU working group on cartographic coordinates and rotational elements: 2015. Celestial Mechanics and Dynamical Astronomy 130. doi:10.1007/s10569-017-9805-5.

Battin, R.H., 1999. An introduction to the mathematics and methods of astrodynamics. American Institute of Aeronautics and Astronautics.

Borderies, N., 1977. Mutual gravitational potential of n solid bodies. Celestial Mechanics 18, 295–307.

Borderies, N., Yoder, C., 1990. Phobos' gravity field and its influence on its orbit and physical librations. Astronomy & Astrophysics 233, 235–251.

Burmeister, S., Willner, K., Schmidt, V., Oberst, J., 2018. Determination of phobos' rotational parameters by an inertial frame bundle block adjustment. Journal of Geodesy 92, 963–973. doi:10.1007/s00190-018-1112-8.

Cappuccio, P., Hickey, A., Durante, D., Di Benedetto, M., Iess, L., De Marchi, F., Plainaki, C., Milillo, A., Mura, A., 2020. Ganymede's gravity, tides and rotational state from juice's 3gm experiment simulation. Planetary and Space Science 187, 104902. URL: https://www.sciencedirect.com/science/article/pii/S003206331930385X, doi:https://doi.org/10.1016/j.pss.2020.104902.

Chapront-Touze, M., 1988. Esapho - a semi-analytical theory for the orbital motion of phobos. AAP 200, 255–268. URL: https://ui.adsabs.harvard.edu/abs/1988A&A...200..255C.

Dirkx, D., Mooij, E., Root, B., 2019. Propagation and estimation of the dynamical behaviour of gravitationally interacting rigid bodies. Astrophysics and Space Science 364. doi:10.1007/s10509-019-3521-4.

Dirkx, D., Vermeersen, L., Noomen, R., Visser, P., 2014. Phobos laser ranging: Numerical geodesy experiments for martian system science. Planetary and Space Science 99, 84–102. doi:10.1016/j.pss.2014.03.022.

Duxbury, T.C., 1974. Phobos: Control network analysis. Icarus 23, 290–299. doi:10.1016/0019-1035(74)90007-4.

Duxbury, T.C., Callahan, J.D., 1981. Pole and prime meridian expressions for PHOBOS and deimos. The Astronomical Journal 86, 1722. doi:10.1086/113056.

Duxbury, T.C., Callahan, J.D., 1989. Phobos and deimos control networks. Icarus 77, 275–286. doi:10.1016/0019-1035(89)90090-0.

Fayolle, M., Magnanini, A., Lainey, V., Dirkx, D., Zannoni, M., Tortora, P., 2023. Combining astrometry and juice–europa clipper radio science to improve the ephemerides of the galilean moons. arXiv preprint arXiv:2307.15966 doi:10.48550/arXiv.2307.15966.

Fienga, A., Avdellidou, C., Hanuš, J., 2019. Asteroid masses obtained with INPOP planetary ephemerides. Monthly Notices of the Royal Astronomical Society 492, 589–602. doi:10.1093/mnras/stz3407.

Fukushima, T., 2012. SIMPLE, REGULAR, AND EFFICIENT NUMERICAL INTEGRATION OF ROTATIONAL MOTION. The Astronomical Journal 135, 2298–2322. doi:10.1088/0004-6256/135/6/2298.

Goldman, R., 2011. Understanding quaternions. Graphical Models 73, 21–49. URL: https://www.sciencedirect.com/science/article/pii/S1524070310000172, doi:https://doi.org/10.1016/j.gmod.2010.10.004.

Hall, A., 1878. Discovery of satellites of mars. Monthly Notices of the Royal Astronomical Society 38, 205–209. URL: https://ui.adsabs.harvard.edu/abs/1878MNRAS..38..205H/abstract.

Jacobson, R., Konopliv, A., Park, R., Folkner, W., 2018. The rotational elements of mars and its satellites. Planetary and Space Science 152, 107–115. doi:10.1016/j.pss.2017.12.020.

Jacobson, R., Lainey, V., 2014. Martian satellite orbits and ephemerides. Planetary and Space Science 102, 35–44. doi:10.1016/j.pss.2013.06.003.

Jacobson, R.A., 2010. The orbits and masses of the martian satellites and the libration of phobos. The Astronomical Journal 139, 668–679. doi:10.1088/0004-6256/139/2/668.

Kameda, S., Ozaki, M., Enya, K., Fuse, R., Kouyama, T., Sakatani, N., Suzuki, H., Osada, N., Kato, H., Miyamoto, H., Yamazaki, A., Nakamura, T., Okamoto, T., Ishimaru, T., Hong, P., Ishibashi, K., Takashima, T., Ishigami, R., Kuo, C.L., Abe, S., Goda, Y., Murao, H., Fujishima, S., Aoyama, T., Hagiwara, K., Mizumoto, S., Tanaka, N., Murakami, K., Matsumoto, M., Tanaka, K., Sakuta, H., 2021. Design of telescopic nadir imager for geomorphology (TENGOO) and observation of surface reflectance by optical chromatic imager (OROCHI) for the martian moons exploration (MMX). Earth, Planets and Space 73. URL: https://doi.org/10.1186/s40623-021-01462-9, doi:10.1186/s40623-021-01462-9.

Keeler, J.E., 1888. Micrometer observations of the satellites of mars. The Astronomical Journal 8, 73–78.

Konopliv, A.S., Park, R.S., Folkner, W.M., 2016. An improved JPL mars gravity field and orientation from mars orbiter and lander tracking data. Icarus 274, 253–260. doi:10.1016/j.icarus.2016.02.052.

Lainey, V., Dehant, V., Pätzold, M., 2007. First numerical ephemerides of the martian moons. Astronomy & Astrophysics 465, 1075–1084. doi:10.1051/0004-6361:20065466.

Lainey, V., Noyelles, B., Cooper, N., Rambaux, N., Murray, C., Park, R., 2019. Interior properties of the inner saturnian moons from space astrometry data. Icarus 326, 48–62. doi:10.1016/j.icarus.2019.01.026.

Lainey, V., Pasewaldt, A., Robert, V., Rosenblatt, P., Jaumann, R., Oberst, J., Roatsch, T., Willner, K., Ziese, R., Thuillot, W., 2021. Mars moon ephemerides after 14 years of mars express data. Astronomy & Astrophysics 650, A64. doi:10.1051/0004-6361/202039406.

Maistre, S.L., Rivoldini, A., Rosenblatt, P., 2019. Signature of phobos' interior structure in its gravity field and libration. Icarus 321, 272–290. doi:10.1016/j.icarus.2018.11.022.

Maistre, S.L., Rosenblatt, P., Rambaux, N., Castillo-Rogez, J.C., Dehant, V., Marty, J.C., 2013. Phobos interior from librations determination using doppler and star tracker measurements. Planetary and Space Science 85, 106–122. doi:10.1016/j.pss.2013.06.015.

Marth, A., 1879. On the satellites of mars. Astronomische Nachrichten 95, 369–379.

Miranda, C., Patel, M., Berberan-Santos, M.N., Hormigo, T., Correia, A., Pedras, B., Martins, Z., 2023. The importance of phobos simulants: a review on our current knowledge. Frontiers in Astronomy and Space Sciences 10.

Murray, C.D., Dermott, S.F., 1999. Solar system dynamics. Cambridge university press.

Nadezhdina, I.E., Zubarev, A.E., 2014. Formation of a reference coordinate network as a basis for studying the physical parameters of phobos. Solar System Research 48, 269–278. doi:10.1134/s003809461404008x.

Nakamura, T., Ikeda, H., Kouyama, T., Nakagawa, H., Kusano, H., Senshu, H., Kameda, S., Matsumoto, K., Gonzalez-Franquesa, F., Ozaki, N., Takeo, Y., Baresi, N., Oki, Y., Lawrence, D.J., Chabot, N.L., Peplowski, P.N., Barucci, M.A., Sawyer, E., Yokota, S., Terada, N., Ulamec, S., Michel, P., Kobayashi, M., Sasaki, S., Hirata, N., Wada, K., Miyamoto, H., Imamura, T., Ogawa, N., Ogawa, K., Iwata, T., Imada, T., Otake, H., Canalias, E., Lorda, L., Tardivel, S., Mary, S., Kunugi, M., Mitsuhashi, S., Doressoundiram, A., Merlin, F., Fornasier, S., Reess, J.M., Bernardi, P., Imai, S., Ito, Y., Ishida, H., Kuramoto, K., Kawakatsu, Y., 2021. Science operation plan of phobos and deimos from the MMX spacecraft. Earth, Planets and Space 73. doi:10.1186/s40623-021-01546-6.

Newall, H.F., 1895. Micrometer measurements of phobos, the inner satellite of mars, during the opposition of 1894. Monthly Notices of the Royal Astronomical Society 55, 348–353. doi:10.1093/mnras/55.7.348.

Oberst, J., Zubarev, A., Nadezhdina, I., Shishkina, L., Rambaux, N., 2014. The phobos geodetic control point network and rotation model. Planetary and Space Science 102, 45–50. doi:10.1016/j.pss.2014.03.006.

Pickering, E.C., Searle, A., Upton, W., 1879. Photometric observations. part ii. appendix f. satellites of mars 1879. Annals of Harvard College Observatory 11, 311–317. URL: https://ui.adsabs.harvard.edu/abs/1879AnHar..11..311P.

Rambaux, N., Castillo-Rogez, J.C., Maistre, S.L., Rosenblatt, P., 2012. Rotational motion of phobos. Astronomy & Astrophysics 548, A14. doi:10.1051/0004-6361/201219710.

Rambaux, N., Castillo-Rogez, J.C., Williams, J.G., Özgür Karatekin, 2010. Librational response of enceladus. Geophysical Research Letters 37. doi:10.1029/2009gl041465.

Shishov, V.A., 2008. Determination of spacecraft and phobos parameters of motion in the phobos-grunt project. Solar System Research 42, 319–328. doi:10.1134/s0038094608040047.

Smith, B.A., 1970. Phobos: Preliminary results from mariner 7. Science 168, 828–830. doi:10.1126/science.168.3933.828.

Stark, A., Willner, K., Burmeister, S., Oberst, J., 2017. Geodetic framework for martian satellite exploration i: Reference rotation models, in: European Planetary Science Congess 2017, pp. 1–2.

Tolson, R.H., Blackshear, W.T., Mason, M.L., Kelly, G.M., 1977. The mass of phobos. Geophysical Research Letters 4, 551–554. doi:10.1029/gl004i012p00551.

Veverka, J., 1978. The surfaces of phobos and deimos. Vistas in Astronomy 22, 163–192. doi:10.1016/0083-6656(78)90014-4.

Willner, K., Oberst, J., Hussmann, H., Giese, B., Hoffmann, H., Matz, K.D., Roatsch, T., Duxbury, T., 2010. Phobos control point network, rotation, and shape. Earth and Planetary Science Letters 294, 541–546. doi:10.1016/j.epsl.2009.07.033.

Woolard, E.W., 1944. The secular perturbations of the satellites of mars. The Astronomical Journal 51, 33. URL: https://ui.adsabs.harvard.edu/abs/1944AJ.....51...33W, doi:10.1086/105793.

Yang, Y., Yan, J., Guo, X., He, Q., Barriot, J.P., 2020. An elastic model of phobos' libration. Astronomy & Astrophysics 636, A27. doi:10.1051/0004-6361/202037446.

3

Conclusions and recommendations

This section will synthesize the outcome of the research paper included in chapter 2 in the form of answers to the research (sub)questions formulated in section 1.1.

3.1. Conclusions

This section will collect the answers to the research (sub)questions from section 1.1. The subquestions will be answered first, which will serve to shape an answer to the main research question.

- **How does the trajectory of Phobos change when an initial state is integrated with an uncoupled model as opposed to a coupled model?**

  In studying the position differences between the coupled and uncoupled trajectories, it was found that the uncoupled trajectory got ahead of the coupled trajectory by as much as 40 m after 9 years. Differences in the radial and out-of-plane directions were limited to oscillations whose amplitude grew up to 4 m.

  In terms of Keplerian elements, it was found that the quantity $\Omega + \omega$ decreased at a rate of about 0.75 arcsec/year in the uncoupled trajectory when compared to the coupled trajectory. Orbital inclination showed long-period oscillations each 2.3 years with growing amplitude that reached 0.06 arcsec after 9 years.
- **How well do analytical approaches to describe Phobos' orientation in an uncoupled model represent the features of the rotational motion obtained by numerically integrating a coupled model?**

  Uncoupled models featuring only a once-per-orbit longitudinal libration are not designed to produce latitudinal librations. Thus, any rotation in a coupled model that occurs about an axis other than Phobos' polar axis cannot be represented by uncoupled models. Furthermore, uncoupled models do not give rise to the phenomenon of resonance, by which small dynamical forcings are amplified when their frequency is close to one of Phobos' normal modes. This causes resonant forcings to be mis-represented by uncoupled models. The most significant of these resonances is a longitudinal libration with amplitude 2.5×10^{-4} degrees close to the longitudinal normal mode of the coupled model, which does not exist in the uncoupled model. The peak in longitudinal libration close to the latitudinal normal mode is amplified in the coupled model to twice its amplitude in the uncoupled model; the peak close to half the latitudinal normal mode is amplified in the coupled model to ten times its amplitude in the uncoupled model.
- **What are the differences between the parameters estimated by an uncoupled estimation model and the parameters used to generate the observations with a coupled model?**

  Three different parameter sets were estimated in this thesis:

  - Initial state
  - Initial state and once-per-orbit longitudinal libration amplitude
  - Initial state and gravity coefficients $\overline{C}_{2,0}$ and $\overline{C}_{2,2}$.

Errors in estimated initial position were in the order of several centimeters, while errors in initial velocity were in the order of μm/s. When estimated on its own, the along-track component of the estimated initial position showed the largest error, owing to the large along-track effects of couplings, while the out-of-plane components of both position and velocity showed the smallest errors, with relative errors in the order of 10^{-9} for both position and velocity. When additional parameters are estimated together with the initial state, however, errors in R and S components of both position and velocity decrease by 2 orders of magnitude, while errors in the W components stay the same, becoming the largest.

This decrease in initial position estimate is caused by absorption of couplings into the libration amplitude or the harmonic coefficients. For a 250-day arc, the estimate of the once-per-orbit physical longitudinal libration amplitude differed from the *true* amplitude by about 1.6×10^{-3}, while the estimates of $\overline{C}_{2,0}$ and $\overline{C}_{2,2}$ were off by 5.4×10^{-5} and 2.0×10^{-5} respectively.

To what extent can an uncoupled dynamical model of Phobos' translation and rotation emulate a coupled dynamical model?

This work has considered uncoupled models that feature the once-per-orbit longitudinal libration. The main differences introduced by couplings are longitudinal librations at other frequencies, as well as all latitudinal librations. Furthermore, coupled models introduce the resonant amplification of forcings close to Phobos' normal modes, which the uncoupled model cannot account for. This results in the underestimation of longitudinal librations close to the latitudinal normal mode, as well as the complete omission of librations close to the longitudinal normal mode. This mis-representation of Phobos' orientation causes Phobos' orbit to get ahead when computed with an uncoupled model as opposed to the coupled solution. The along-track offset between both solutions accumulated to 40 m after 9 years. The uncoupled solution also features oscillations in the radial and out-of-plane directions, whose amplitude grow up to 4 m after 9 years.

Differences between the coupled and uncoupled solutions were minimized by finding the dynamical parameters that produces a trajectory as computed with the uncoupled model that best fits the coupled solution through a least-squares parameter estimation. For this, the once-per-orbit libration amplitude and gravity field coefficients $\overline{C}_{2,0}$ and $\overline{C}_{2,2}$ were separately estimated, each of them together with the initial state. Both estimations provided extremely similar results. It was found that position differences in the along track direction could be reduced by an order of magnitude, while radial differences could be reduced to small oscillations at millimeter level. These parameters, however, were not effective in reducing the differences in the out-of-plane direction. Furthermore, long-period oscillations in the along-track component of residuals were seen to be relevant for long estimations. These reductions are driven by changes in estimated parameters with respect to their true values. For the libration amplitude, the change was of 1.6×10^{-3} degrees, while for the harmonic coefficients $\overline{C}_{2,0}$ and $\overline{C}_{2,2}$ the changes were of 5.4×10^{-5} and 2.0×10^{-5} respectively.

3.2. Recommendations

There are several steps that could be taken in order to improve on the product of this thesis that have been left for future research. They are collected here in order of complexity taking this thesis as starting point.

- It was observed that estimations of the libration amplitude and gravity coefficients produced residuals featuring long-period oscillations in their along-track components that had the potential to become dominant for longer estimations. Considering longer time scales in these estimations would therefore clarify how these residuals would evolve with time.
- This thesis has used ideal observations of Phobos' center of mass in all the estimations for practicality reasons and to facilitate the insight in the dynamical effects of couplings. Furthermore, these observations were all equally spaced from one another and spanned most of the estimated arc in a consistent manner. A perhaps more useful type of observations in the context of the use of these results for future missions would be to use range observations to a lander on Phobos' surface. These range measurements should account for visibility conditions, resulting in short arcs separated by hours or days, that are processed together.

- The dynamical model used in this thesis has been made as minimal as possible to help in isolating the effects of couplings while still retaining all relevant dynamics usually considered in the study of Phobos. However, a deeper study of the role of couplings in parameter estimation could benefit from the inclusion of additional perturbations, in particular in terms of Phobos' gravity field, where its irregular shape could render higher harmonics relevant in the study.
- As a continuation of the previous point, the big uncertainties associated to Phobos' higher harmonics usually makes their inclusion in state-of-the-art estimation schemes impractical, and a quadrupole gravity field of Phobos is still widely used. In this sense, the potential improvement that a coupled model could represent over an uncoupled model in estimation could be tested by using the same quadrupole-field dynamics to fit both models to observations generated by a coupled model with an extended gravitational field of Phobos.
- This thesis has shown that couplings will be necessary to process observations of a laser ranging system to a Phobos lander, while a Phobos-bound mission will likely also provide range measurements to a Phobos orbiter and the most advantage can be taken by processing all of them together. Thus, the science return of such a lander + orbiter mission can then be analyzed with the knowledge that this analysis should be done by using a coupled model to represent Phobos' dynamics.

Bibliography

Dobrovolskis, A.R., 1982. Internal stresses in phobos and other triaxial bodies. Icarus 52, 136–148. doi:10.1016/0019-1035(82)90174-9.

ESA, 2019. Martian moons: Phobos. URL: https://sci.esa.int/web/mars-express/-/31031-phobos.

Jacobson, R.A., 2010. The orbits and masses of the martian satellites and the libration of phobos. The Astronomical Journal 139, 668–679. doi:10.1088/0004-6256/139/2/668.

Kerr, F.J., Whipple, F.L., 1951. Possible explanations of the secular acceleration of phobos and jupiter v. The Astronomical Journal 56, 131. URL: https://ui.adsabs.harvard.edu/abs/1951AJ.....56R.131K, doi:10.1086/106617.

Lainey, V., Dehant, V., Pätzold, M., 2007. First numerical ephemerides of the martian moons. Astronomy & Astrophysics 465, 1075–1084. doi:10.1051/0004-6361:20065466.

Lainey, V., Pasewaldt, A., Robert, V., Rosenblatt, P., Jaumann, R., Oberst, J., Roatsch, T., Willner, K., Ziese, R., Thuillot, W., 2021. Mars moon ephemerides after 14 years of mars express data. Astronomy & Astrophysics 650, A64. doi:10.1051/0004-6361/202039406.

Maistre, S.L., Rivoldini, A., Rosenblatt, P., 2019. Signature of phobos' interior structure in its gravity field and libration. Icarus 321, 272–290. doi:10.1016/j.icarus.2018.11.022.

Murray, J.B., Iliffe, J.C., Muller, J.P.A.L., Neukum, G., Werner, S., Balme, M.R., 2006. New evidence on the origin of phobos' parallel grooves from hrsc mars express, in: Mackwell, S., Stansbery, E. (Eds.), 37th Annual Lunar and Planetary Science Conference, p. 2195. URL: https://ui.adsabs.harvard.edu/abs/2006LPI....37.2195M.

Oberst, J., Zubarev, A., Nadezhdina, I., Shishkina, L., Rambaux, N., 2014. The phobos geodetic control point network and rotation model. Planetary and Space Science 102, 45–50. doi:10.1016/j.pss.2014.03.006.

Rambaux, N., Castillo-Rogez, J.C., Maistre, S.L., Rosenblatt, P., 2012. Rotational motion of phobos. Astronomy & Astrophysics 548, A14. doi:10.1051/0004-6361/201219710.

Smith, B.A., 1970. Phobos: Preliminary results from mariner 7. Science 168, 828–830. doi:10.1126/science.168.3933.828.

Usui, T., ichi Bajo, K., Fujiya, W., Furukawa, Y., Koike, M., Miura, Y.N., Sugahara, H., Tachibana, S., Takano, Y., Kuramoto, K., 2020. The importance of phobos sample return for understanding the mars-moon system. Space Science Reviews 216. doi:10.1007/s11214-020-00668-9.

Veverka, J., 1978. The surfaces of phobos and deimos. Vistas in Astronomy 22, 163–192. doi:10.1016/0083-6656(78)90014-4.

Woolard, E.W., 1944. The secular perturbations of the satellites of mars. The Astronomical Journal 51, 33. URL: https://ui.adsabs.harvard.edu/abs/1944AJ.....51...33W, doi:10.1086/105793.

A

Integrator selection

Preliminary work made it clear that integrator constraints were tight in this problem. To set a numerical requirement on the admissible integrator error, the effect of the phenomenon of interest needs to be quantified. In this case, this phenomenon is the coupling between Phobos' translational and rotational equations of motion. The following was done to quantify them.

First, the damping algorithm described in the presented research paper was applied on the coupled model as explained in Appendix C of the research paper included in chapter 2. The result is a ~9 year long arc free of proper modes, which will act as a simulated ephemeris of Phobos. This ephemeris was used to obtain (a) the *real* libration amplitude of Phobos and (b) an initial translational state. These two elements were fed to the translational uncoupled model, making it as similar as possible to the coupled model. The uncoupled model was then propagated for the same ~9 year long arc, and the differences in *position* were computed between the two arcs. The norms of these position differences can be seen in Figure A.1. In the same figure, the same quantity is plotted for a period of 1 month - similar to the duration of the estimation arcs that we will work with.

All this was done with a preliminar choice of integrator of RKF10(12) with a fixed time-step of 5min.

Figure A.1 shows that errors of nearly 100m can accumulate only due to couplings over 10 years. However, by working with shorter estimation arcs - in the order of several weeks or a few months - it is more representative to consider the plot in Figure A.1b, where errors just reach the 1m line, with 10cm being a more conservative approximation of this error. A good choice of integrator will have integration errors fall between 2 and 3 orders of magnitude below these 10^{-1} m, so an integrator accuracy of $10^{-4} - 10^{-3}$ m will be sought.

Tudat provides three main types of integrators: Runge-Kutta (RK), Bulirsch-Stoer (BS) and Adams-Bashforth-Moulton (ABM). All these will be made to work in fixed-step regime, in order to have

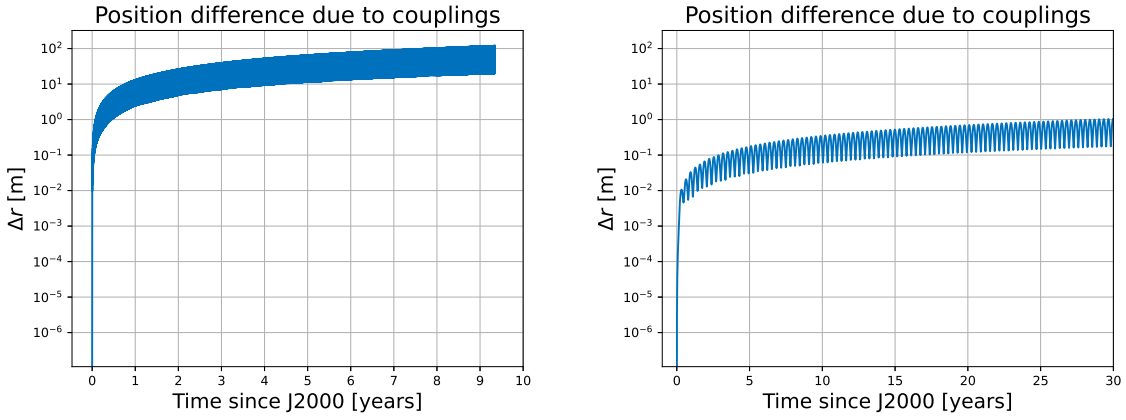

(a) Couplings effects over ~9 years

(b) Couplings effects over 1 month

Figure A.1: Coupling effects

consistency and uniformity in the solution output points. Of these, extrapolation integrators (i.e. BS integrators) are not as suitable for dense outputs, as required in the present thesis, since they perform several sub-integrations for each integration point. The consequences of this were observed in preliminary analysis, where integration times of BS integrations were far higher than those of RK integrators for the same accuracy performance. So much so, that some of the attempts with this type of integrator were interrupted and a comprehensive analysis was deemed too time-consuming. Therefore the focus was turned to RK and ABM integrators.

A study was done on all RK integrators and several orders of the ABM integrator using both the coupled and uncoupled models, and an optimal step size was sought that met accuracy requirements while not going into the region of dominance of rounding error. The range of time steps that were studied is bounded from above by output density, which is preferred to be high - some simulations are supposed to represent "continuous reality" - and from below by the storage capacity of the laptop used - the implementation of the forward/backward propagation of the damping algorithm generates a huge amount of data. The time steps that were considered go from 30 seconds to 10 minutes.

The comparison can be seen in Figure A.2. In particular, the ABM integrator with orders 2, 4 and 6 does not present any time step setting that falls within accuracy requirements. Furthermore, integrators RKF10(12) and RKF12(14) do not present the rounding-truncation transition in this range of time-steps, and only their rounding region is observed. All these integrators will not be considered for further analysis. Due to available diversity, the ABM integrator with order 8 will be discarded from further analysis, as it only provides one single point within accuracy requirements. The same plot for the remaining integrators is presented in Figure A.3. Here, it is possible to see that the ABM integrator with order 10, and both RKF9(8) and RKV9(8), fall into rounding dominance before or right when they begin complying with accuracy requirements. The same thing happens to RKF8(10). Thus, an RKDP integrator seems the most suitable for this problem. The transition from truncation to rounding dominance occurs around a time step of 4.5 minutes (270 seconds). This will be the choice of integrator for the rest of the work. The error of this integrator is plotted, for a month, in Figure A.4a. As a final sanity check, Figure A.4b shows that the integration error falls always between 2 and 3 orders of magnitude below the physical differences created by the couplings in Phobos' translational and rotational equations of motion.

Although seemingly complete, this analysis was a preliminar one in order to select a somewhat intermediate integrator. Once the choice of integrator was made, estimations were performed and a new approach was taken at quantifying the required numerical accuracy.

The definition of *the difference between coupled and uncoupled models* has some additional subtleties in this work. The thesis presents several estimations for which observations have been simulated using a coupled model, while the estimation model is an uncoupled one. The estimation will fit the uncoupled model to the coupled one by changing the initial position and possibly some parameters. In this case, the difference between the two models is not what is seen in Figure A.1, but rather the residuals of the estimation.

Preliminary estimations were performed using the selected integrator - the RKDP7(8) with a 4.5min time step - and the residuals were studied for different cases. Figure A.5a shows some statistics of the post-fit residuals of an estimation with only initial state fitting for different lengths of the estimated arc. On the other hand, Figure A.5b shows the same thing but for an estimation that fits both initial state and the harmonic coefficients $C_{2,0}$ and $C_{2,2}$ of Phobos. On the other hand, Figure A.5c shows the post-fit residual time history for an estimation fitting initial state and gravity field during 90 days. As can be seen, *the difference between a coupled and uncoupled model* is not in the order of 1×10^{-1} meters, but rather in the order of 1×10^{-2} meters.

If physical differences in the models are in these orders of magnitude, one would want numerical error to be below 1×10^{-4} meters, at least. This new requirement is quite stringent in the looks of Figure A.2 and Figure A.3, where the range $1 \times 10^{-4} - 1 \times 10^{-3}$ seems to be the door to rounding for all integrators. It looks like one is forced to work in a regime in which integration error and physical differences coexist at the same level. However, one can manage to make the two look very different if numerical errors are set to work in the rounding regime. Physical differences accumulate in a rather smooth manner, as can be appreciated in Figure A.5c or Figure A.1. On the other hand, rounding error is known to be erratic. The more erratic they are, the more different they will look from model differences. One can take advantage of this by choosing an integrator that works well within its rounding regime. At the same time, the smaller time steps will be avoided if possible so as to decrease computation time -

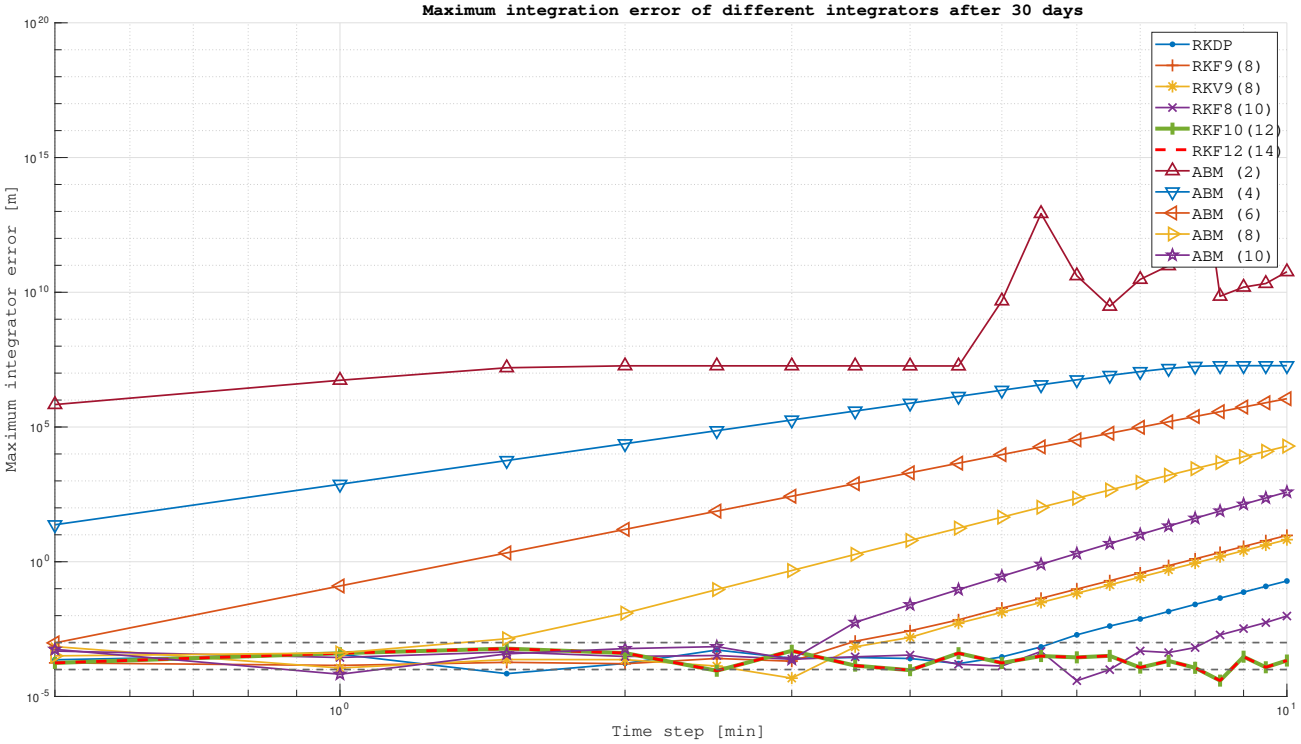

Figure A.2: Integrator errors as a function of time step for different integrators

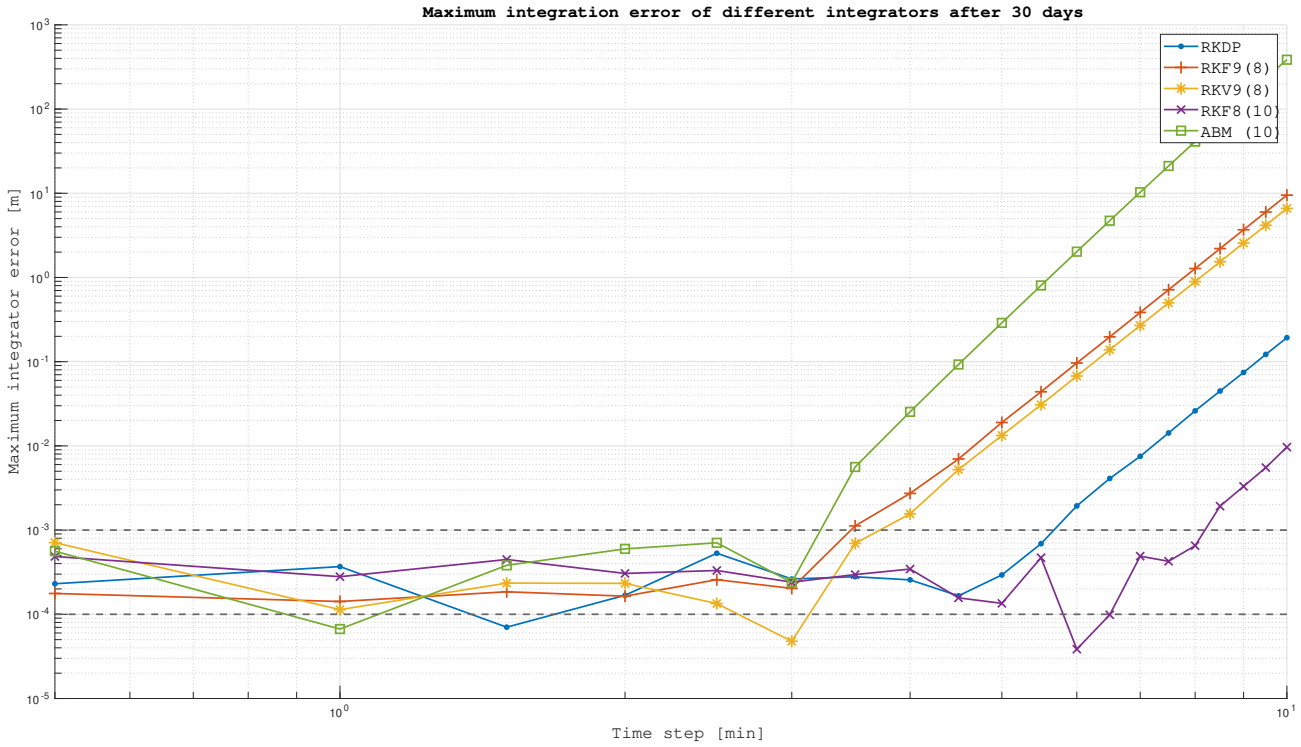

Figure A.3: Integrator errors as a function of time step for a selection of integrators

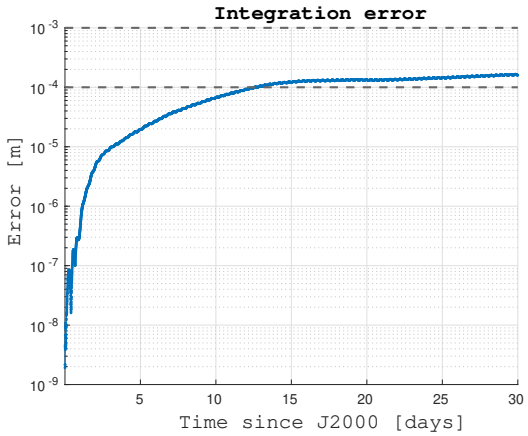

(a) Integration errors as a function of time for RKDP7(8) with a time step of 4.5 minutes.

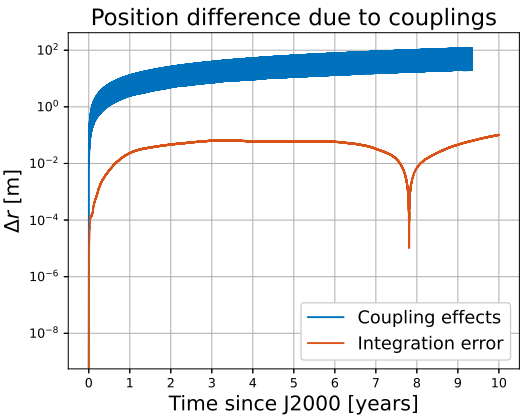

(b) Integration error of final choice of integrator compared to coupling-derived differences

Figure A.4: Coupling effects

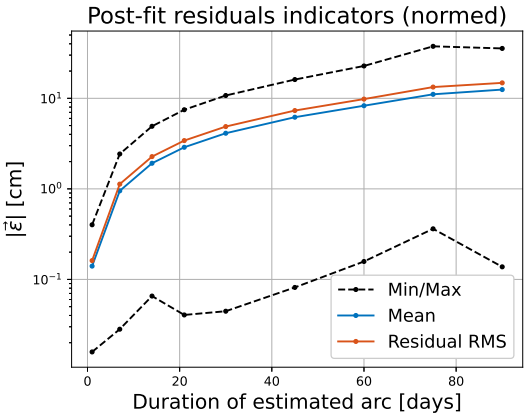

(a) Post-fit residual statistics for a fitting of initial state

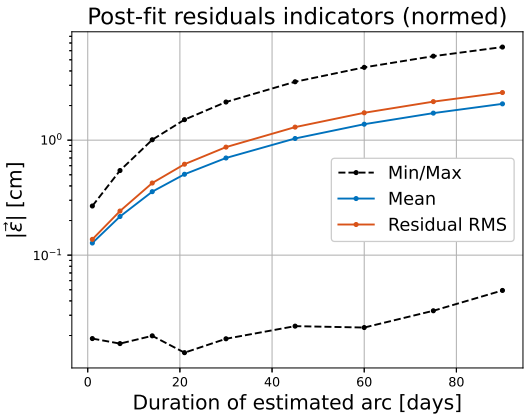

(b) Post-fit residual statistics for a fitting of initial state and harmonics coefficients $C_{2,0}$ and $C_{2,2}$

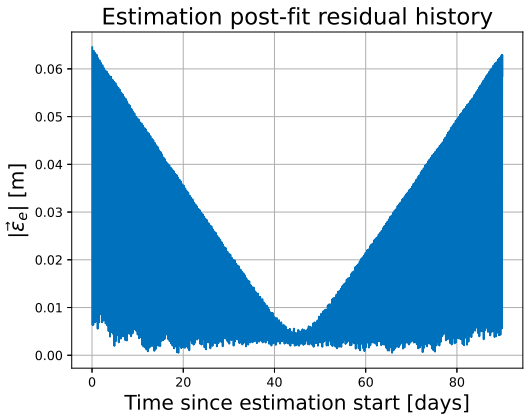

(c) Post-fit residual history for a 90-day-arc fitting of initial state and harmonics coefficients $C_{2,0}$ and $C_{2,2}$

Figure A.5: Residual statistics for two different estimations. An uncoupled model estimates a coupled model.

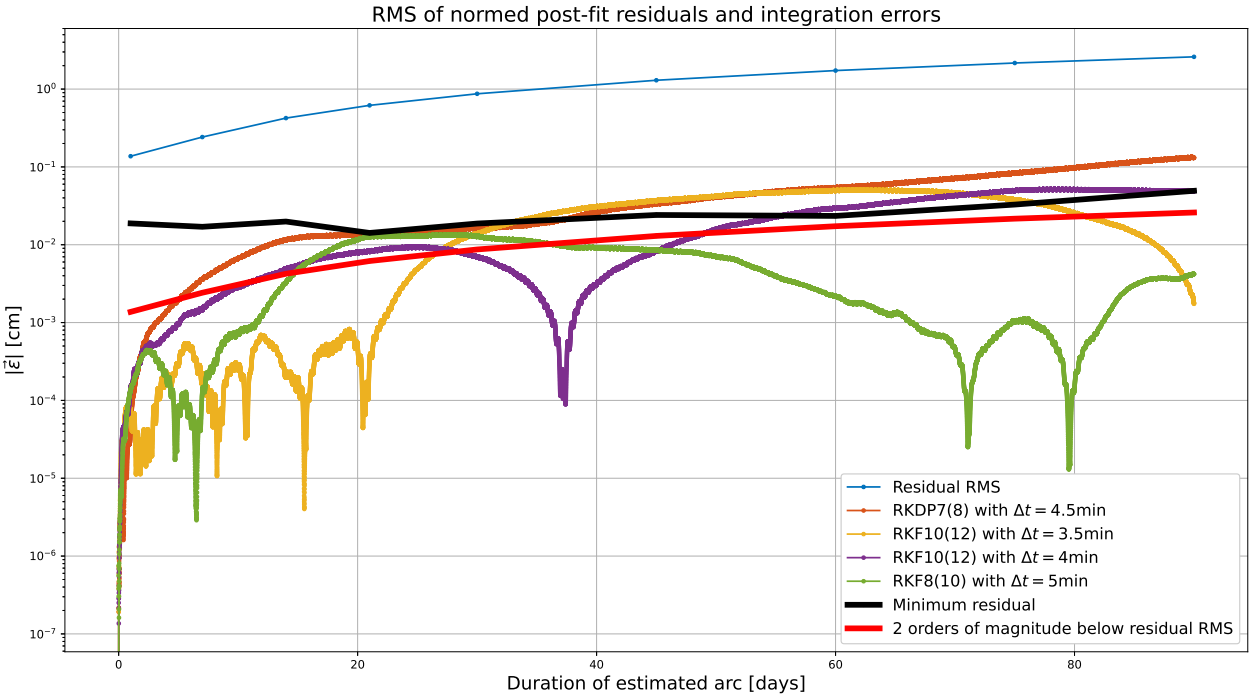

Figure A.6: Residual RMS for different estimation times and time evolution of the integration error for different integrator and integrator settings. Both initial state and Phobos' quadrupole gravity field were fitted

although not expected to be a bottleneck, lower run times are always preferred. They also do not present any advantage in terms of rounding error.

There are now two different scenarios, in which different requirements have to be imposed:

- Numerical errors are at least 2 orders of magnitude below residuals. Here, we accept an integrator working in truncation regime.
- If numerical error and physical differences coexist, the integrator should work in rounding regime.

Figure A.6 contains all the information required to make this choice. On the one hand, the residual RMS for different estimation times of an estimation that fits both initial state and libration amplitude. On the other hand, the numerical error of a selection of different integrators over time. It is intuitive to plot them together because an estimation of 20 days will encounter all the integration errors of those 20 days, but will be "immune" to those after that. Additionally, two thresholds are shown in the same plot: the 2-orders-of-magnitude-below-RMS and the minimum residual. The first one will be prioritized, as it gives a better indication of the order of magnitude of the residuals.

In the light of Figure A.6, there is really no case in which a clear rounding-driven behaviour - like the one seen for the RKF10(12) integrator with a 3.5 minute time step, or for the the RKF8(10) integrator - coexists with an integration error at the same order of magnitude as the residuals. Furthermore, truncation seems to dominate after 40 days for all integrators except for the RKF8(10). The RKF10(12) with a 3.5 minute time step also shows non-truncation errors towards the end of this 90 day range, although a significant truncation dominated exists above the indicated thresholds between days 30 and 70. The RKF8(10) also presents such a region, but it is much shorter, between days ~17 and ~40. Thus, the RKF8(10) integrator with a time step of 5 minutes will be used for this thesis.

B

Verification and validation

This section will explain how it has been made sure that the software developed for this thesis works as it should. All Tudat features - orbit propagation and estimation suites - are assumed to work properly, as they have been developed and tested by a professional community. Thus, the individual pieces of software - i.e. integrator, propagator, ... - will not be explicitly validated here, but how they have been put together for this thesis will. There are three important parts that play a role in this thesis: translational dynamics propagation (aka the *orbit* propagation), rotational dynamics propagation and the estimation or *orbit determination* algorithm. More precisely, we will look at the following:

- Orbit propagation, analyzed based on the obtained trajectory and Keplerian elements.
- Propagation of rotational dynamics, analyzed mainly through Phobos' Euler angles in time and frequency domain, as well as Mars' location in Phobos' sky.
- Orbit determination, which has been tested by making one dynamical model estimate itself.

This thesis will involve - or has involved - 3 different dynamical models:

- Fully-locked: This is an uncoupled translational model that propagates Phobos' translational state vector under the assumption that its x is always aligned with the moon-to-planet line.
- Uncoupled: Similar to the fully-locked model, this uncoupled model features a once-per-orbit longitudinal libration that deviates Phobos' x axis from the moon-to-planet direction by an amount $\psi = -\mathcal{B}e \sin M$.
- Coupled: This is a coupled translational-rotational model that simultaneously integrates Phobos' translational and rotational equations of motion.

In principle, there are two models (fully-locked and uncoupled) that need to be verified in two difference performance settings (verification of rotational dynamics does not apply to them), and one model that needs to be verified in all three. However, use will be made of past *Tudat* use and simulations that have been extensively done without any signs of problems will be assumed to have been verified, if anything by extensive past experience. These elements are:

- Orbit propagation using the fully-locked model.
- Orbit determination using the fully-locked model.
- Orbit propagation using the uncoupled model.

Furthermore, estimations will not be performed using the coupled model, so that is one less thing that needs verifying.

In this section, the orbit propagation using the coupled model will be verified in section B.1, the rotational dynamics using the coupled model will be verified in section B.2, and the orbit determination of the uncoupled model will be verified in section B.3.

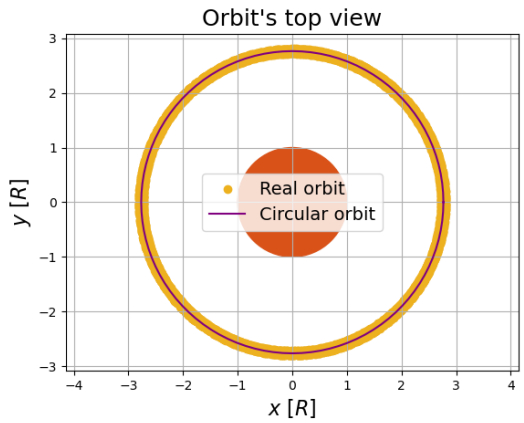

(a) Top view of the orbit. Distances expressed in Martian radii, $R = 3390$ km.

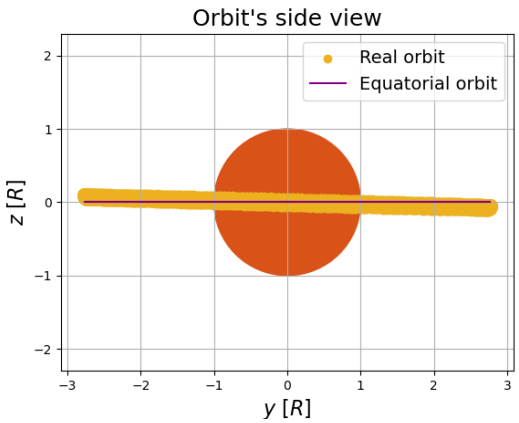

(b) Side view of the orbit. Distances expressed in Martian radii, $R = 3390$ km.

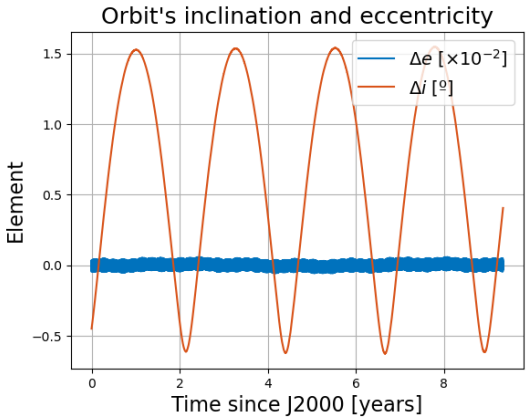

(c) Inclination and eccentricity. Differences with respect to nominal values of $i = 1.1^{\circ}$ and $e = 0.0151$. Note the scales and units.

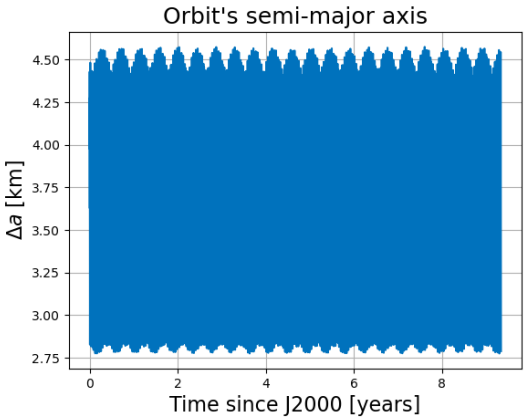

(d) Semi-major axis. Difference with respect to nominal value of $a = 9375$ km.

Figure B.1: Projection of Phobos' trajectory over 9 years and 4 months onto two of the three inertial planes (top) and time history of some selected orbital elements (bottom).

B.1. Orbit propagation

The propagation of the translational dynamics will be made on the basis of the orbit not *blowing up*. It is good practice to plot the overall orbit. This does not give a lot of quantitative information because scales are usually quite big, but it does validate the pre-assumptions that one approaches the problem with. In this case, these assumptions are that the orbit is (quasi-)equatorial and (quasi-)circular, and it should remain like that for the whole integration time (i.e. $e, i \approx 0$).

The top and side views of the orbit, can be seen in Figure B.1. At first sight, the orbit is indeed regular, with very low eccentricity - see Figure B.1a - and inclination - see Figure B.1b. One the other hand, more detailed information can be found in Figure B.1c and Figure B.1d, which show that the orbit's semi-major axis, eccentricity and inclination all oscillate close to and around their nominal values of $a = 9375$ km, $e = 0.0151$ and $i = 1.1^{\circ}$.

Offsets and oscillations will still exist, as the plots are obtained with a very specific dynamical model and report osculating values of the elements, while the tabulated information is an average taken from ESA (2019).

B.2. Rotational dynamics

The impact of Phobos' orientation on its orbit is not so big that one can look at plots of the Keplerian elements and see if something is going on with its orientation. Thus, a dedicated verification process of the propagation of Phobos' rotational dynamics is required. A typical description of the orientation of a body is the 3-1-3 Euler angles. With Phobos in fully-locked rotation, one would expect the first two

angles to be near 0 and the third angle to complete a full revolution per orbital period. This situation, however, leads to the Euler angles being ill-defined, since the axes around which the first and third rotations occur are identical. Furthermore, the Euler angles are defined with respect to three axes that are fixed in inertial space. With Phobos' orientation following its orbit over long timescales, the precession of the nodes will carry onto the Euler angle representation of Phobos' orientation.

For these reasons, it is practical - and sensible - to analyze Phobos' orientation by looking at Mars' Phobos-fixed spherical position, i.e. the location of Mars in Phobos' sky. If Phobos rotates in a fully-locked configuration - understood as Phobos' long axis pointing always directly towards Mars - then Mars should not move at all as seen from Phobos. However, because we are not imposing this kind of rotation but rather propagating the dynamics, Phobos will show librations in all three axes, which will make Mars oscillate around this otherwise fixed point. The rotation of Phobos is mostly driven by its own gravity field. This coupled model uses only the $C_{2,0}$ and $C_{2,2}$ coefficients to describe Phobos' gravity field, whose gravitational potential U behaves as shown in Equation B.1, where θ and ϕ are the Phobos-fixed longitude and latitude of Mars, respectively. With Phobos' gravity field being both latitudinally and longitudinally symmetric, oscillations of Mars in the Phobian sky should also be symmetric about $\theta, \phi = 0$.

$$U \propto C_{2,0} \cos(2\phi) - 4C_{2,2} \left(1 + \cos(2\phi)\right) \cos(2\theta) \tag{B.1}$$

The most prominent of these oscillations should occur in the East-West direction, lead by the once-per-orbit longitudinal libration of Phobos. Equation 9b in the research paper included in chapter 2 provides an expression for the scaled amplitude of the once-per-orbit longitudinal tidal libration. It has been collected in Equation B.2 for convenience. On the other hand, Equation B.3 gathers the numeric values of all the terms in the equation. Note the introduction of the eccentricity to obtain the un-scaled amplitude of the libration. For a correct verification and validation of the rotational dynamics, the Phobos-fixed coordinates of Mars should oscillate most prominently in the East-West direction with an amplitude of around 2.86°. In terms of the once-per-orbit physical longitudinal libration of Phobos, $\mathcal{A} = -1.125°$, which matches well with the known libration of ~1.1° (Rambaux et al., 2012; Lainey et al., 2021).

$$\begin{gathered} \mathcal{A} = \frac{2e}{1 - \frac{1}{3\sigma}} \qquad \mathcal{B} = \frac{2}{1 - 3\sigma} \qquad \sigma = \frac{I_{yy} - I_{xx}}{I_{zz}} \\ I_{xx} = \frac{1}{3}C_{2,0} - 2C_{2,2} + \tilde{I} \qquad I_{yy} = \frac{1}{3}C_{2,0} + 2C_{2,2} + \tilde{I} \qquad I_{zz} = -\frac{2}{3}C_{2,0} + \tilde{I} \end{gathered} \tag{B.2}$$

$$\begin{gathered} \tilde{I} = 0.2645232788265306 \qquad C_{2,0} = -0.01307786717320527 \qquad C_{2,2} = 0.02426656445399719 \\ I_{xx} = 0.22250469649285748 \qquad I_{yy} = 0.2629489705828529 \qquad I_{zz} = 0.3081161694038815 \\ \sigma = 0.13126306927755121 \qquad e = 0.015115059930190826 \qquad \mathcal{B}e = 2.857188134150437° \end{gathered} \tag{B.3}$$

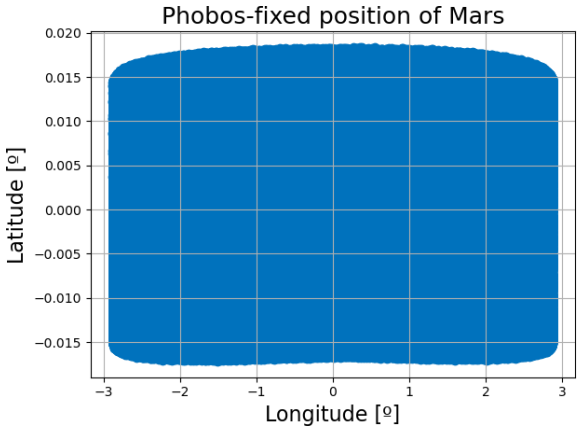

Figure B.2: Librations corresponding to the quadrupole field of Phobos.

In this thesis, the rotational dynamics come into play in the coupled model, where they are propagated together with the translational dynamics. Thus, all plots shown in this section should be assumed to have been generated by propagating the coupled dynamical model. In particular, Figure B.2 shows the position of Mars in the Phobian sky, which is the equivalent to Phobos' tidal librations, ψ (see section 2.2 of the research paper included in chapter 2). Indeed, Mars most prominently oscillates in the East-West direction with an amplitude of ~2.9°. Latitudinal oscillations extend to about ±0.15º, without showing any preferred directions. The small asymmetries between the upper and lower edges of the shape are attributed to the asphericity of Mars' gravity field, which as been expanded to degree and order 12 in this thesis.

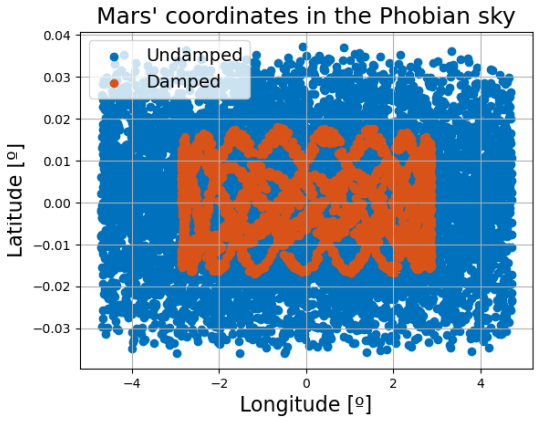

(a) Phobos-fixed position of Mars for the damped (orange) and undamped (blue) dynamics.

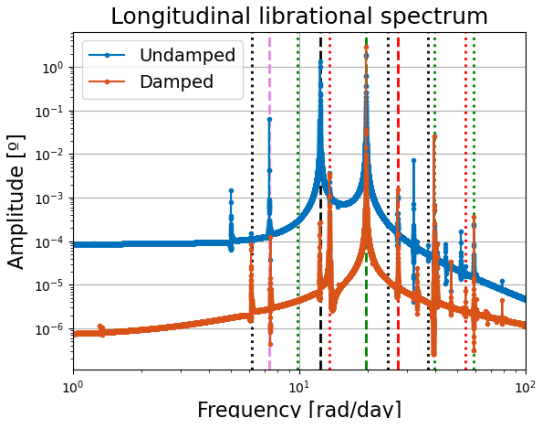

(b) Undamped librational spectrum

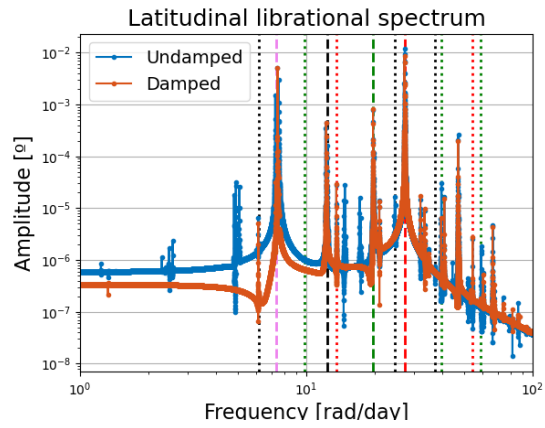

(c) Damped librational spectrum

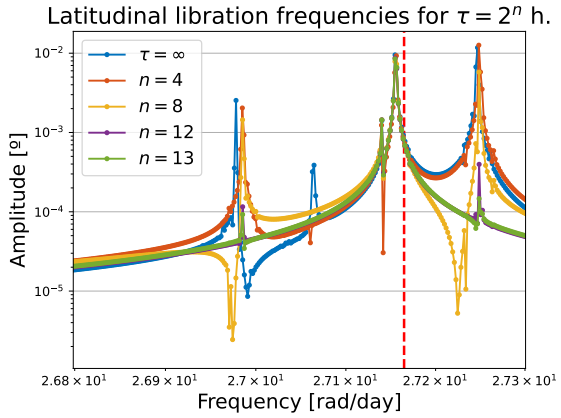

(d) Frequency content of latitudinal librations for backward propagations of iterations with different damping times τ. Forced librations are conserved, while normal modes are damped.

Figure B.3: Performance of the damping algorithm. Dashed vertical lines indicate the frequency of the orbital mean motion (green) and the three normal modes: longitudinal (black), latitudinal (red) and wobble (violet). Dotted lines are integer multiples/divisors of dashed lines.

Although Phobos rotates as was expected, there is one final aspect to verify: the damping algorithm. As explained in section 2.3 of the research paper included in chapter 2, directly propagating the rotational motion of Phobos will excite its normal modes, which are not seen in the present state of the moon. To get rid of them, the damping algorithm covered in appendix C of the same research paper is applied. In the proper functioning of this algorithm, the original dynamics contain all normal modes of the moon, while the final, damped dynamics do not. This change can be seen in two ways, and both are gathered in Figure B.3. On the top-left, Figure B.3a shows, as earlier, the Phobos-fixed spherical position of Mars. The undamped dynamics result in Phobos rotating significantly around its three axis, with greater longitudinal and latitudinal librations (blue in Figure B.3a) than the damped rotation (orange in Figure B.3a). On the top-right, Figure B.3b shows the frequency spectrum of Phobos' tidal longitudinal

librations for the undamped (blue) and damped (orange dynamics). Although all frequencies have been greatly reduced, the effect is most significant in the libration associated to the longitudinal normal mode (vertical black dashed line), whose amplitude is reduced in 4 orders of magnitude. Librations at other frequencies, like those at half the latitudinal normal mode, or those associated to the mean motion, are seen to remain after damping, being therefore librations produced by forcings and amplified by their proximity to the normal modes themselves. The same thing, but for latitudinal librations, can be seen in Figure B.3c. Although a lot of frequencies around the normal modes seem to remain, the zoom-in view in Figure B.3d shows how the peak around the latitudinal normal mode - which in the left picture looks like a single peak, is in fact 3 different peaks, two of which are associated to the excitation of the normal modes (on the sides) and one which is a forcing amplified by its proximity to the normal mode (in the middle). As a reminder, the frequencies of the normal modes have been computed as in Equation 12 of the paper included in chapter 2, which are linearized approximations, explaining why Figure B.3d shows peaks that seem to be displaced from the red line.

B.3. Orbit determination

The second main part of this thesis is the implementation of the estimation problem - in this astrodynamics context called also *orbit determination*. Although the individual parts that are required to solve the orbit determination problem - residual computation, variational equation integration, ... - are done by *Tudat*, the setup of the estimation problem is done by the user. It is this "putting all the pieces together" that needs verifying. As a reminder, only verification with the uncoupled model will be performed. For that, an estimation was performed such that this dynamical model had to estimate itself, i.e. the observations were generated using the exact same dynamics as those used for estimation. Then, the initial state was slightly perturbed and the estimation was left to minimize the residuals. Because the matching is perfect, post-fit residuals are expected to be nil - rather, at the level of numerical noise - and the parameters are expected to quickly converge to their real values.

The test estimation involved the uncoupled model estimating its own initial state for an arc of 30 days. After observations were simulated, the initial state was perturbed for estimation. The estimation algorithm was let to run for a fixed number of iterations: 10 in this case. The estimation post-fit residuals can be seen in Figure B.4a. To its right, in Figure B.4b, the evolution of the difference between the estimated and real initial state has been plotted (iteration 0 is the pre-fit value, i.e. the perturbation that was applied on the initial state). Post-fit residuals are at the level of numerical noise (10^{-5} m) and show signs of rounding error dominance, so they can be considered nil or "flat". On the other hand, the error in the estimated position is in the order of 10^{-6} m, and those in the estimated velocity are in the order of 10^{-9} m/s, i.e. completely negligible. Although post-fit residuals and estimated parameters do reach the expected level of agreement with the observations, convergence had been expected to be quicker and more straight-forward. However, it is observed that the estimator does not reach a stable value of the estimated parameters, but rather reaches the minimum residual - "converges" - at the very last iteration.

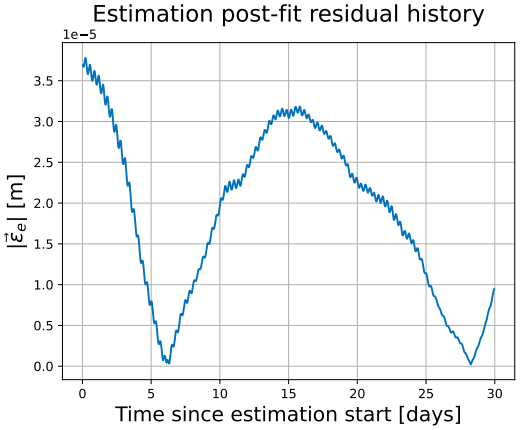

(a) Post-fit residual history.

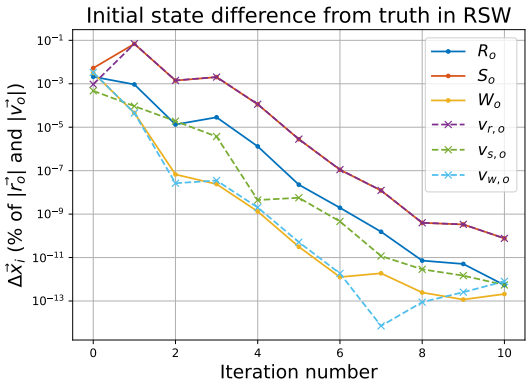

(b) Errors in estimated initial state. $|\vec{r}_o| = 9.48414595 \times 10^6$ m and $|\vec{v}_o| = 2.11298166 \times 10^3$ m/s

Figure B.4: Estimation results for an estimation of initial state. A librational model estimates itself.

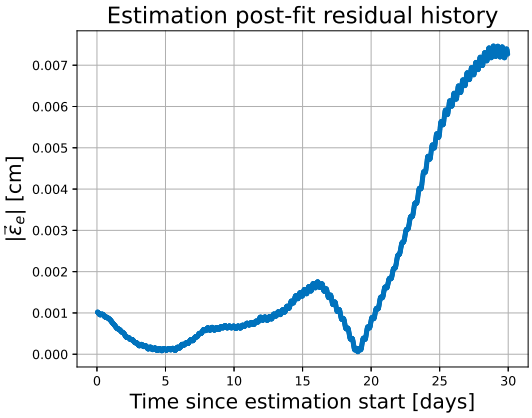

(a) Post-fit residual history.

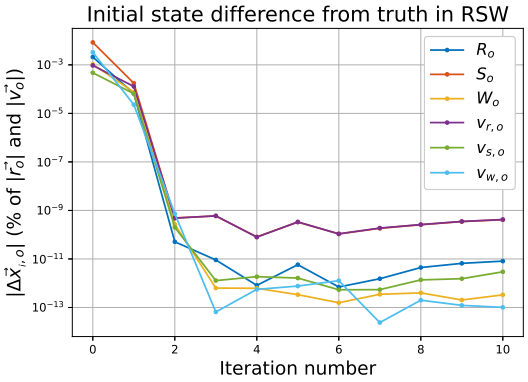

(b) Errors in estimated initial state. $|\vec{r}_o| = 9.48370373 \times 10^6$ m and $|\vec{v}_o| = 2.11308130 \times 10^3$ m/s

Figure B.5: Estimation results for an estimation of initial state. A synchronous model estimates itself.

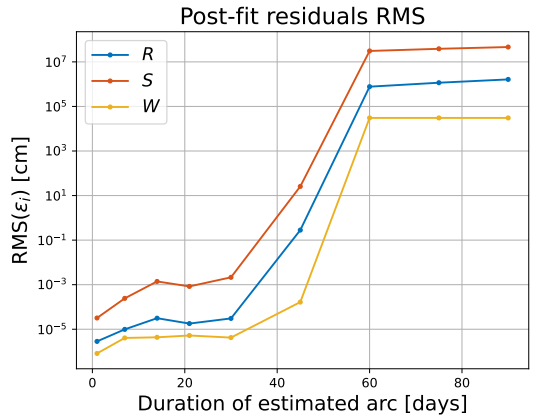

(a) Evolution of post-fit residual RMS. Shown here, the component of the residuals along each RSW direction.

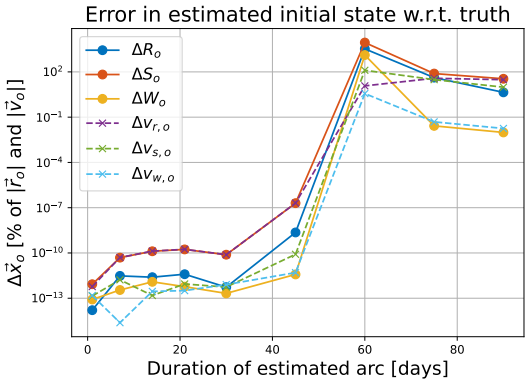

(b) Errors in estimated initial state. $|\vec{r}_o| = 9.48414595 \times 10^6$ m and $|\vec{v}_o| = 2.11298166 \times 10^3$ m/s

Figure B.6: Estimation results after 10 iterations for different estimation times. A synchronous model estimates itself.

To check whether this was common in other scenarios - and the expectation was somehow wrong - or this is an issue that should be further looked into, the same estimation test was performed using the fully-locked model. The same as shown in Figure B.4 is now shown in Figure B.5 for this new estimation. The post-fit residuals in Figure B.5a are very similar to those in Figure B.4a - at noise level and case-showing rounding dominance - while the convergence trend observed in Figure B.5b resembles what was expected of the test more than that in Figure B.4b: a rapidly decaying error and a fast convergence reached in only 3 iterations.

To further investigate this, several arcs of ever-increasing duration - 1, 7, 14, 21, 30, 45, 60, 75 and 90 days - were used to test the limits of this "weak" convergence. All estimations ran for 10 iterations. Figure B.6 shows the results, after 10 iterations, of the estimation test performed with the uncoupled model, but for different estimation times (note the units in Figure B.6a). For estimation times of up to a month, residual RMS stay below the millimeter level, and errors in position and velocity are 12 orders of magnitude below the actual values. For longer estimation times, things are quite different. Residual RMS increases to around the meter level for an estimation time of 45 days, and completely blows up beyond that. In particular, one sees that residuals increase by some tens of centimeters between a 30 and a 45 day arc, but they jump ~100 km between a 45 and a 60 day arc. A similar trend is observed in the error of the estimated initial state (Figure B.6b). There is a significant increase at the 45 day mark, and a completely disproportionate jump at the 60 day mark.

This phenomenon is not expected from an estimation in which observations and estimation are performed with the same dynamical model, because the residual function has one very clear absolute

minimum: the parameters with which observations were generated. The least squares algorithm was not performing as well as it should. Something was suspected to go wrong, and the first reason that was thought of was a mis-propagation of the variational equations. Thus, an in-depth investigation was carried out to assess whether this was indeed the case.

B.4. Libration partials

In verifying the orbit determination setup, it was suggested that *Tudat* might not correctly integrate the variational equations when the once-per-orbit libration is present in the dynamics. Further investigation was carried out on the partial derivatives of the state vector - or, rather, of the position vector, which is what in the end represents the observations used in this thesis. For this, *Tudat*'s analytical partial derivatives of the position with respect to all possible estimatable parameters - initial state, libration amplitude, and harmonic coefficients, which will be collectively called the "parameter vector, $\vec{y}$" - were compared to numerical partial derivatives. These numerical partial derivatives were computed through a central difference approximation as in Equation B.4, where y_i represents one component of the parameter vector and h is a small number. Note the Taylor expansion on the right hand side.

$$\frac{\partial \vec{x}}{\partial y_i} \approx \frac{\vec{x}(y_i + h) - \vec{x}(y_i - h)}{2h} = \frac{\partial \vec{x}}{\partial y_i} + \frac{1}{6}\frac{\partial^3 \vec{x}}{\partial {y_i}^3} h^2 + O\left(h^4\right) \tag{B.4}$$

The first step was to choose an appropriate value of h to compute the central difference. For this, the error $\vec{\varepsilon}$ of the central difference approximation will be computed by taking the difference $\Delta\vec{f}$ between two central differences computed with two different values of h, as in Equation B.5. By choosing $h_2 << h_1$, one gets a very good approximation of the error of the central difference computed with h_1. By definition, the error in the derivative by using h_2 will be even smaller. Note that an appropriate value of h might be different for the different parameters.

$$\Delta\vec{f} = \frac{1}{6}\frac{\partial^3 \vec{x}}{\partial {y_i}^3} h_1^2 \left(1 - \left(\frac{h_2}{h_1}\right)^2\right) \tag{B.5}$$

If a value of h_1 for each estimated parameter is found to be "precise enough", the central difference computed with h_2 will be by definition more precise. At the same time, this h_2 will perturb the trajectory in an even less significant manner, and it might be the case that the effect it has on the dynamics is so small that it is swamped by numerical error. It is important to check that this is not the case. This effect can be approximated by $\Delta\vec{r} = \vec{f} \times h_2$.

Choosing an appropriate h therefore involves comparing $|\Delta\vec{f}|$ with $|\vec{f}(h_1)|$ and making sure that the former is much smaller than the latter, while at the same time comparing $|\vec{f}(h_2)|$ with the numerical noise and making sure the latter is much smaller than the former. Here, "much smaller" means "at least 2 orders of magnitude below". The first of these two comparisons can be seen in Figure B.7 for the derivatives with respect to the initial state vector $\vec{x}_o$ (Figure B.7a) and for the derivatives with respect to the libration amplitude and the two harmonic coefficients (Figure B.7b). The second comparison can be seen in Figure B.8 for the derivatives with respect to the initial state vector (Figure B.8a) and the derivatives with respect to $\mathcal{B}$ and the harmonic coefficients (Figure B.8b). The values of h_1 and h_2 that were used for each parameter are collected in Table B.1.

Figure B.7a shows that the gap between $|\vec{f}|$ and $|\Delta\vec{f}|$ is of ~ 4 orders of magnitude for the derivatives of the position with respect to the initial velocity, and of ~ 6 orders of magnitude for the derivatives with respect to the initial position. In Figure B.7b, errors in $|\vec{f}|$ are seen to be ~ 5 orders of magnitude below $|\vec{f}|$ itself for the derivatives with respect to the harmonic coefficients, and between 2 and 3 for the

Parameter	x_o	y_o	z_o	$v_{x,o}$	$v_{y,o}$	$v_{z,o}$	$\mathcal{B}$	$C_{2,0}$	$C_{2,2}$
h_1	10.0	10.0	10.0	10^{-5}	10^{-5}	10^{-5}	0.01	0.001	0.001
h_2	1.0	1.0	1.0	10^{-6}	10^{-6}	10^{-6}	0.001	0.0001	0.0001

Table B.1: Values of h_1 and h_2 that were used in Equation B.5 to compute the error in the central difference with respect to each parameter. Note that $h_2/h_1 = 0.1$ for all cases.

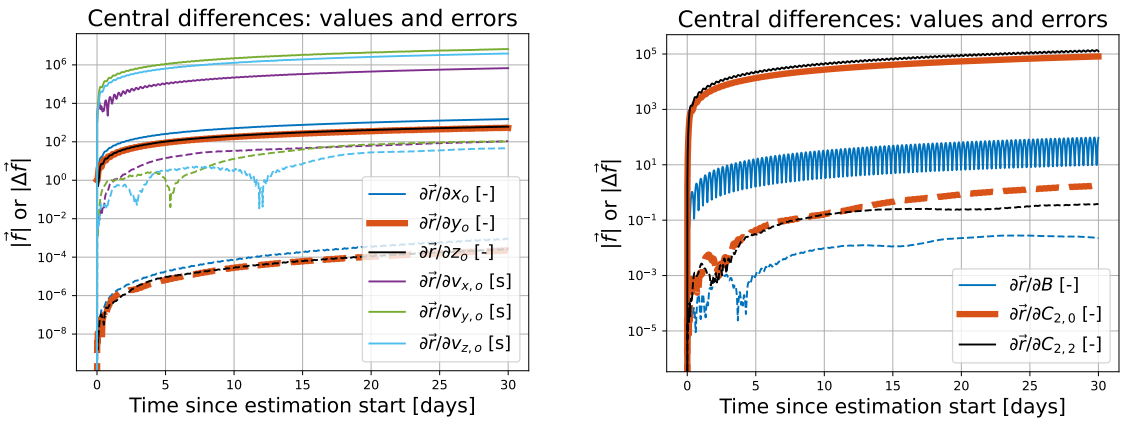

(a) Central differences with respect to $\vec{x}_o$

(b) Central differences with respect to $\mathcal{B}$, $C_{2,0}$ and $C_{2,2}$

Figure B.7: Central differences (solid) computed with h_1 from Table B.1 and their errors (dashed) computed as in Equation B.5.

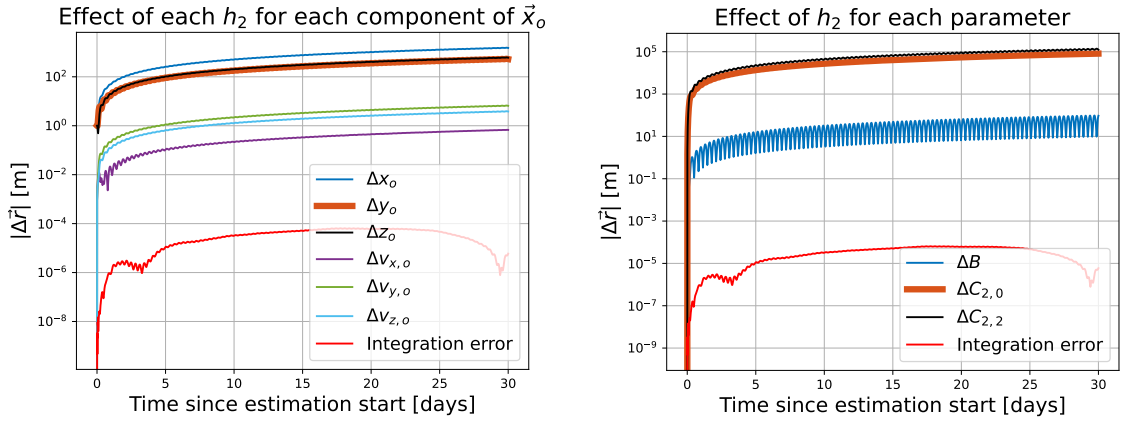

(a) Effect of h_2 in $\vec{x}_o$

(b) Effect of h_2 in $\mathcal{B}$, $C_{2,0}$ and $C_{2,2}$

Figure B.8: Effect on trajectory caused by variations of size h_2 from Table B.1 in parameters compared to the integration error.

derivatives with respect to $\mathcal{B}$. Note that some of the errors even show signs of rounding error in them. All these values of h_1 - and therefore of h_2 - comply with the precision requirement. On the other hand all lines in Figure B.8 can be seen to be no less than 4 orders of magnitude above numerical noise level, and therefore all values of h_2 comply as well with this requirement.

Now that it is sure that central differences are indeed a good representation of the partial derivatives, we can proceed in comparing these "numerical derivatives" with the "analytical derivatives" computed by *Tudat* by integrating the variational equations. The numerical differences, collected in a "numerical design matrix $\tilde{\boldsymbol{H}}$" can be directly subtracted from the analytical derivatives, collected in an "analytical design matrix $\boldsymbol{H}$", to compute the errors in $\boldsymbol{H}$. In doing the analysis, it was found that working in RSW components was more insightful than working in Cartesian components. Thus, plots will be shown containing derivatives of the RSW components of the position vector with respect to RSW components of the initial state vector and the parameters. These are computed on the basis on Equation B.6a together with relationships in Equation B.6b. In these expressions, $\Delta\vec{r}$ and $\Delta\vec{v}$ indicate changes in position and velocity expressed in XYZ components, $\Delta\vec{\rho}$ and $\Delta\vec{\eta}$ indicate a change in position and velocity expressed in RSW components and $\boldsymbol{R}$ is the inertial-to-RSW rotation matrix such that $\Delta\vec{\rho} = \boldsymbol{R}\Delta\vec{r}$. Furthermore, α represents any estimatable parameter that is *not* part of the initial state vector, i.e. $\mathcal{B}$, $C_{2,0}$ or $C_{2,2}$.

$$\begin{aligned} \Delta\vec{r} = \boldsymbol{\Phi}_{rr}\Delta\vec{r}_o + \boldsymbol{\Phi}_{rv}\Delta\vec{v}_o \quad &\Longrightarrow \quad \Delta\vec{\rho} = \boldsymbol{\Phi}_{\rho\rho}\Delta\vec{\rho}_o + \boldsymbol{\Phi}_{\rho\eta}\Delta\vec{\eta}_o \\ \Delta\vec{r} = \boldsymbol{S}\Delta\alpha \quad &\Longrightarrow \quad \Delta\vec{\rho} = \boldsymbol{\Lambda}\Delta\alpha \end{aligned} \tag{B.6a}$$

$$\begin{bmatrix}\boldsymbol{\Phi}_{rr} & \boldsymbol{\Phi}_{rv}\end{bmatrix} = \begin{bmatrix}\dfrac{\partial \vec{r}}{\partial \vec{r}_o} & \dfrac{\partial \vec{r}}{\partial \vec{v}_o}\end{bmatrix} \implies \begin{bmatrix}\boldsymbol{\Phi}_{\rho\rho} & \boldsymbol{\Phi}_{\rho\eta}\end{bmatrix} = \begin{bmatrix}\boldsymbol{R}\boldsymbol{\Phi}_{rr}\boldsymbol{R}_o^T & \boldsymbol{R}\boldsymbol{\Phi}_{rv}\boldsymbol{R}_o^T\end{bmatrix}$$
$$\boldsymbol{S} = \frac{\partial \vec{r}}{\partial \alpha} \implies \boldsymbol{\Lambda} = \boldsymbol{R}\boldsymbol{S} \tag{B.6b}$$

The derivatives of the position with respect to the initial velocity involve a total of 18 scalar quantities. For the sake of clarity, the values of $\tilde{\boldsymbol{H}}$ and $\boldsymbol{H}$ themselves will not be reported, but rather the errors among them $\Delta\boldsymbol{H} = \tilde{\boldsymbol{H}} - \boldsymbol{H}$ will be given. Although this might limit the interpretation of the data in terms of absolute numbers, a wrong integration of the variational equations is expected to manifest in an ever-diverging trend in the errors. Although this divergence might be slow in some derivatives of some components of the position vector - and therefore not appreciable in the 30 days of the estimated arc - the presence of the quickly diverging error of the derivative of one single component of the position vector with respect to some generic parameter α is indication enough that the derivatives wrt said parameter are not correctly computed. In fact, because a diverging signal in the derivative of one position component carries on to the norm of the derivatives of all three components, the analysis can be made on the basis of this latter quantity, reducing the relevant data by two thirds.

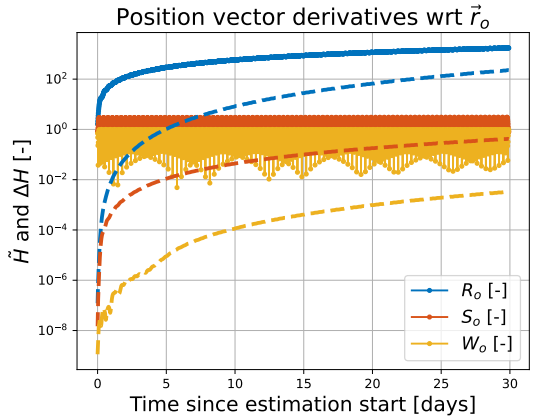

(a) Partials of ρ with respect to ρ_o (solid) and *Tudat*'s errors (dashed).

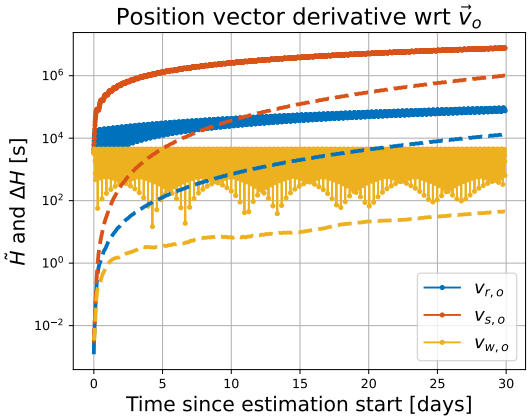

(b) Partials of ρ with respect to η_o (solid) and *Tudat*'s errors (dashed).

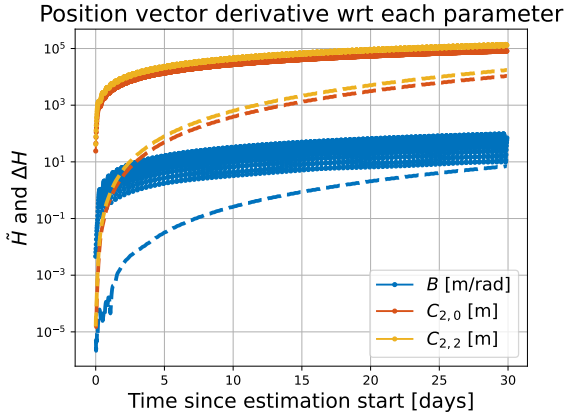

(c) Partials of ρ with respect to dynamical parameters $\mathcal{B}$, $C_{2,0}$ and $C_{2,2}$ (solid) and *Tudat*'s errors (dashed).

Figure B.9: Numerical derivatives and *Tudat*'s errors.

In an ideal situation, these errors $\Delta\boldsymbol{H}$ should always remain very small compared to the values of either $\tilde{\boldsymbol{H}}$ or $\boldsymbol{H}$ themselves, as the two correctly computed quantities are always approximately the same. Errors in the order of 5% are usually considered worrying already, so the difference between the two derivatives should always remain at least 2 orders of magnitude below the derivatives themselves. However, when some of the two quantities are wrongly computed, the error is expected to grow beyond the 10% of $\tilde{\boldsymbol{H}}$. This, however, requires specifying in how much time this should happen, as this might

not be the case for this 30-day test and still occur in 90-day estimations, for example. Thus, a better way to assess whether the error *is too big* is to look at its trend. If $\Delta\boldsymbol{H}$ grows faster than $\tilde{\boldsymbol{H}}$, the analytical partial derivatives are considered to be wrong.

The values of the numerical position derivatives $\tilde{\boldsymbol{H}}$ (solid) together with *Tudat*'s derivative errors $\Delta\boldsymbol{H}$ (dashed) can be seen plotted in Figure B.9. Each color in Figure B.9a represents the norm of one column of $\boldsymbol{\Phi}_{\rho\rho}$, each color in Figure B.9b represents the norm of one column of $\boldsymbol{\Phi}_{\rho\eta}$ and each color in Figure B.9c represents the norm of a column of $\boldsymbol{\Lambda}$. As was expected, the order of magnitude of the error can be seen to increase much faster than the order of magnitude of the derivatives themselves in all nine cases - in the extreme, the two become comparable for derivatives with respect to $\mathcal{B}$ in Figure B.9c.

In the light of this analysis, it was concluded that the variational equations are not integrated correctly by *Tudat*. Although the ideal solution would be to fix *Tudat*, it is not feasible at all due to time - and capability - constraints. Thus, the problem was circumvented by using the numerical derivatives that had already been implemented. Two tests were performed to truly assess that the numerical derivatives were indeed working correctly.

B.4.1. Test 1: Linearized residual increment

If we call $\vec{z}$ the vector of observations and $\vec{h}$ the vector of model values - i.e. the model's attempt at recreating the observations - the vector of residuals is given by $\vec{\varepsilon} = \vec{z} - \vec{h}$. The model is parameterized with vector $\vec{y}$, so that we can write Equation B.7 about $\vec{\varepsilon}$, and define an increment in residuals as in the same equation. Here, $\boldsymbol{H}$ is the design matrix, which is a concatenation of all matrices $\begin{bmatrix}\boldsymbol{\Phi}_{rr} & \boldsymbol{\Phi}_{rv}\end{bmatrix}$ at each observation epoch one below the other. This is, it collects all relevant partial derivatives.

$$\vec{\varepsilon}\left(\vec{y}\right) = \vec{z} - \vec{h}\left(\vec{y}\right) \quad \Longrightarrow \quad \Delta\vec{\varepsilon} = \vec{\varepsilon}\left(\vec{y} + \Delta\vec{y}\right) - \vec{\varepsilon}\left(\vec{y}\right) \approx \frac{\partial\vec{\varepsilon}}{\partial\vec{y}}\Delta\vec{y} = -\frac{\partial\vec{h}}{\partial\vec{y}}\Delta\vec{y} = -\boldsymbol{H}\Delta\vec{y} \tag{B.7}$$

In testing whether Equation B.7 holds, an arc of 30 days was considered, starting 1 year after J2000, and the initial state was taken as estimated parameter. The arc was propagated with some default initial state. Then, the partial derivatives $\boldsymbol{H}$ were numerically computed and a parameter $\Delta\vec{x}_o$ was computed by solving the normal equations $\boldsymbol{H}^T\boldsymbol{H}\Delta\vec{x}_o = \boldsymbol{H}^T\vec{\varepsilon}\left(\vec{x}_o\right)$. Now, one can compute the numerical residual $\Delta\vec{\varepsilon}_n = \vec{\varepsilon}\left(\vec{x}_o + \Delta\vec{x}_o\right) - \vec{\varepsilon}\left(\vec{x}_o\right)$ and the linearized post-fit residuals $\Delta\vec{\varepsilon}_l = -\boldsymbol{H}\Delta\vec{x}_o$. In the ideal case, the numerical and linearized residuals are the same - within 1%. Both $\left|\Delta\vec{\varepsilon}_n\right|$ and $\left|\Delta\vec{\varepsilon}_l\right|$, together with $\left|\Delta\vec{\varepsilon}_n - \Delta\vec{\varepsilon}_l\right|$ can be seen plotted in Figure B.10. The gap between the residual difference and the residuals themselves is roughly 2 orders of magnitude. It is, however, close enough to the limit that doubts about the performance of this algorithm could still persist. Nevertheless, this is just one small doubt in one iteration of a much bigger scheme. That is why a second test encompassing a full estimation was performed.

The result of this test is in the limit of "satisfactory". Given that this is just one iteration of a much bigger estimation process. The next test involves performing such an estimation, and will therefore be

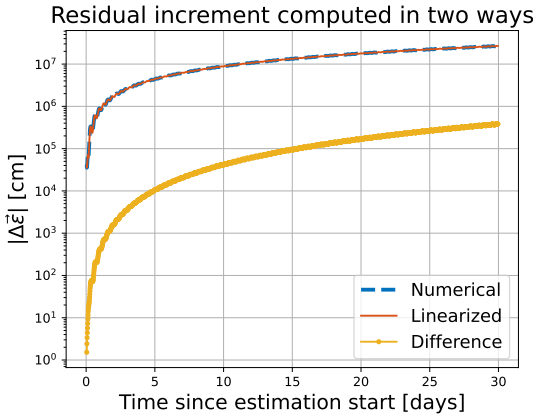

Figure B.10: Residual increment computed in two ways for a 30-day arc.

used as final word in tipping the balance for or against the use of numerical partials in estimation.

B.4.2. Test 2: Performance of full estimation

The final test was performing a full estimation, for which the same estimation settings were used as the ones described in section B.3. The aim is to recreate Figure B.6, with the expectation that post-fit residual RMS and estimated parameter error do not show such variability when changing the estimation time. The results are show in Figure B.11, which is completely analogous to Figure B.6, but for an estimation in which the partial derivatives have been computed numerically. As expected, residual RMS stays below the millimeter for all arc lengths - noise level - and errors in the estimated initial state remains ~ 11 orders of magnitude below the initial state itself.

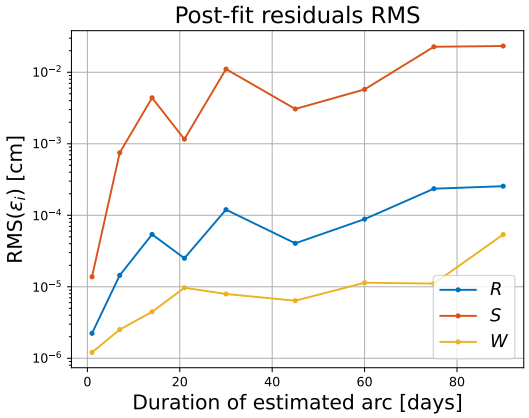

(a) Evolution of post-fit residual RMS. Shown here, the component of the residuals along each RSW direction.

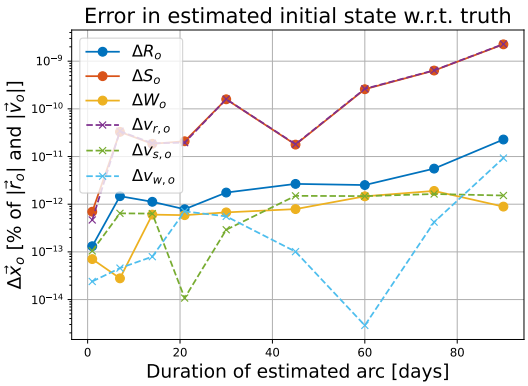

(b) Errors in estimated initial state. $|\vec{r}_o| = 9.48414595 \times 10^6$ m and $|\vec{v}_o| = 2.11298166 \times 10^3$ m/s

Figure B.11: Estimation results after 10 iterations for different estimation times. A synchronous model estimates itself. Partial derivatives of the position vector were obtained numerically.

For the sake of brevity and cleanliness, similar results for simulations in which the libration amplitude and/or Phobos' gravity field are estimated will not be shown. However, the same tests were done and the same conclusion was reached. Thus, the whole numerical estimation algorithm was tested and verified.

As a final conclusion, and in the light of the variational equations not providing the expected results for times longer than a month, it will be stated that all estimations performed in this thesis will be done using *Tudat* if the estimation time is lower than or equal to 30 days, while the numerical partials will be used for longer arcs. Unless otherwise stated, it should be assumed so.